Investigating Mechanotransduction by Two-Photon Fluorescence Microscopy Measurement of Intracellular Free Energy of Binding

by

Nur Aida Abdul Rahim
M.Eng. Mechanical Engineering (2003)
University of Cambridge, England

Submitted to the Department of Mechanical Engineering in Partial Fulfillment of the Requirements for the Degree of
Doctor of Philosophy in Mechanical Engineering
at the
Massachusetts Institute of Technology
May 2008
[June 2008]

Signature of Author

Department of Mechanical Engineering
April 20, 2008

Certified by

Roger D. Kamm
Germeshausen Professor of Mechanical and Biological Engineering
Thesis Supervisor

Certified by

Mohammad R. Kaazempur-Mofrad
Assistant Professor, Department of Bioengineering, University of California, Berkeley
Thesis Co-supervisor

Accepted by

Lallit Anand
Chairman, Department Committee on Graduate Students

Investigating Mechanotransduction by Two Photon Fluorescence Microscopy Measurement of Intracellular Free Energy of Binding

by

Nur Aida Abdul Rahim

Submitted to the Department of Mechanical Engineering
on May 1, 2008 in partial fulfillment of the requirements for the
Degree of Doctor of Philosophy in Mechanical Engineering

Abstract

Force, due either to haemodynamic shear stress or relayed directly to the cell through adhesion complexes, is transmitted and translated into biological signals. This process is known as mechanotransduction. Extensive studies have been carried out on the signaling pathways involved in mechanotransduction. However, the mechanism(s) of mechanotransduction has yet to be fully understood. This thesis focuses on the measurement of the intracellular binding constant between focal adhesion proteins of interest, GFP-Paxillin and FAT-mCherry, using two-photon excitation fluorescence microscopy and the utility of it as a measure of protein conformational change. The hypothesis tested is that force-induced changes in protein conformation alter inter-protein binding affinity.

A comprehensive toolkit that utilizes fluorescence microscopy techniques, Förster Resonance Energy Transfer (FRET) and its corollary, Fluorescence Lifetime Imaging (FLIM), as well as Fluorescence Correlation Spectroscopy (FCS), was developed. A procedure by which low photon counts cell data from FLIM could be included in global analysis fits and be corrected for was developed. This results in the recovery of maximum information from cellular data. Successful intracellular FCS measurements were combined with FLIM global analysis data to calculate the free energy of binding between GFP-Paxillin and FAT-mCherry. Results demonstrate that inter-cell heterogeneity exists and likely gives rise to differences in measured ΔG.

The application of these measurement techniques to cells experiencing 10% step strain shows that inter-protein binding is tighter upon stretch application. The source of this change is not clear, though Tyr phosphorylation has been ruled out by biochemical disruption of kinase activity.

Thesis supervisor: Roger D. Kamm
Title: Germeshausen Professor of Mechanical and Biological Engineering

Thesis co-supervisor: Mohammad R. Kaazempur-Mofrad
Title: Assistant Professor, Department of Bioengineering, University of California, Berkeley

Acknowledgements

Sincere thanks goes to my advisor, Roger Kamm, for his support and guidance. Everyone could learn a thing or two about the art of diplomacy from him. Thank you also to Mohammad R. K. Mofrad who brought me into the lab, giving me the leg up I needed in order to get initial exposure and direct involvement in the world of bioengineering. A big and cheerful thank you goes to Peter So for his amazing enthusiasm. Our meetings are always extremely charged with energy, I leave his office convinced that the next breakthrough is just round the corner. It is always a great moral booster. Thanks also to Rich Lee for his support and guidance throughout the course of this project. I have learnt a lot about how I want to do research, about how to ask good questions, from having had the wonderful opportunity of working with such a great group of people.

I am extremely fortunate to have joined a lab where the atmosphere is one of collegiality and cooperation. Better colleagues and friends could not be found elsewhere. Thank you very much to all members of the Kamm Lab, past and present. Thank you for the training sessions, the many discussions, the good advice, the new ideas, the inspiring role models, the late nights, the shared candy and chocolate, the borrowed cars, the gym trips, the sympathetic ear… Being part of the lab made things so much more bearable when the going got tough.

Thanks also to the members of my adopted lab on the 2nd floor, the So Lab, who helped me with my multiple and never-ending optics and microscopy-related questions. There are some very clever people down there.

Many thanks also go to the RTLee Lab for the help given with molecular biology.

Working with this fantastamazing set of people has been tremendously enjoyable.

Special thanks go to the many wonderful friends both here in the US and back in Malaysia, who have been there whenever I needed them, and who have helped me grow as a person throughout my stay here at MIT.

To my siblings, Adzim, Imaan, and Sahar, I wish them many thanks for being so nice to me even though I bullied them all the time. But that's what a big sister is for right? ☺

I am forever indebted to my parents for the love, understanding, patience, encouragement, support, advice, and help they have showered me from the moment I arrived into the world. I hope to be able to fulfill all the hopes and ambition they have for me, as a testament to the wonderful job they did raising me.

And lastly of course, I have my cute little chubby, naughty, cheeky, squeezable Princess Nasreen, a constant source of amusement for me, a great motivation to finish up, if ever I needed one.

Table of Contents

Chapter 1 Introduction

1.1 Mechanotransduction

The term mechanotransduction refers to the transmission and translation of mechanical forces into biochemical signals [5, 69]. The effects of mechanical force application are relevant to myriad biological processes, from single proteins to tissue level effects, concurrent with the multiple size scales inherent in biological systems. For example, at the protein-DNA interface, RNA polymerase needs to apply force in order to unwind the tight double-helical dsDNA and carry out transcription. By using an optical trap system to measure the amount of force required to stall the polymerase, Yin et. al. deduced that a force of $\approx$ 10 pN was being exerted [168]. At the cellular level, blood flow through blood vessels gives rise to hemodynamic stresses that influence endothelial biology [36], where changes stresses play an important role in the localization of atherosclerotic lesions [32, 56, 133]. On a larger scale, the everyday act of walking loads cartilage in articular joints, the force being transmitted throughout the tissue as hydrostatic pressure due to the high water content (75-80 wt%) [71]. Due to the important and pervasive effects of force on the complex biological system we call the human body, it is of great interest to many researchers to understand in greater detail the mechanism(s) of mechanotransduction.

1.1.1 Cellular response to mechanical cues

Blood flow-induced shear stress has been shown to be an essential feature of atherogenesis [32]. Atheroprotective laminar shear stress regulates normal vascular functions. A disturbance in the laminar flow profile promotes atherosclerosis, the buildup of plaque. Though the exact mechanisms of atherogenesis remain uncertain, the 'response-to-injury' theory [124] is widely accepted. Elevated levels of cholesterol and triglyceride in the blood, high blood pressure, tobacco smoke, and diabetes, all cause damage to the arterial wall. Fats, cholesterol, calcium, cellular waste products, platelets, and other substances are deposited in the damaged arterial wall. This deposition stimulates the endothelium to produce other substances that result in further thickening of the vessel wall, shrinking the artery's diameter, reducing blood flow and decreasing oxygen supply (refer Figure 1). In time, a blood clot could form near this plaque blocking the artery and stopping blood flow. In the heart, this leads to a heart attack. In the brain, this could result in a stroke. This cascading effect is fascinating, and devastating.

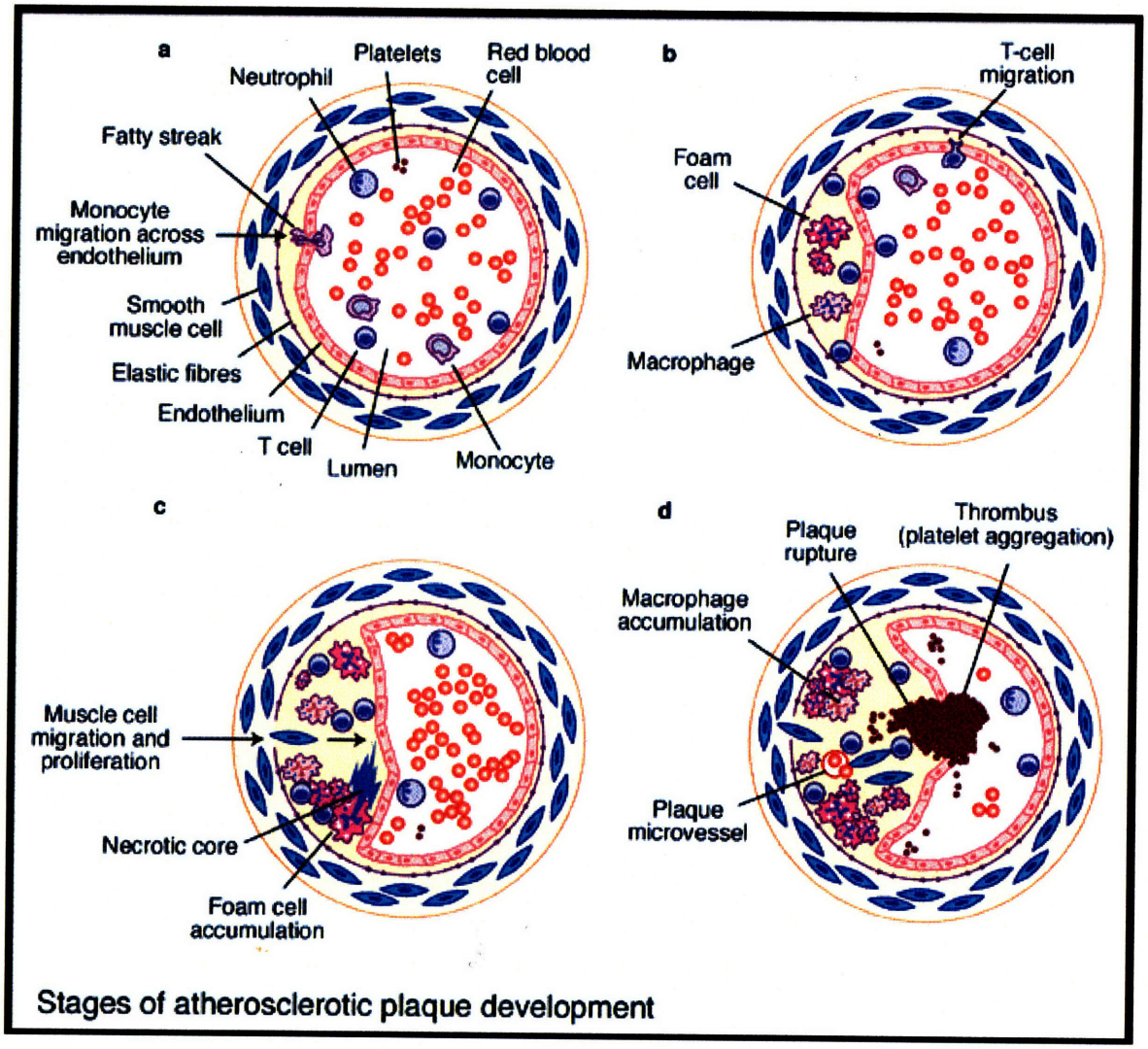

Figure 1 Stages of atherosclerotic plaque development. (a) The fatty streak is the earliest identifiable morphological change. This may be pre-dated by endothelial dysfunction, which can be detected using methods assessing vascular function (rather than morphology), and may persist or deteriorate as the atherosclerotic process advances. (b) The fatty streak is followed by the formation of an established plaque (often termed an intermediate lesion), characterized by the accumulation of increasing numbers of macrophage foam cells and a local chronic inflammatory infiltrate. (c) The complicated plaque is characterized by smooth muscle cell migration and the formation of a fibrous cap, the formation of a necrotic lipid core and an ever-increasing inflammatory infiltrate. (d) Plaque rupture may occur after the fibrous cap has been weakened by the production of degradative enzymes and reactive oxygen species by the inflammatory cellular infiltrate. This exposes highly prothrombotic material, which leads to the formation of thrombus that may result in the clinically recognized acute coronary syndromes. Figure and subtitle reproduced from Expert Reviews in Molecular Medicine © Cambridge University Press [137]

It is obvious that the endothelial cells lining blood vessels are greatly affected by, and contribute to, this cascading phenomenon. Thrombosis [7, 15], proliferation [88], wall inflammation [165], gene expression [25, 34], cell alignment and cytoskeletal arrangement [37], and nitric oxide production [106] have all been shown to be either affected or regulated by shear stress. The fact that such a myriad processes are influenced by, or influence, shear stress makes it all the more important to study the regulatory molecular mechanisms involved. Though some inroads are being made into this

complex web, more research needs to be done to completely untangle it. Our work thus focuses on improving our understanding of mechanotransduction as it relates to the cardiovascular system. It is noted that though medical diagnostic technologies and pharmaceutical approaches keep advancing at a rapid rate, cardiovascular disease continues to be the leading cause of death in the United States and Europe [17, 18].

1.1.2 Mechanotransduction mechanisms

Many groups have investigated and extensively characterized the signaling cascades that result from mechanical stress [75]. However, a strong understanding of the initiating process(es) is still lacking. The current view in the field is that mechanisms by which endothelial cells sense and transduce hydrodynamic forces are likely varied, and there is probably interplay between them, in order to affect global changes.

Fluid shear stress has been shown to increase membrane fluidity of endothelial cells [62], and there seems to be a differential increase between upstream and downstream elements where upstream diffusivity reaches a peak at 7 mins before decreasing despite continued shear stress application [21, 62]. This result relates to G protein activity, which was stimulated by artificially increasing membrane fluidity [49]. G protein activation in turn has been shown to occur within 1 s of flow onset. Thus the cell membrane itself might be a transducer of force.

The glycocalyx, glycosaminoglycan chains present on the apical cell surface, provides a barrier to shear stress, resulting in an essentially zero force being exerted on the apical plasma membrane [140]. The presence of an intact glycocalyx layer is necessary for the shear stress-induced suppression of motility and proliferation, and the glycocalyx itself is modulated by shear stress [166]. It has thus been proposed that the force transmitted through the glycocalyx to its membrane anchors is responsible for mediating mechanotransduction [159].

Ion channels are also implicated in mechanotransduction. The inward-rectifying K^+ current is activated upon shear stress [107], along with an increase in Ca^{2+} influx in endothelial cells [164]. This influx could in turn regulate the activation of other K^+- and Ca^{2+}-activated channels [105], providing the initial trigger for a signaling cascade. Ca^{2+} influx could also lead to production of bioactive agents such as NO.

Since forces that travel through the cell have to be transmitted through the load-bearing elements within the cell, the cytoskeleton itself has been proposed to play a role. Filamentous actin has been shown to realign in the direction of flow with the application of shear stress [34], thus the ability of the cytoskeleton to focus forces from flow to sites of both cell-cell and cell-matrix attachments is important.

The mechanism we are interested in focusing on here is related to the force transmission pathway that originates at the luminal / apical endothelial surface and terminates at focal adhesions (FA) at the basal surface, having crossed the cell membrane and traveled along the cytoskeleton (Figure 2). Visualized in cells plated on 2D surfaces, FAs can be clearly seen as punctate regions at the basal cell surface or a variety of sizes and morphologies, from very small spots called focal complexes to larger, more elongated spots (Figure 3). Actin stress fibers are seen to terminate at FAs. In some early studies, Davies et. al observed remodeling of FAs in the direction of flow within minutes of the

onset of flow [33]. Integrins, transmembrane glycoproteins that bind to a variety of extracellular and cytoplasmic proteins, are activated upon shear stress application, as manifested by modulations of affinity and avidity [133]. Integrins are implicated as intermediates that are activated downstream of PECAM-1, which along with VE-cadherin and VEGFR2 stimulates PI3-kinase [147].

Looking at it in another way and relating directly force and FA, FAs as sites of attachment between the cell and the extracellular matrix (ECM) allow direct communication between cytoskeletal elements and extracellular elements. It was once thought that FAs were relatively inert [52] but this myth has long been dispelled. Initial integrin attachment sites containing cytoskeletal proteins talin and actin mature into focal complexes (FCs) with the recruitment of vinculin. These small FCs (area $<1\mu m^2$) further develop into FAs which are larger and longer [122]. This development has been shown to both depend on, and be affected by, internally generated and externally applied force. Internally generated mechanical force is required to strengthen FCs to mature FAs, as removal of the actin-myosin contractile machinery was shown to suppress this process [50]. Early FC formation can be disrupted by 5pN external force directly applied to FCs, as shown by experiments using an optically-trapped bead [26]. These experiments further show that a sustained application of force on FCs leads to the development of stronger attachments. These strong attachments can then sustain forces of up to ten times the sustained force initially applied. Indirect external force application also causes nucleation of FCs, where force applied on the apical cell surface initiates FCs on the basal surface at both pN levels [50] and nN levels [122].

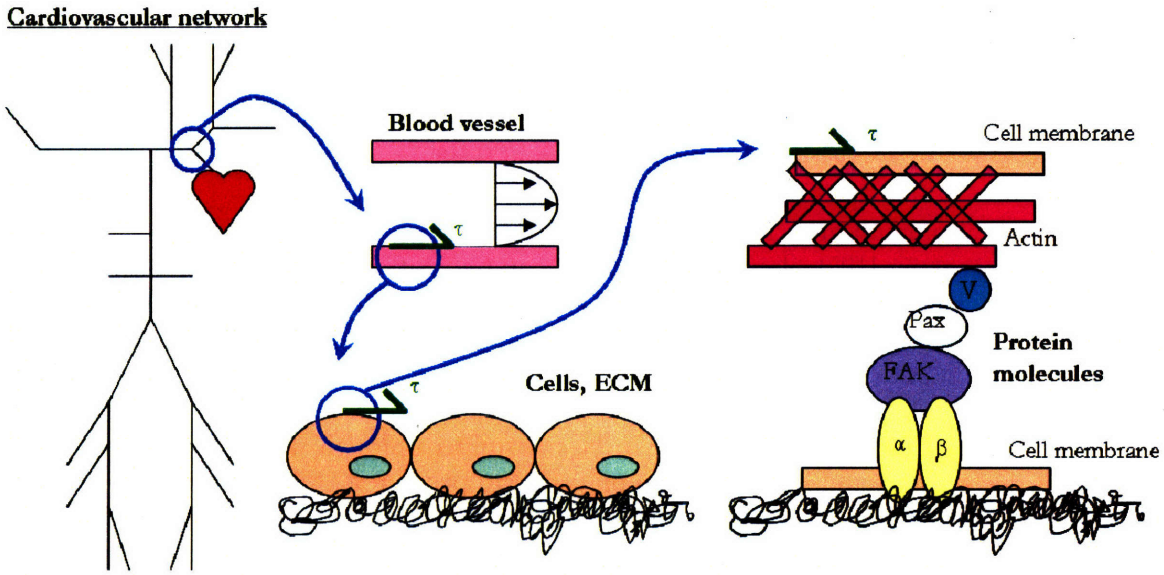

Figure 2 Cartoon of the cardiovascular network and pathway of force transmission arising from shear stress.

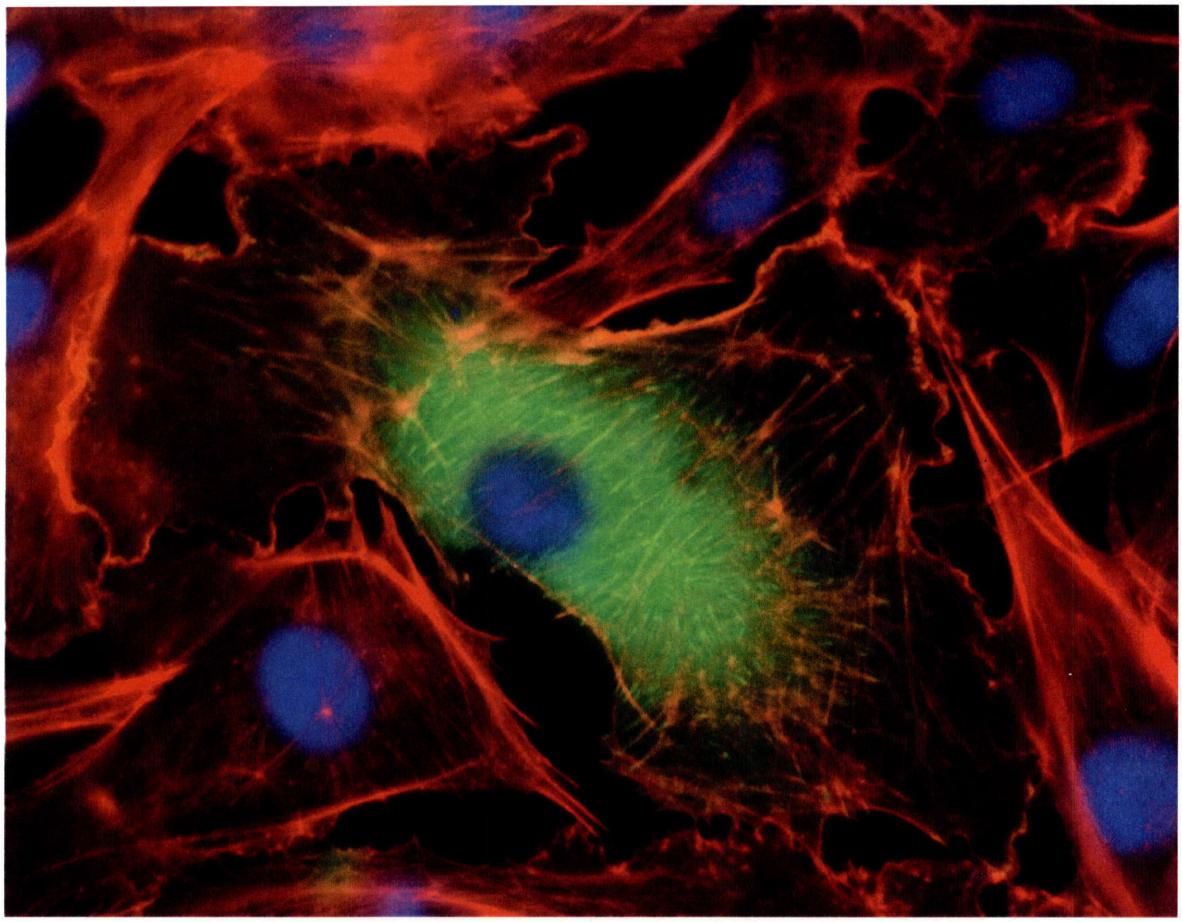

Figure 3 Epifluorescence image of GFP-Paxillin transfected cells. Cells were fixed with 4% paraformaldehyde and stained with DAPI (nucleus) and rhodamine-phalloidin (actin).

It is known that once formed, FAs are not merely stationary but are dynamic and mobile, assembling, disassembling and sliding [38, 82]. This dynamism and mobility can also be influenced by applied force. Non-directional FA translocation can be induced by both steady and oscillatory force applied on the apical surface via a magnetically trapped bead [92].

In summary, it is thus clear that force is an essential stimulus in regulating the behavior of FAs. The exact mechanism of this stimulus however is not understood.

1.1.3 Proteins within force transmission pathway

Investigations of this decentralized mechanotransduction model [34] have yielded extensive knowledge of the different protein components that reside along this pathway, culminating in schematic maps of estimated structural pathways and focal adhesion (FA) protein components [122]. Such a map is given in Figure 4. With more than fifty different proteins associated with FAs [170], some more significant than others, though all having a specific role to play this high degree of complexity necessitates a reduction of the system to a few important proteins. We identify the interaction between proteins paxillin and focal adhesion kinase (FAK) as a promising system. They are known to directly bind [31, 51, 65] and have been shown to be important to the wellbeing of the

cell. Paxillin-null fibroblasts exhibit defects including abnormal focal adhesions, reduced cell migration, inefficient localization of focal adhesion kinase (FAK) – though FAK has been shown to localize to FAs without paxillin [31] - and reduced fibronectin-induced phosphorylation of FAK, Cas, and mitogen-activated protein kinase (MAP kinase) [61]. FAK knockout mice suffer from defects in their developmental morphogenesis [72]. In cancer cells, FAK levels are found to be elevated [22]. Integrin-mediated binding results in autophosphorylation of FAK [144], and FAK signaling is essential to cell motility [101]. The complexity of FAK is further exemplified by its interaction with multiple other proteins including epidermal growth factor (EGF), platelet-driven growth factor (PDGF), p130Cas and Src.

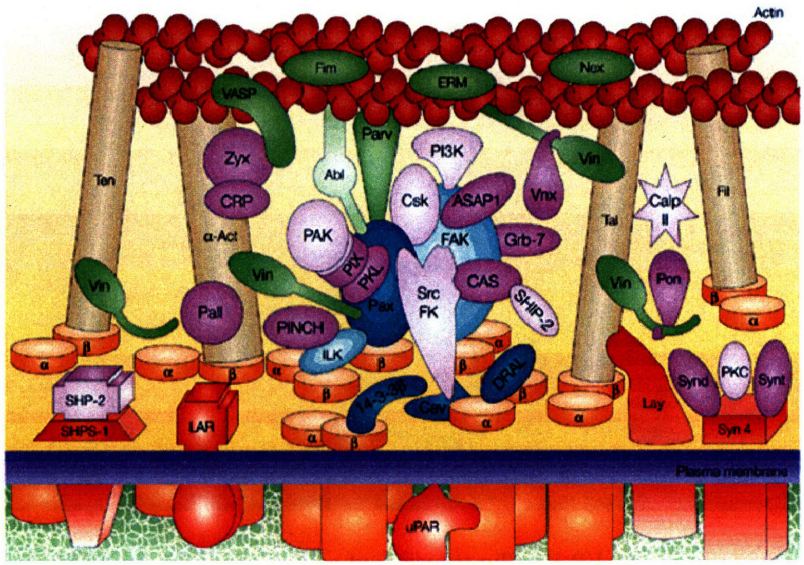

Figure 4 Schematic depicting the complexity of the main molecular domains of cell-matrix adhesions. Figure and subtitle reproduced from Geiger et. al. [53]

Force and FA composition

The application of force modifies FA composition and recruits proteins to FAs. Stretching of triton insoluble cytoskeleton matrices was shown to recruit many proteins to FAs, including paxillin, FAK and p130Cas [125]. Since Triton treatment disassembled the cell membrane, it is inconsequential here and this is evidence that stress applied directly to the extracellular matrix-integrin-cytoskeleton chain somehow modifies the binding affinity of certain cytoplasmic proteins to FAs.

Force and FA enzymatic activity

Of the many FA proteins, some are structural, functioning as connectors between different proteins, while others are biological, acting as signaling molecules or regulators of other proteins. Vinculin, one of the early recruits to FAs [171], is an example of the first kind of protein. It strengthens the attachment of integrins to the cytoskeleton and distributes internally and externally applied force. Proteins such as paxillin and FAK, each with multiple binding partners and with prominent enzymatic roles, likely play the dual role of strengthener and regulator, with phosphorylation being the signaling mechanism of choice. The link between force and phosphorylation has previously been made. When tyrosine kinase is inhibited, the patterns and trends of FA translocation initially observed are now different [92]. Conversely, application of force also affects phosphorylation, where shear stress has been shown to increase tyrosine phosphorylation and kinase activity of focal

adhesion kinase (FAK) [89], where phosphorylation on Y576 is two-fold higher after 20mins [131]. There is even a difference in phosphorylation site depending on the type of force applied, where shear stress induces phosphorylation at Y576 of FAK whereas cyclic strain induces phosphorylation at Y397 and Y576 [131]. For paxillin, phosphatase activity is indicated within the first minute of flow application, followed by several-fold increase in phosphorylation within 2hrs [35] thus showing a dephosphorylation / phosphorylation cycle.

Taken together, these suggest that a possible mechanotransduction mechanism is the force-induced conformational change of proteins that reside along the force transmission pathway, and which ultimately results in changes in binding affinity and / or enzyme activity [125]. The schematic in Figure 5, presented by Janmey et. al., shows how this kind of signaling might occur where external force applied to the extracellular protein causes proteins within the cell to deform and transduce signals that initiate a biochemical signaling cascade [74].

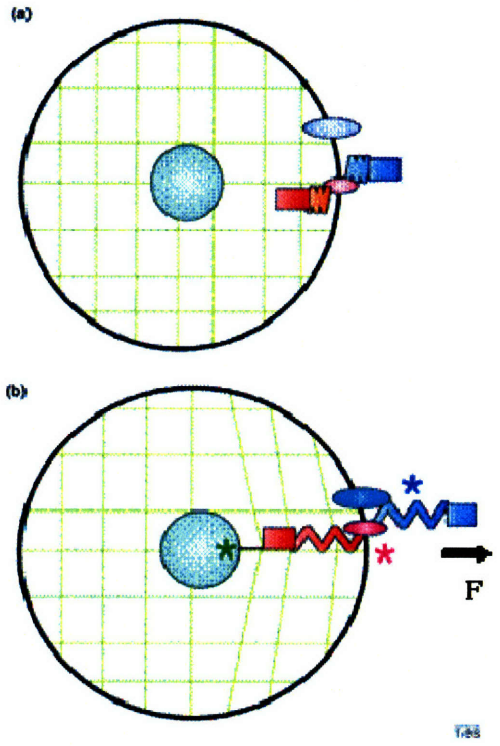

Figure 5 Mechanotransduction at the membrane-cytoskeletal interface. Figure reproduced from Janmey et. al. [74]

1.1.4 Protein conformational change

A protein's linear amino acid sequence leads to a specialized globular fold that at this point in time still cannot be reliably predicted, though great inroads have been achieved [39]. It is this tertiary structure that confers proteins its functionality. Changes in a protein's conformation could lead to changes in their chemical potential [54, 125], or expose cryptic binding sites [8], which will lead to changes in its 3D surface contour, thus affecting its interaction with binding partners.

The idea of protein conformational change upon force activation is not novel. It has been shown that fibrillogenesis of fibronectin is regulated by the exposure of cryptic binding sites, buried in the native fold of the protein [156]. Mechanosensitive channels of large conductance, MscL, are transducers of mechanical strain that arise in their membrane environment, thereby allowing the cell to regulate its behavior in response to changing environmental conditions. Mechanical strain toggles the channels between open and closed states. With the publication of the MscL crystal structure [23], many groups have attempted to discover the mechanism and pathway of its conformational change. For another FA protein, talin, a conformational change is required to expose a cryptic Vinculin binding site that would otherwise be hidden in its inactive state. It has been postulated that this leads to recruitment of vinculin to focal adhesions [70, 85].

1.2 Molecular dynamics (MD)

1.2.1 Protein crystal structure

With the application of x-ray crystallography and nuclear magnetic resonance (NMR) to the study of protein structure, the atom-by-atom placement of amino acids that make up these proteins is available. Such detailed molecular-level information of protein structures opens up the field of study that relates structure to function, as it enables examination and visualization of the various factors that affect protein configurations and that direct protein-protein interaction. Some of these factors include steric effects, hydrophobic regions, salt bridges, hydrogen bonds and ionic interactions. The availability of crystal structures also allows perturbation of the structure in order to examine the effects such perturbations have on the protein itself, and also effects on its interaction with other proteins and molecules.

1.2.2 Basis of molecular dynamics

The computer simulation technique that is used to calculate the time-dependent behavior of molecular-level systems is called molecular dynamics (MD). MD simulation consists of the numerical, step-by-step solution of the classical equations of motion. For a simple atomic system this may be written as $m_i \ddot{r}_i = f_i$. Forces, f_i, acting on the atoms, are derived from potential energies U, where $f_i = -\frac{\partial}{\partial r_i} U$. Potential energies arise from bonded and non-bonded interactions. Bonded interactions sum over atom pairs, bond angles, planar angles, and torsion angles, while non-bonded interactions account for electrostatic and van der Waals interaction.

1.2.3 Using MD to study protein-protein interactions

The use of MD to study the force-response of proteins was initially inspired by Atomic Force Microscopy (AFM) experiments, and termed steered molecular dynamics (SMD) [73, 136]. For example, Marszalek and co-authors [97] used SMD to illustrate the origin of a pre-extension 'hump' in sequential AFM unfolding of beta-sheet structure of both I28 and I27 titin multimers. The hypothesis was then verified by carrying out AFM experiments on an I27 mutant engineered based on the SMD results, and indeed the 'hump' was not seen [97]. AFM experiments on spectrin, alpha-helix bundle repeats, suggested that the repeats mechanically unfold one by one, predominantly

independently, in an all-or-none manner [121]. SMD simulations of two or more spectrin repeats identified the linker region between spectrin repeats as key elastic elements [108, 110]. Moving away from AFM experiments, MD studies recently carried out study the effects of a more realistic force application profile and location in an attempt to elucidate the mechanics of intracellular protein talin, under physiological conditions. Lee and colleagues demonstrate that realistically transmitted force acting on focal adhesion protein talin leads to a conformational change that exposes the cryptic Vinculin-binding residues of vinculin-binding site 1 (VBS1) [85].

1.3 Fluorescence microscopy techniques

The intracellular environment is a dynamic hub of activity, with proteins, nucleic acids, lipids and ions in constant flux, performing their predefined tasks and striving to maintain homeostasis. In order to uncover its biochemical underpinnings, researchers are interested in probing the natural cellular environment with as little disruption as possible to its physiological state. With this comes also a desire for interrogation at a higher spatial and temporal resolution, down to the nanometer size scale and nanosecond time scale. Since the days when van Leeuwenhoek first used the microscope to observe bacteria in pond water and blood cells, microscopy in the most general sense seems to have come full circle, where microscopy is again a primary method for observing and investigating biological samples. With the development of genetically coded dyes like green fluorescent proteins (GFP) [146] and variants [2, 27, 132], it is now possible to create fusions of fluorescent proteins with the various molecules of interest, and to monitor its interactions within the cell. In this thesis, we employ two main fluorescence techniques, Förster (Fluorescence) Resonance Energy Transfer (FRET) and its corollary, Fluorescence Lifetime Imaging (FLIM), as well as Fluorescence Correlation Spectroscopy (FCS).

1.3.1 Phenomena of Fluorescence

Fluorescence occurs when electrons in excited singlet states return to the ground state and expend energy by radiation [81]. The average residence time in the excited state is termed its lifetime, and is defined as

$$\tau = \frac{1}{k_r + k_{nr}} \qquad 1$$

where k_r is the radiative rate constant, and k_{nr} is the non-radiative rate constant [81]. Thus fluorescence intensity decay, $F(t)$, follows an exponential decay law

$$F(t) = F_0 e^{-t/\tau} \qquad 2$$

where F_0 represents the fluorescence intensity at time $t = 0$.

1.3.2 Two-photon excitation fluorescence microscopy

In conventional one-photon techniques, UV or visible light is used to excite fluorescent molecules from the ground to excited state. In two-photon techniques, two less energetic photons are simultaneously absorbed to produce this transition. This is depicted in the Jablonski diagram presented in Figure 6(a) and (b) taken from [134]. The existence of the two-photon effect was predicted in 1931 by Maria Göppert-Mayer [57]. This non-linear feature of excitation results in absorption only near the focal plane, where photon flux is highest, localizing the excitation spot in 3D. This is in comparison to the linear one-photon excitation technique that results in fluorescence all along the laser path (Figure 6(c)). This inherent 3D localization minimizes specimen photodamage. Another key advantage to two-photon fluorescence is the greater penetration depth achieved due to the reduced scattering and absorption of near IR light in biological samples. Thick

tissue specimens can therefore be imaged. Besides this, because the excitation wavelength is much farther removed from the emission band, efficient filtering of excitation wavelengths is possible with minimal signal attenuation.

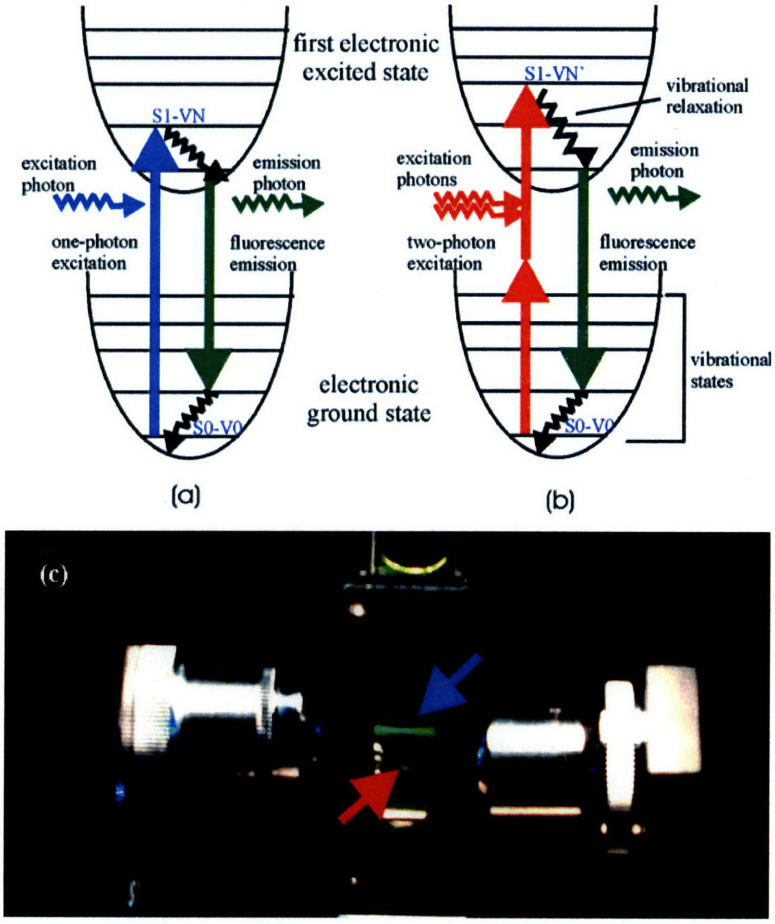

Figure 6 Jablonski diagram for (a) one-photon and (b) two-photon excitation. (c) A comparison of one- and two-photon excitation profiles of fluorescein. One-photon excitation results in fluorescence throughout the laser beam path while two-photon excitation results in a localized 3D spot. Figures reproduced from So et. al.'s review of two-photon excitation fluorescence microscopy [134].

Femtosecond, picosecond, and continuous wave (cw) laser sources have been used for two-photon microscopy, but the most commonly used laser source is pulsed femtosecond titanium-sapphire (Ti-Sapphire) systems. Two-photon excitation requires ultrashort pulsed laser excitation with high peak power, because this second-order process can only be generated efficiently with a high photon flux [134].

Two-photon excitation therefore sets us up well for the measurements we want to carry out. Femtosecond pulsed excitation allows us to build up fluorescence lifetime decays in the form of a histogram of arriving photons, and 3D localization allows us to easily carry out fluorescence correlation spectroscopy (FCS).

1.3.3 Förster (Fluorescence) Resonance Energy Transfer (FRET) phenomena

Though experiments using multiple fluorescent species and conventional epifluorescence microscopy have provided valuable information regarding co-localization of intracellular molecules, the method is not a definitive gauge of the degree of inter-molecule interaction. Regular fluorescence microscopes have a resolution of a few hundred nanometers. Typical protein sizes are on the order of a few nanometers. Thus even co-localization of two different fluorescent signals in the same pixel far from demonstrates molecular level interaction as the proteins are a few hundred times smaller than the pixel. In order to expand upon such co-localization experiments, researchers are increasingly exploiting the phenomena called Förster Resonance Energy Transfer (FRET).

FRET is a non-radiative energy transfer mechanism that occurs through dipole-dipole interaction between two fluorophores of different excitable wavelengths. When donor and acceptor fluorophores are within 10-100Å and conditions related to fluorophore spectral properties, relative dipole orientation, and medium refractive index are met, excitation of the donor leads to energy transfer to the acceptor. A cartoon of the interaction is shown in Figure 7(a) and the Jablonski diagram for the occurrence of energy transfer is depicted in Figure 7(b). Upon the occurrence of FRET, the donor emission is reduced, the acceptor emission increases (Figure 7(c)), and there is a change in the physical parameters governing the phenomena of fluorescence itself, namely a change in the donor lifetime.

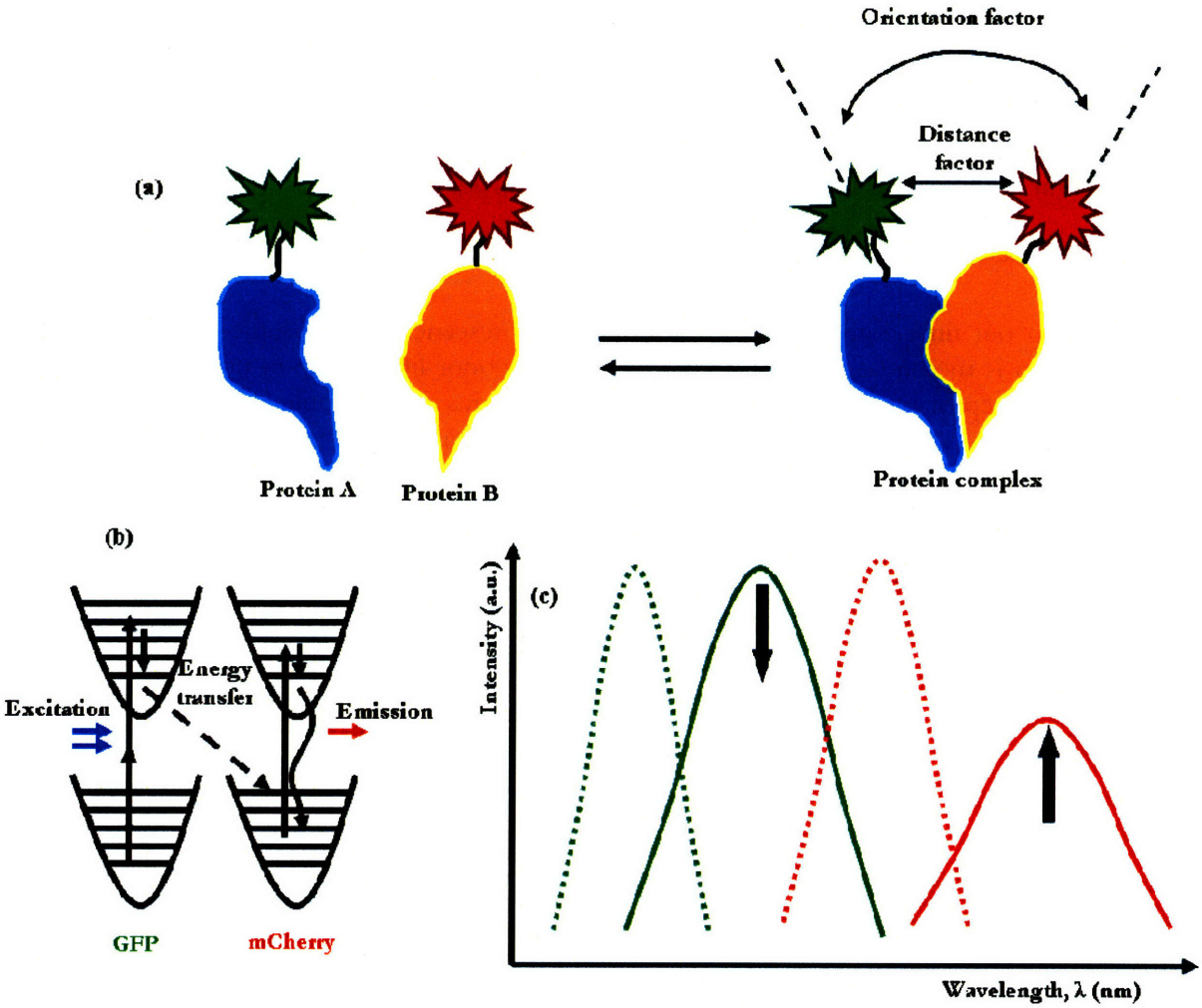

Figure 7 FRET (a) Schematic of inter-protein FRET. (b) Jablonski diagram depicting energy transfer. (c) Overlapping of donor emission spectrum and acceptor excitation spectrum is one factor that leads to FRET, resulting in a decrease in donor emission and an increase in acceptor emission.

From the efficiency of energy transfer occurring, inter-fluorophore distance, R, can be calculated as

$$E = \frac{R_0^{\,6}}{(R_0^{\,6} + R^6)} \qquad 3$$

where E is the efficiency of energy transfer and R_0 is the Förster distance [45]. Since this phenomenon is distance-sensitive and energy transfer efficiency decays with the sixth power of the inter-fluorophore distance, occurrence of FRET would indicate protein binding, and any small change in protein conformation would lead to a change in inter-fluorophore distance and subsequently to measurable changes in donor fluorophore lifetime [145].

Methods used to detect the presence of FRET and deduce binding include ones based on donor intensity measurements with various steps to correct for spectral bleed-through (e.g. the three-filter cube approach [11, 24] and the acceptor photobleaching approach [150, 169]), ones based on

spectral imaging microscopy to measure a complete per pixel emission spectrum [13, 63, 141], ones based on fluorescence polarization anisotropy measurements that compare the orientation of excited and emitting molecules [29, 90, 98, 123], and ones based on monitoring changes in a donor's fluorescence lifetime either in time-domain [55, 99, 114, 115] or in frequency-domain [28, 60, 114, 150, 154]. Our method of choice is fluorescence lifetime imaging (FLIM).

1.3.4 Fluorescence Lifetime Imaging (FLIM), the corollary of FRET

When carrying out time-domain FLIM, the donor's fluorescence decay profile upon femtosecond pulse excitation is measured, and the shortening of the donor lifetime upon occurrence of FRET, via the donor-acceptor interaction, can be calculated from this decay profile [45]. This is depicted in Figure 8. The major strength of FLIM measurements compared to intensity-based measurements is that it provides FRET parameters (i.e. energy transfer efficiency, inter-fluorophore distance, and ratio of FRETting to non-FRETting donors) independent of fluorescence intensity or local probe concentration. Considering also the increasing availability of commercial user-friendly systems for carrying out FLIM measurements [157], it is no surprise that the number of FRET/FLIM papers published has increased in recent years [45, 155].

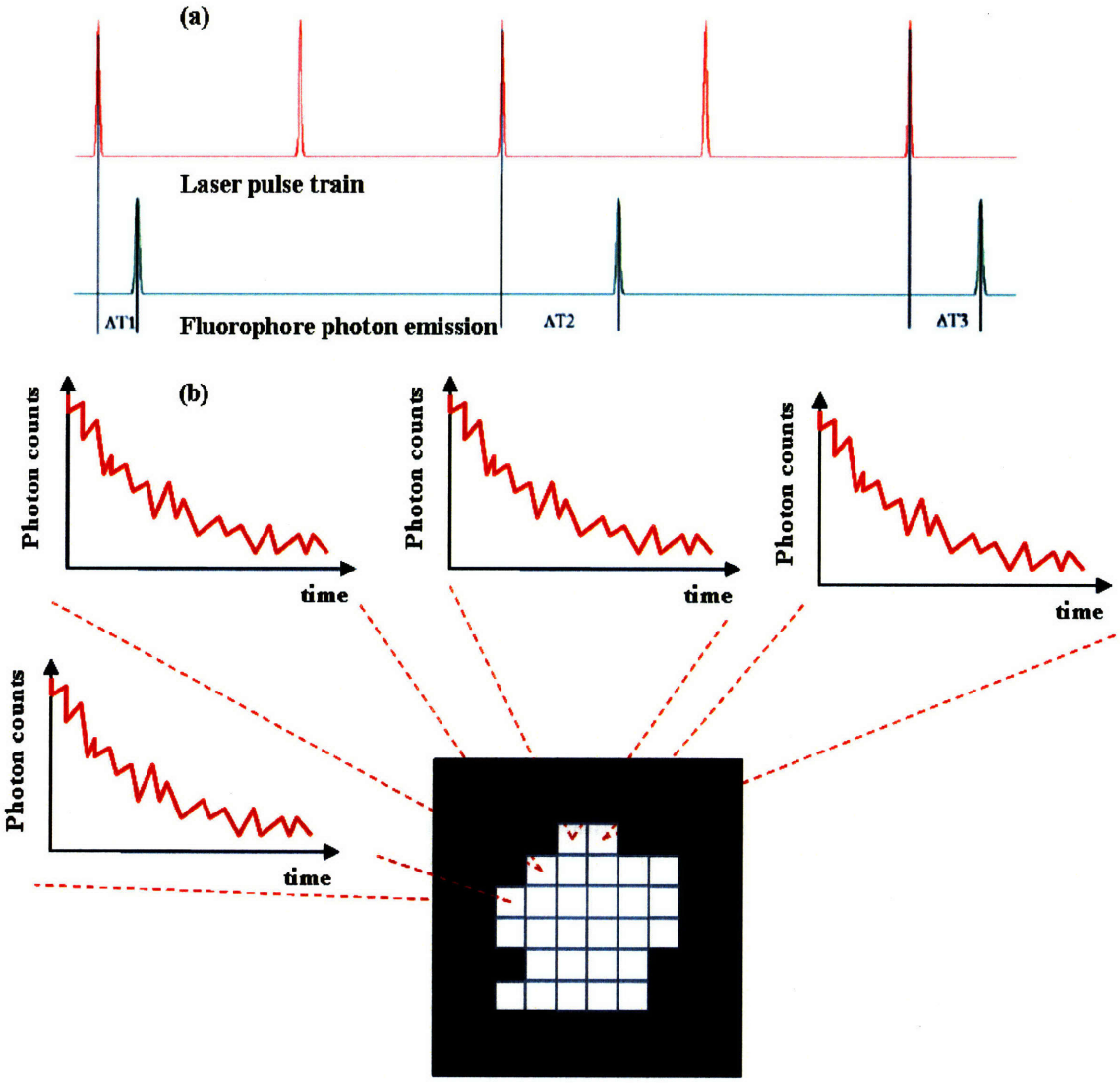

Figure 8 Lifetime histogram. (a) The time interval, ΔT, between the laser excitation pulse and the fluorophore photon emission is kept track of. (b) A histogram of time intervals is collected for each pixel within the image. The time constant of the resulting decay curve represents fluorescence lifetime.

Fluorescence lifetime is defined as the average electron residence time in the excited state [81]. Upon the occurrence of FRET, donor fluorophores acquire an additional non-radiative decay pathway, which adds to the non-radiative rate constant and reduces lifetime. FLIM measurements are carried out by exciting only donor fluorophores within the system. Fluorescence decay curves are collected on a per-pixel basis where the fluorophore population consists of both FRETting and non-FRETting donors. Therefore in a FRET system with only one donor population and one acceptor population present, the total per-pixel fluorescence intensity decay measured is

$$I(t) = \int_0^t G(t-T)\{\alpha_D e^{-T/\tau_D} + \alpha_F e^{-T/\tau_F}\}dT \qquad 4$$

where $I(t)$ is a convolution of the sum of the exponentials with the instrument response $G(t)$. The pre-exponential factors α_D and α_F reflect fractional contributions to the total fluorescence from the FRETting and non-FRETting donor species respectively, each of which undergoes decay at rates τ_D and τ_F. The pre-factors are expressed here in terms of $\alpha_F/(\alpha_D + \alpha_F)$, the ratio of FRETting GPax to total GPax, and termed FRET ratio (FR). The efficiency of the energy transfer process that occurs during FRET, E, can be written in terms of lifetimes and also in terms of molecular separation between donor and acceptor, r.

$$E = 1 - \frac{\tau_F}{\tau_D} = \frac{1}{1 + (\frac{r}{R_0})^6} \quad 5$$

R_0, the Förster radius, is the interfluorophore distance when energy transfer is 50% efficient. R_0 depends on the donor quantum yield, Q_D, the overlap integral J, the orientation factor κ and the index of refraction of the medium n [48].

$$R_0^6 = \frac{9000\ln(10)\kappa^2 Q_D}{128\pi^5 N_A n^4} J \quad 6$$

J represents the overlap between donor emission and acceptor excitation spectrums, and κ is usually set to 2/3, representing a random relative orientation between the transition dipole of the donor and acceptor molecules. R_0 is on the order of 50 to 60 Å for well-matched fluorophore pairs [112, 163].

1.3.5 Principles of Fluorescence Correlation Spectroscopy (FCS)

Fluorescence correlation spectroscopy (FCS) reveals information hidden in the fluctuation signal from fluorescence molecules traversing an observation volume. The technique was described by Magde, Webb, and Elson in the 1970s where they were interested in measuring the diffusion and chemical dynamics of DNA-drug intercalation [41, 94]. The diffusion of fluorescence molecules into and out of the observation volume results in a trace of fluctuation fluorescence intensity over time, $F(t)$. This trace looks random to the naked eye. However, a calculation of the normalized temporal autocorrelation of the trace, $G(\tau)$, a measure of its self-similarity, results in the ability to extract information related to processes that give rise to fluctuations. Parameters that can be recovered include concentrations, mobility coefficients, and characteristic rate constants of both inter- and intramolecular reactions. A plot of $G(\tau)$ against the time interval τ, gives us information about the time scale(s) of the signal fluctuations.

For *in vitro* systems, FCS is routinely used for measuring photodynamics of GFP [64, 127], binding kinetics and equilibrium [14, 162], and protein oligomerization [109]. FCS has been used to investigate the translational diffusion of lipids in single bilayer systems [9, 80]. Carrying out intracellular FCS is more challenging due to the presence of autofluorescence, photobleaching of dyes in restricted compartments, degraded signal-to-noise ratios due to scattering, and cell damage [126]. The first application of two-photon molecular excitation to FCS was by Berland, So and Gratton [10], where they measured the translational mobility of latex beads in the cell cytoplasm.

More recently, in order to understand barriers to drug delivery in tumors, transport parameters in tumors were measured [6].

The normalized temporal autocorrelation function, $G(\tau)$, is given by

$$G(\tau) = \frac{\langle \delta F(t) * \delta F(t+\tau) \rangle}{\langle F(t) \rangle^2} \quad 7$$

where $\delta F(t) = F(t) - \langle F(t) \rangle$ and $\langle F(t) \rangle = \frac{1}{T}\int_0^T F(t)dt$. In a system where fluctuations arise solely from freely diffusing fluorescence molecules, the autocorrelation curve can be fit with the following equation:

$$G(\tau) = \frac{G(0)}{(1+\frac{t}{t_D})\sqrt{1+(\frac{r_0}{z_0})^2 * \frac{t}{t_D}}} \quad 8$$

Where $G(0) = \frac{1}{\langle N \rangle} = \frac{1}{V_{eff}\langle C \rangle} \Leftrightarrow \langle C \rangle = \frac{1}{V_{eff} * G(0)}$, N is the number of particles, V_{eff} is the effective focal volume, $(\frac{r_0}{z_0})^2$ is a measure of the aspect ratio of the focal volume (r_0 = radius, z_0 = height), and τ_D is the diffusion timescale of the molecules, related to the molecule diffusion constant, D, by $\tau_D = \frac{r_0^2}{4D}$.

Poisson statistics governs the measurement of the number of molecules contained within the observation volume. Thus the root mean square fluctuation of the particle number, N, is given by

$$\frac{\sqrt{\langle (\delta N)^2 \rangle}}{\langle N \rangle} = \frac{\sqrt{\langle (N - \langle N \rangle)^2 \rangle}}{\langle N \rangle} = \frac{1}{\sqrt{N}} \quad 9$$

In order to record large fluctuations, the number of measured particles has to be small. However, the fluorescence signal has to still be higher than background noise. Too few molecules will result in an empty observation volume. According to Schwille and Haustein [128], the temporal average of the particle number should therefore between 0.1 and 1000, corresponding to optimal concentrations within the nM region. Thus when carrying out intracellular FCS, it is important to select cells that are fairly dim in order to measure sufficient relative intensity fluctuation for autocorrelation decay curves with good SNR.

1.4 Designing a model protein system

Our proteins of interest are paxillin and FAK. FAK's C-terminal focal adhesion targeting (FAT) domain is responsible for localizing it to integrins at focal contacts and retains this functionality even if separately expressed in cells (unpublished data). Therefore, in order to further simplify our system, we work with FAT and paxillin fusion proteins. FAT is a four alpha-helix bundle with two hydrophobic sites available for binding with LD domains of paxillin or talin [51, 65]. The only significant phosphorylation site on FAT is Y925. It seems that FA localization and Y925 phosphorylation are mutually exclusive as the bundle integrity that is essential to localization prevents Y925 from being phosphorylated [51, 118]. Therefore, if Y925 phosphorylation is important in force-related FA events, kinase inhibition would delineate this effect. In our computational system, only the LD domain of paxillin is available as a crystal structure. Therefore MD simulations are carried out on the FAT-LD complex. For our experimental system, the complete globular paxillin is used. Refer Figure 9(a) and (b).

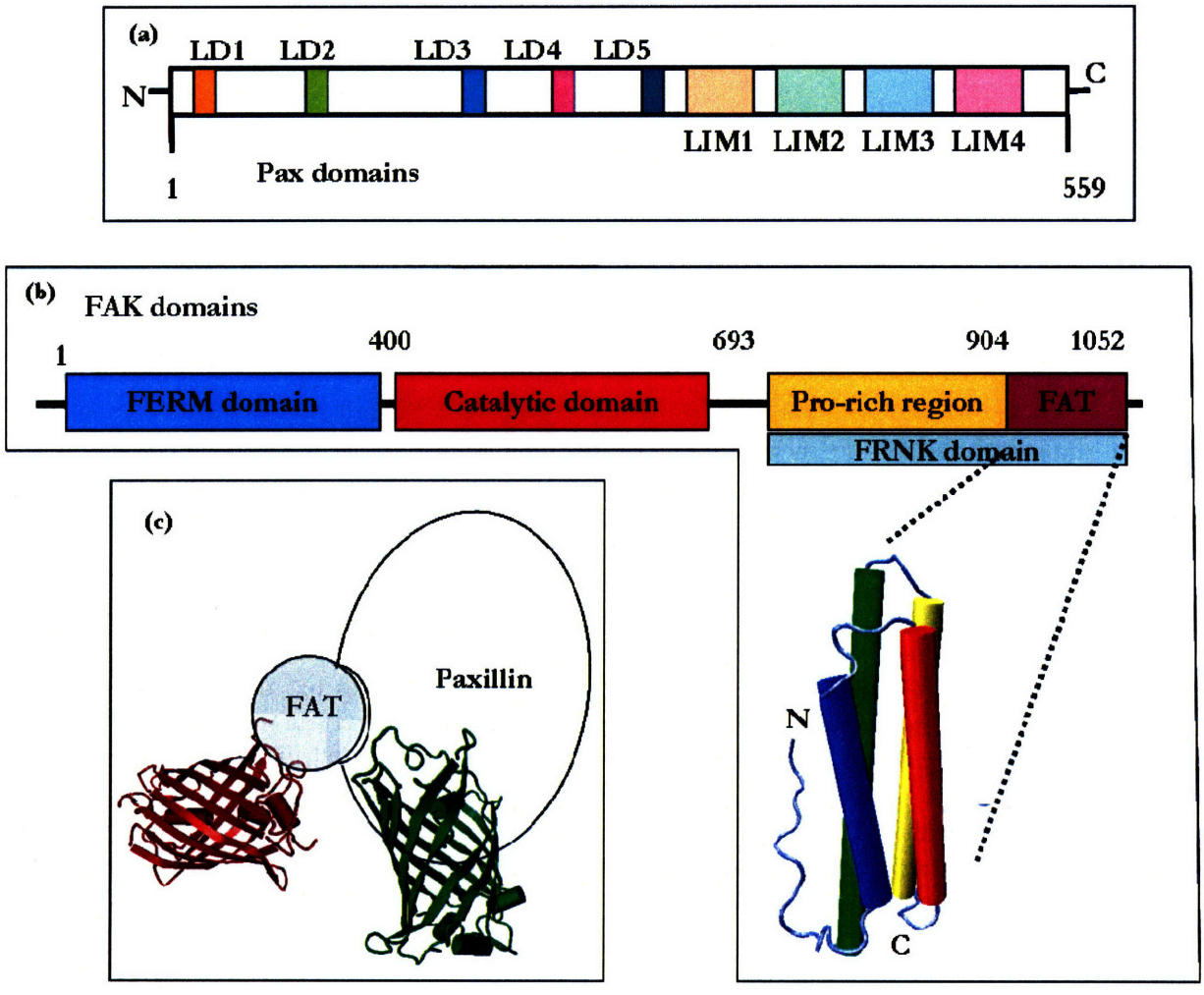

Figure 9 Schematic of our Paxillin – FAT system. (a) Domains within paxillin. (b) Domains within FAK. (c) Cartoon of bound FAT-mCherry and GFP-Paxillin.

Figure 10 shows another schematic of focal adhesion protein interactions. While paxillin has on the order of 15 binding partners, FAT's only other binding partner is now talin. Therefore, a likely scenario for these two proteins to bind in the cell would be FAT hanging off on one side of paxillin, which is recruited to FAs through its other binding partners. While it is still possible that the FAT-Pax complex is directly in the line of force transmission through integrins and into the cell, it is also possible that the FAT-Pax complex is no longer in the transmission pathway, but is affected by external force application through an indirect route, for example by enzymatic soluble factors.

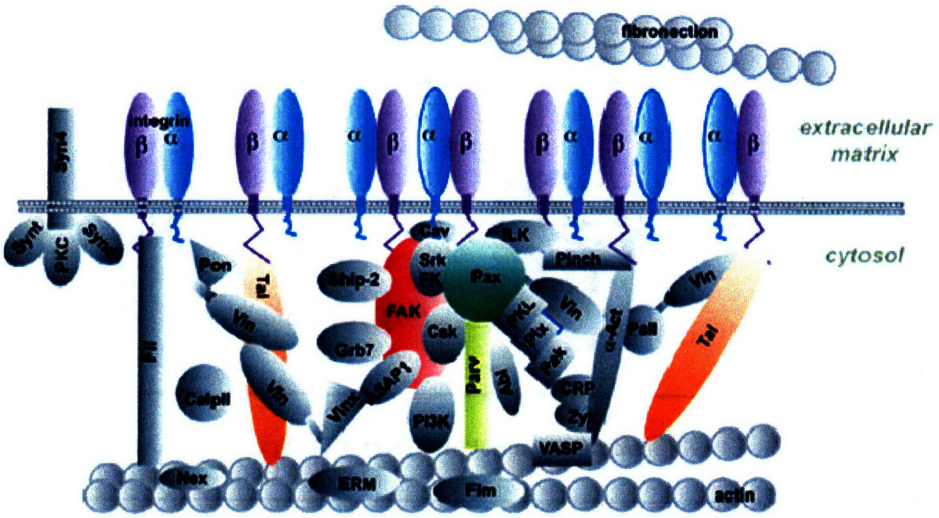

Figure 10 Some of the proteins and interactions observed in focal adhesion complexes. Figure and subtitle reproduced from http://www.bioch.ox.ac.uk/aspsite/research/brochure/Noble/.

The ability to genetically fuse fluorescent proteins to host proteins in frame has allowed active and passive monitoring of these proteins' activity within cells [146]. Fusion at either the N- or C-terminal is possible, with the expectation that the host protein is able to retain its biological role within the cell. For our experimental system, we utilize GFP-Paxillin (GPax) and FAT-mCherry (FATmCh) fusion proteins (Figure 9(c)), N-terminal and C-terminal fusions respectively. Plasmids coding for the fusion protein are introduced into bovine aortic endothelial cells (BAEC) by transfection where the formation of cationic complexes facilitates incorporation of plasmids into the cells. The cells' protein synthesis machinery then takes over and churns out these proteins.

As a result of fusion protein overexpression, by and large these proteins would be either free or bound to each other. This is certainly true when comparing the expression of endogenous paxillin and FAT to fusion proteins GPax and FATmCh, as seen in the Western Blots of Figure 11. Blots were carried out on BAEC, either non-transfected or double-transfected. Transfection efficiency was 10%. For FATmCh, it is clear that endogenous protein expression is many times lower than fusion protein expression. For GPax, endogenous protein expression is quite high. Comparing blot intensities however, even if the total amount of endogenous paxillin was the same as GPax, because GPax essentially came from only 10% of cells, GPax expression is at least ten times higher than endogenous paxillin. While this says nothing about the relative expression of other endogenous proteins compared to fusion proteins, it is probably safe to assume that there is much more fusion proteins than endogenous proteins. We therefore think of double-transfected cells as being largely a system of interacting GPax and FATmCh which can exist in only two pools, free or bound to each

other. The binding equation is thus $GPax + FATmCh \leftrightarrow GPax - FATmCh$. This is depicted in Figure 12.

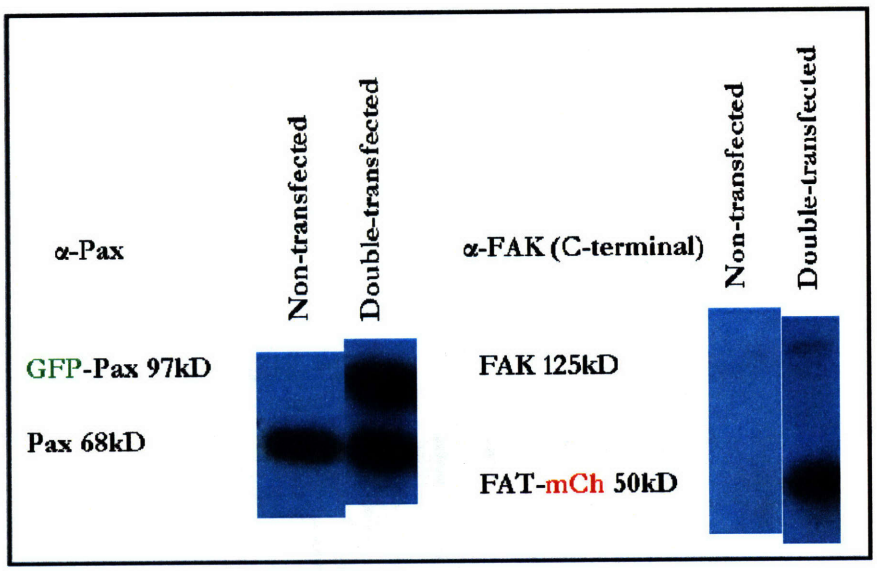

Figure 11 Western blots against Paxillin and C-terminal of FAK (FAT). Transfection efficiency was 10%.

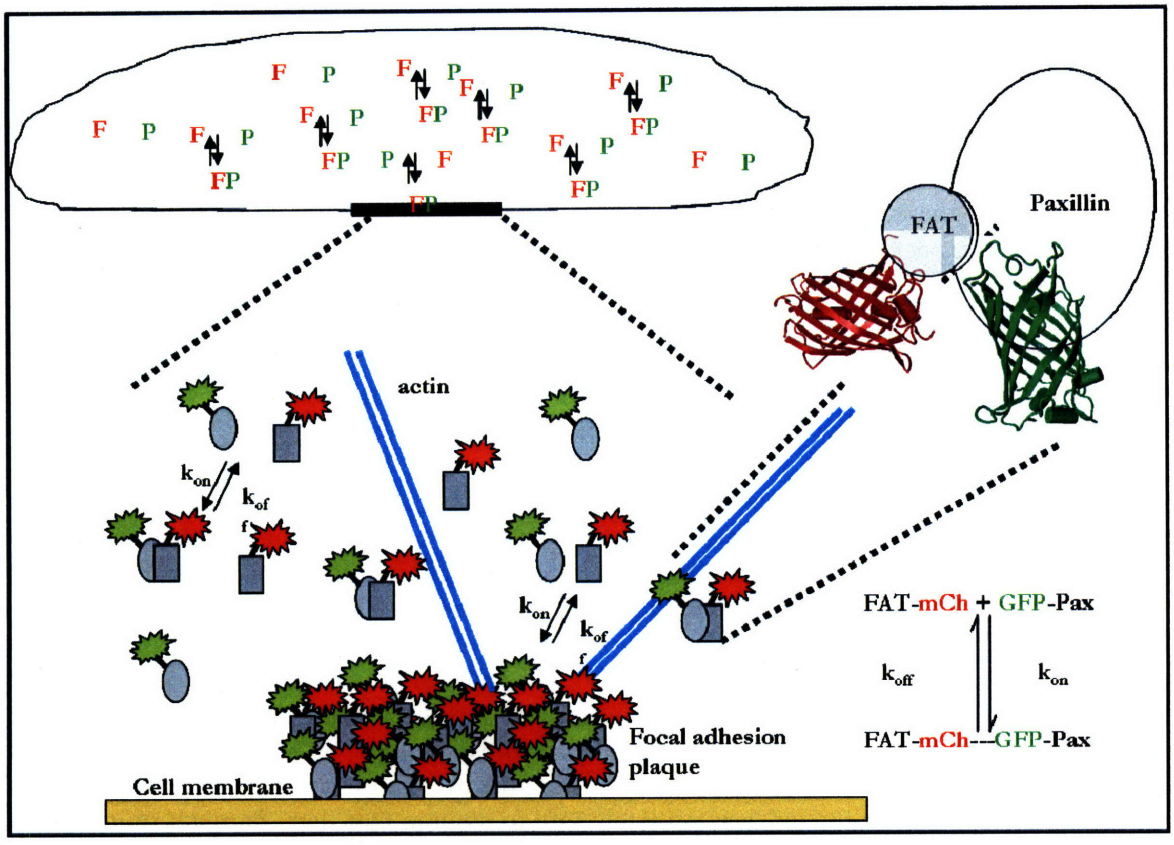

Figure 12 Cartoon depicting double transfected cells containing GPax and FATmCh that interact to form complexes with binding interaction $GPax + FATmCh \leftrightarrow GPax - FATmCh$.

In this work we examine the idea of conformational change as it is applied to protein pairs GPax and FATmCh. Chapter 2 examines the atomistic details of this interaction using MD simulation. The following two chapters detail how two-photon fluorescence microscopy techniques are used to calculate the dissociation constant for the intracellular interaction of this protein pair. Technical aspects related to the global algorithm used, and methods developed to maximize information extraction from noisy data are covered in Chapter 3, whereas the complete application of microscopy and mathematical techniques on measured cellular data is explained in Chapter 4. The change in interaction behavior with external force application is also measured in Chapter 5. Since it is also known that phosphorylation can cause a conformational change of proteins [12, 138], it is thus important, when studying the mechanism of conformational change in our pair of FA proteins, to try and tease apart the difference between conformational change directly caused by force application and that caused by phosphorylation. The work concludes with considerations of future directions in Chapter 6.

Chapter 2 Molecular Dynamics Simulation

2.1 Introduction

Studies of cells' responses to mechanical stimuli can be carried out at the tissue, cellular, and molecular level. Interrogation at different levels leads to different sets of information. From tissue-level experiments come the understanding of more global systemic effects, for example effects related to overall capillary size and geometry modifications. Cellular-level experiments illuminate finer details related to cell-cell interactions in a smaller radius of influence and signaling cascades within cells, while molecular-level experiments lead to understanding of the effects and influences at the single molecule scale. Molecular dynamics simulation is a method used to study molecular-level interactions and effects. The crystal structure of FAT and the LD domains from paxillin that bind to FAT are available from the Protein Data Bank [66]. Starting with this information, we are therefore able to probe the mechanics of FAT-Pax interaction by looking at the protein interface and changes in this interface and overall 3D structure, with externally applied perturbations.

A previous SMD simulation had been carried out to examine the binding interaction between FAT and LD domain, the 12-residue alpha helix from paxillin that is known to bind to FAT [102]. In this study, the N-terminal C-α atom of FAT was fixed and a constant force was applied to the C-terminal C-α atom. SMD was carried out on unbound FAT (nb-FAT), as well as on FAT bound to LD-domain (FAT-Pax). Results showed that at 75pN, nbFAT completely unraveled after going through intermediate configurations, whereas FAT-Pax stayed unperturbed. At the higher force of 85pN, FAT-Pax does unravel, with the hydrophobic face where the LD motif binds being the last to unfold. These results indicate that the presence of the LD motif strengthens the overall integrity of the 4-helix bundle of FAT. Though this is very interesting information, it is unlikely that in the intracellular environment FAT would experience a sustained force that pulls it apart end-on-end and causes unraveling. In order to determine a more realistic mode of protein deformation, normal mode analysis (NMA) is employed. NMA has been previously shown to be useful for identifying collective domain motions of proteins [19, 96, 139]. The results from NMA are then used to determine a more suitable direction of force application for SMD. By monitoring the effects of force application on the molecular conformation of FAT, we demonstrate that even with this more physiologically relevant pulling direction, the effect of the LD motif on the stability of the FAT helical bundle can be observed.

2.2 Methods

The coordinates of both nb-FAT and FAT-Pax crystal structures obtained from the Protein Data Bank (entry code 1OW8) were used for computation [66]. X-ray crystallography had been used to obtain the protein crystal structure with a resolution of 2.85Å. The FAT region is organized into four alpha-helix bundles of dimensions 60Å x 20Å x 20Å as shown in Figure 13(a), with the helices straight, closely antiparallel and connected by short ordered turns. The bundle is highly compact and symmetrical with a square cross-section and a hydrophobic core known to be highly conserved across all species [65]. Hydrophobic patches, HP1 and HP2, are located on the exposed faces of helix2-helix3 (Hx2-Hx3) and helix1-helix4 (Hx1-Hx4) respectively, as shown in Figure 13(b). The N-

terminal region of paxillin contains five distinct leucine-rich LD motifs of sequence LDXLLXXL, each of which form individual amphipathic alpha-helices with minimal propensity to form secondary structures Figure 13(c) [20]. The crystal structures obtained by Hoellerer and colleagues show the ability of LD2 and LD4 to bind to either HP1 or HP2. Residues were renumbered 1-126 for FAT and 1-16 for the LD motif. This is a good model system to analyze as α-helices and four-helix bundles are ubiquitous motifs in folded protein structures.

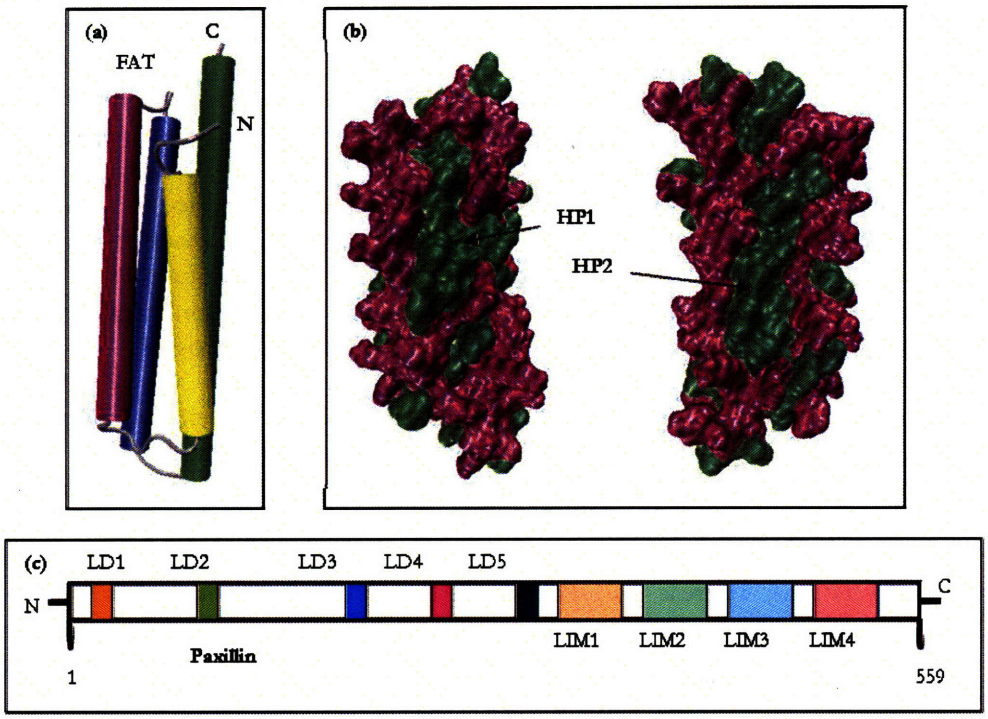

Figure 13 FAT: Four compact alpha-helical bundles. Straight, antiparallel and connected by short, ordered turns. 60Å long with a square cross-section of dimensions 20Å x 20Å. (b) FAT: molecular surface showing hydrophobic patches, HP1 and HP2. Top: as seen (a) but rotated 90° anti-clockwise about a vertical axis running through the 4-helix bundle. Bottom: as seen in (a), but rotated 90° clockwise about the vertical axis running through the 4-helix bundle. (c) Paxillin: positions of LD and LIM domains.

2.2.1 Normal Mode Analysis

To address more physiologically relevant conformational changes that could occur within the FAT domain, we used normal mode analysis to determine the natural modes of oscillation of the FAT bundle. This would allow us to apply more plausible forcing directions on the bundle. In normal mode analysis (NMA), the protein is modeled as a collection of masses (atoms) and springs (interactions), while the electrostatic and Van der Waals forces are ignored. NMA has proven useful for the identification of collective domain motions of proteins where some of the lowest-frequency normal modes of several proteins have been found to correlate well with the proteins' conformational change [96].

Commercial molecular dynamics software, CharmM (Harvard University, Cambridge, MA) [19] was used to carry out normal mode analysis-related simulations. For system minimization and equilibration, an integration time step of 1 fs was used and the ACE parameters were IEPS 1.0

(dielectric constant for space occupied by the molecule), SEPS 80.0 (dielectric constant for the solvent that is treated as a continuum), ALPHA 1.2 (Gaussian density distribution used to determine atom volume) and SIGMA 3.0 (scaling value for hydrophobic contribution to ACE). Non-bonded van der Waals and electrostatic interactions were treated with cut-off by using a switching function between 6.5 Å and 7.5 Å.

The system was minimized using the Adopted Basis-set Newton-Raphson (ABNR) method for 1000 steps with no atoms fixed, to a sufficient GRMS of 0.32. Since the initial coordinates obtained from crystal structures typically tend to have bad contacts that cause high energies and forces, the minimization process is needed to find a nearby local minimum. The system was then heated up gradually to 310K in 1000 steps and equilibrated for 1000 steps until the energy was equally distributed throughout the molecule and the structure was stable. The equilibration process helps the molecule escape local minima with low energy barriers.

CharmM command *vibran* was used to carry out vibrational analysis of both nb-FAT and FAT-Pax, with a distance-dependent dielectric coefficient (RDIE) to approximate solvent screening.

2.2.2 Steered Molecular Dynamics

NAMD, a publicly available molecular dynamics simulation software that is efficient when parallelized [116], was utilized for SMD. SMD was developed within NAMD in order to simulate numerically the experimental pulling of proteins for example by atomic force microscope (AFM) or optical tweezers. The force field used was CHARMM22 [93]. A water box of explicit water molecules was constructed around the protein(s), with harmonic boundary conditions applied. The whole system was minimized for 20ps and equilibrated for

For both nb-FAT and FAT-Pax, the N-terminal of FAT was held fixed. A constant angular rotation rate constraint was applied to the top four C-α atoms (pulled atoms) of the four helices of FAT. Each pulled atom is connected by springs to reference atoms that were rotated about the vertical axis running through the centre of the helical bundle, parallel with the helices, up to a maximum of 200°. The pulled atoms therefore followed the reference atoms to an extent, depending on the spring constant assigned to the attaching springs as well as the rotation rate specified. A stiff spring would cause the follower atom to stay true to the reference atom but the details of the trajectory would be lost as all force will be used to pull bonds apart whereas a soft spring would cause the follower atom to lag behind the reference atom and not follow a true rotational trajectory. When the rotation rate is too high, the pulled atom does not respond on the same timescale. It is slow to follow the motion of the reference coordinate. At slower rotation rates, the pulled atom lags behind the reference coordinate by a somewhat constant value, which means that it is able to follow the motion of the reference coordinate fairly well within the same timeframe. Thinking of the protein as a collection of masses, and their interactions being represented by dashpots and springs as in a viscoelastic material, jerking hard on the protein means the dashpot elements will be slow to react and so the pulled atoms do not follow the reference coordinate. Distortion applied at a slow rate allows the dashpot elements time to deform and transmit force to the pulled atoms on the same timescale. A spring constant of 69.5 pN/Å (1 kcal/mol) and constant rotation rate of 0.1 °/ps were chosen in order to reduce the lag between reference and pulled atom, while still maintaining computational feasibility.

2.4 Results

2.4.1 Modes of FAT vibration

From NMA, the resultant first six modes of vibration corresponded to the three modes of translation and three of rotation available to the molecule. The seventh mode of vibration for both structures corresponded to a concerted twist of the 4-helix bundle. This is shown in Figure 14. Looking down the main axis of the FAT bundle, the top of the bundle twists anti-clockwise relative to the bottom of the bundle, which intuitively makes sense. This then allows us to carry out SMD and apply force in such a way as to produce protein distortion in a manner similar to the concerted twisting seen by NMA. Other modes of vibration do not correspond to an immediately recognizable pattern in terms of protein deformation.

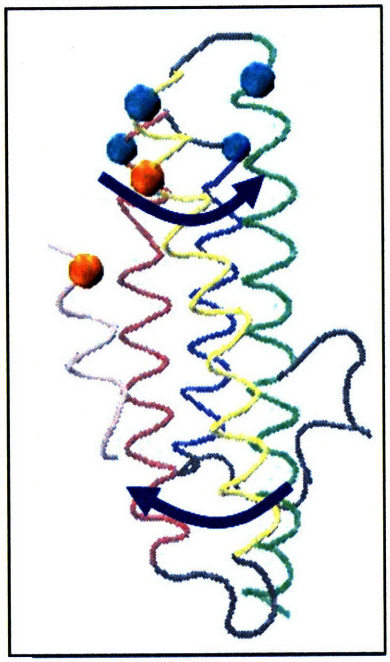

Figure 14 Concerted twisting motion of the lowest frequency mode obtained from normal mode analysis. FAT and paxillin are drawn with 'tube' representation going through the protein backbones. The short pink helix on the left is paxillin. The 'pulled atoms' are represented as blue van der Waals spheres and the orange spheres indicate the atoms paired through salt bridge formation.

2.4.2 Unbinding of LD motif with FAT conformational change

A twisting load was applied to the FAT helical bundle, mimicking its seventh normal mode of vibration. To characterize the binding of the LD motif (LDm) to FAT with the application of this rotation, the distance between residues that form salt bridges between the two proteins, were monitored. The Glu10(LDm)-Lys97(FAT) salt bridge is located at the top of the helix while the Asp5(LDm)-Arg57(FAT) salt bridge is located at the bottom of the complex, as shown in Figure 15(a).

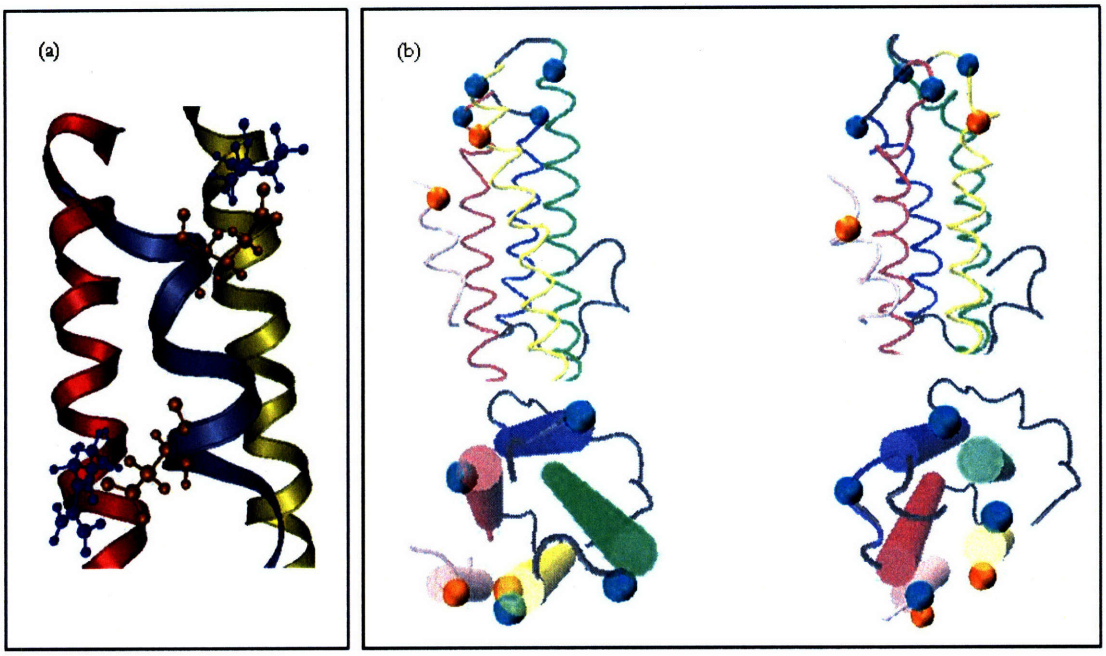

Figure 15 (a) Salt bridges between acidic and basic residues (Glu10(LDm)-Lys97(FAT), Asp5(LDm)-Arg57(FAT)) stabilize the FAT-Pax complex. (b) Corresponding view of FAT-Paxillin face-on and from the top: at the start of simulations (left) and after 90° rotation (right). The distance between the orange spheres (salt bridge) has increased and paxillin position has changed from being on the HP1 face to being cocked out at an angle as helix 4 'swings'.

Initially LDm closely followed the motion of FAT as the hydrophobic surface HP1 is still intact and binding is maintained, but as FAT is twisted by 90°, HP1 becomes distorted and binding is impaired (Figure 15(b) - left). As FAT is further twisted, LDm departs from the binding face (Figure 15(b) - right), as HP1 is severely distorted. Unbinding occurs in such a way that LDm bends out from the binding face as the face is distorted. Tracking of salt bridge distances show that while the top distance increases, the bottom distance remains unchanged. This corresponds to the observed mode of unbinding where LDm cocks out from the binding face.

Figure 16 plots the top salt bridge distance and lag of the reference atom at the top of helix 3 with increasing simulation time. There are three distinct rates of distance increase. As the reference atom is pulled, intramolecular bonds hold back the pulled atom. When enough force is applied to break the intramolecular bonds, the pulled atom immediately springs back to catch up with the reference atom. Since this corresponds to the moment when the salt bridge distance also increases more rapidly, it indicates that the intramolecular bond that is holding the pulled atom back is the salt bridge. Once the salt bridge is broken, it allows LDm to swing out from the binding face faster than before.

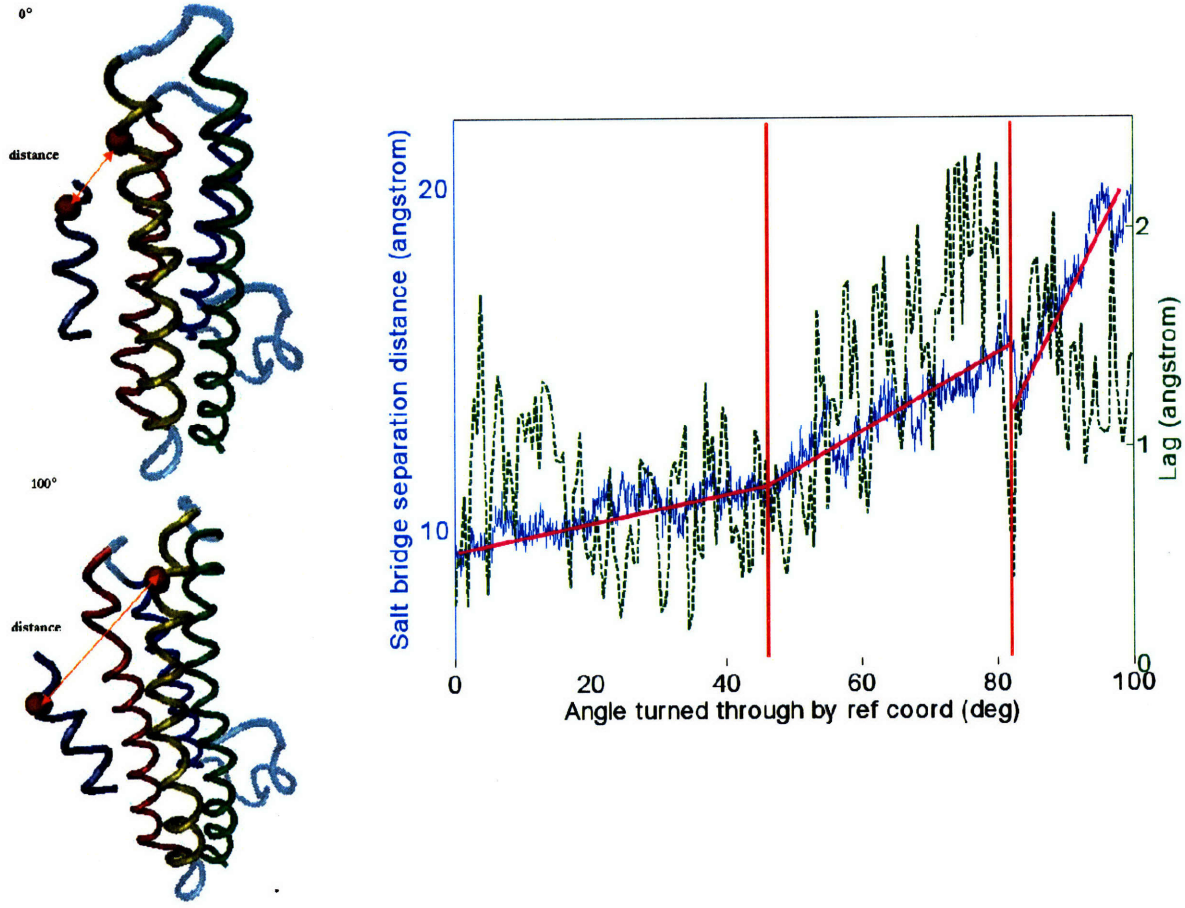

Figure 16 Separation profile of salt bridge distance with angle turned through by the reference atom and corresponding view of FAT-Paxillin face-on: at the start of simulations (top) and after 90° rotation (bottom). The distance between the orange spheres (salt bridge) has increased and paxillin position has changed from being on the HP1 face to being cocked out at an angle as helix 4 'swings' by.

2.4.3 Stabilizing effect of LD motif

In order to study the stabilizing effect of LDm on the FAT bundle, the movement from their original position of specific atoms on Hx2 and Hx3 are tracked. HP1, the site of LDm binding, lies on the Hx2-Hx3 face. The line colors on the plot of Figure 17 match the colors of the C-α atoms in the diagram of the same figure. The ball-and-stick residues in blue and orange are of the two pairs of salt bridges present in the system. Comparing distance moved of these particular atoms, the atoms in Hx2 move similar distances whether or not LDm is present. However, atoms in Hx3 move larger distances without LDm present. This indicates that binding of LDm is primarily to Hx3, where binding stiffens this helix and does not allow as much movement compared to other helices.

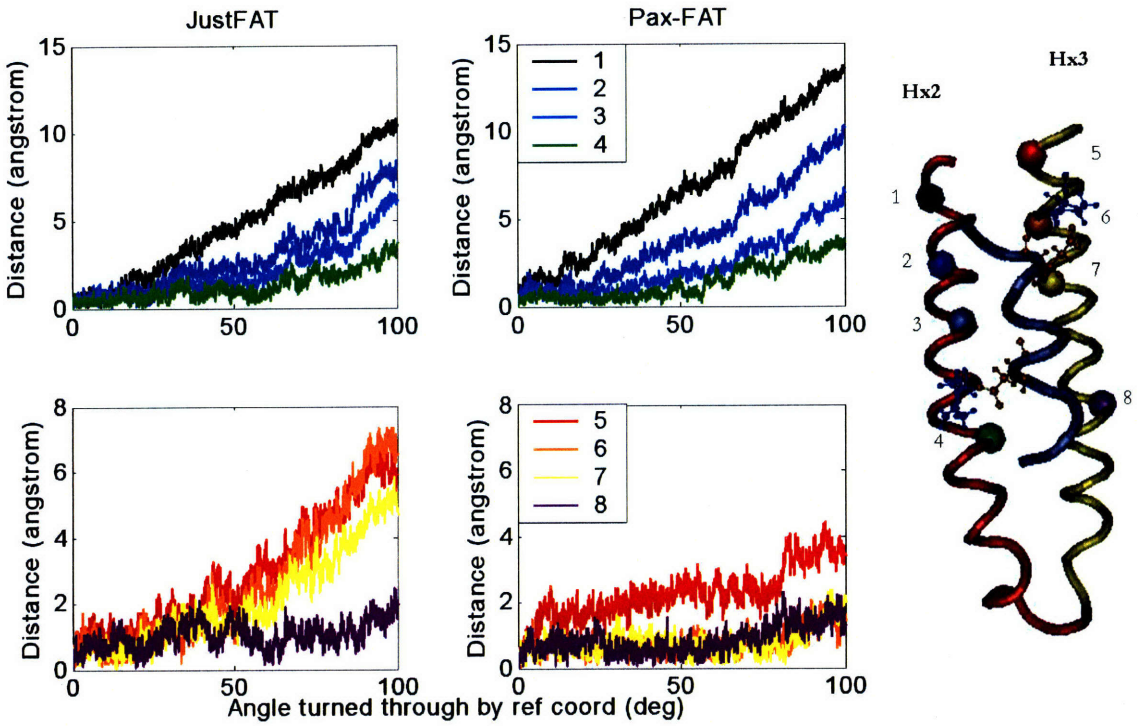

Figure 17 Movement of atoms from initial position with applied twist. Plot line colors match the colors of the C-α atoms shown.

2.5 Discussion

This study seeks to demonstrate that force-induced conformational change in individual proteins is a highly plausible mechanism for transduction of mechanical signals carried via alteration of binding events in the mechanosensing pathways. Our results support the speculation that the integrity of FAT, especially the conformation of HP1, is crucial for its binding to paxillin [65]. Force application that caused a twist in the FAT bundle similar to its seventh normal mode of vibration, eventually remodeled the hydrophobic groove of FAT, affecting the FAT-Pax binding partnership. With the distortion of this hydrophobic patch, LDm is unable to align with HP1 and FAT-Pax binding cannot occur. This indicates that the formation of the FAT 4-helix bundle through alignment of its particular set of amino acids is optimized for promoting the paxillin binding event. While previous work [102] showed that the intactness of HP1 was what facilitated LDm binding, we show that binding is primarily between LDm and Hx3. LDm binding stiffens this helix, retarding its movement compared to other helices. Presumably, the binding signature of LDm to HP2 is similar to its interaction with HP1, though caution should be exercised when extrapolating these results to forces applied at different locations.

A possible physiological scenario would be the concentration of applied force at focal adhesions, causing a twist of the top or 'free' side of the FAT bundle relative to a 'fixed' N-terminal that is connected to the rest of the FAK protein. Conversion of atom lag values to force values leads to force levels of between 50-200pN. Micropipette experiments have shown that concentrated apical cell surface loads of ~10nN initiate focal adhesion complex formation and protein recruitment along the basal cell surface in regions local to the concentrated load [122]. Optical trap experiments

indicated reinforcement of focal complexes into focal adhesions with stress levels of between 1 $nN/\mu m^2$ and 3 $nN/\mu m^2$ [50]. Also, nN level forces applied to the apical cell surface induce translocation of FAs [92]. These experiments implicate force levels of hundreds of pN per FA, and thus a few pN per integrin, to which FAK connects, as being important biologically. This can be resolved by understanding that the force magnitudes necessary to produce effects on molecules depend on the loading rate [44]. Within cells, the magnitude of a few pN forces experienced, caused either externally by arterial shear stress and solid dynamics or internally through cytoskeleton reorganization, occurs over a matter of milliseconds to seconds. This is equivalent to a very slow loading rate. For our simulations however, the short simulation times imposed by the limitations of computer resources requires that FAT be distorted with forces one to two orders of magnitude higher than forces present in the cellular environment. We can therefore only hope to achieve such simulation timescales if there were vast improvements to computational techniques.

2.6 Conclusion

We have shown that analysis of the natural vibrational modes present in a protein system leads to identification of more relevant protein distortion pathways as compared to end-to-end pulling inherent in force simulations that try to mimic atomic force microscopy (AFM) or optical tweezers techniques. Force application that persuades the protein to distort along its normal mode of vibration leads to a better understanding of the importance of the hydrophobic binding site and delineates key residues that facilitate binding. Even with the shortcomings regarding magnitudes of applied force, the present work demonstrates that force-induced conformational change in individual proteins is a highly plausible mechanism for transduction of mechanical signals carried via alteration of binding events in the mechanosensing pathway. Force application eventually remodeled the hydrophobic groove of FAT, affecting the FAT-Pax binding partnership. Putting this in the context of the cell, unbinding might in turn cause disruption of downstream signaling pathways.

NAMD was developed by the Theoretical and Computational Biophysics Group in the Beckman Institute for Advanced Science and Technology at the University of Illinois at Urbana-Champaign.

Chapter 3 Methodological Considerations for Interpreting Cellular FLIM / FRET Measurements

3.1 Introduction

With the development of genetically encoded fluorescent proteins [146], the interrogation of protein dynamics within cells has been greatly facilitated. Besides being used to track protein localization and trafficking, the ability to introduce fluorescent proteins of different colors into cells has allowed closer investigation of protein-protein interaction in its native intracellular environment. A method widely used is FRET, Förster Resonance Energy Transfer, where excitation of the donor species results in excitation also of the acceptor species, resulting in a scheme for quantifying protein interaction. Fluorescence Lifetime Imaging (FLIM) is a technique that quantifies FRET-based protein interaction by measuring the fluorophore lifetime. This technique is increasingly being used due to the rapid development in commercially available instrumentation [149]. FLIM measurements are independent of local fluorophore intensities or concentrations, making it easier to use and more quantitative compared to intensity-based methods for quantifying FRET [45].

Some problems abound in the interpretation of FLIM-FRET data on the cellular level. These stem from the fact that the lifetimes of bound and free donors are often relatively close and must be resolved from donor decay curves that are noisy due to low photon counts. The closeness of the lifetimes depends on the efficiency of energy transfer; lifetimes that are closer together are more difficult to be accurately measured [3, 4]. The requirement of minimal perturbation of intracellular conditions further means that there is a trade-off between high photon counts required for a good signal and low fusion protein concentration for physiologically relevant conditions. Therefore, it is important to formulate a methodology for extracting all the information present in these information-rich but noisy decay curves.

An obvious starting point is to leverage the utility of global analysis and simultaneously fit all decay curves from a particular measurement session to extract the physical parameters of interest. In global analysis methods, *a priori* information is used to significantly reduce the degrees of freedom in the fitting algorithm. It has been shown that global fitting of FLIM, assuming spatially invariant lifetimes, accurately extracts two lifetimes, both for frequency-domain measurements [153, 154], as well as for time-domain measurements [113].

Presented here are methodological considerations for fitting time-domain FLIM data measured in cells in order to recover single lifetimes (τ_D) from non-FRETting samples as well as the second lifetime (τ_F) and the fractions of interacting fluorophores from FRETting samples. We demonstrate an adaptive method for acquiring instrument responses to be used when fitting the decay curves, establish the applicability of global analysis for cell data, and analyze the dependence of accuracy of lifetime fits on total photon counts. As an illustration, we apply these techniques to study the interaction of paxillin and FAT (focal adhesion targeting domain of focal adhesion kinase, FAK); they are cytosolic proteins that localize to focal adhesions (FA), which are sites of cell attachment to the extracellular matrix and play roles in a variety of mechanotransduction processes. Our samples consist of non-FRETting bovine aortic endothelial cells (BAECs) transfected with GFP-Paxillin and FRETting cells co-transfected with GFP-Paxillin (GPax) and FAT-mCherry (FATmCh).

3.2 Theory – global fitting algorithm

The global fitting algorithm developed by Pelet et. al is utilized to fit our fluorescence decay data to the model expressed as eqn. 4 above. In summary, decay curves are scaled to a maximum of one before fitting. The pre-factors are bounded such that $(a_D + a_F) = 1$, but are allowed to vary spatially. It is assumed that only two fluorophores exist in each pixel, non-FRETting and FRETting species, thus the fitted lifetimes are spatially invariant. The least-squares estimate χ^2 is used as a merit function to optimize the values of all fit coefficients

$$\chi^2 = \sum_i \sum_t \left(\frac{(I_i^{model}(t) - I_i^{data}(t))^2}{I_i^{data}}\right) \quad \textbf{10}$$

When fitting single-exponential decay curves, the same algorithm is used but with τ_F fixed at 10^{-12}, essentially setting the pre-factor α_F to zero.

Image segmentation was carried out based on intensity thresholding where pixels of similar intensities were grouped together, and their decay curves summed. A global fit is performed on this very limited set of decay curves [113] (segment-sum) to obtain coefficients that were subsequently used as initial guesses in the final global fitting step (global-indiv). This method of using an educated initial guess of fit parameters was shown to greatly accelerate time to convergence [113]. It is possible to carry out segmentation because Paxillin and FAT are cytosolic proteins that localize to FAs. Images obtained at the basal adhesion plane therefore capture the locations of FAs, which are more intense compared to the rest of the cell area, and can be grouped together.

Figure 18 shows intensity (a) and resultant segmented (b) images of GPax-only and GPax / FATmCh cells. Only pixels with intensities above a threshold of 500 photon counts are selected for segmentation. Several regions identified as FAs in the intensity images are also shown in the segmented images, indicated by pink arrowheads. FAs are brighter in contrast to the cytosol in the surrounding region due to fusion protein localization, but the absolute intensity of FAs is not always the same. FAs in the leading edge (top) of the GPax cell are brighter than the cytosolic region surrounding them, but are of similar intensities as the cytosolic region in the middle of the cell. Intensity segmentation thus assigns both these regions to the same intensity group (orange). FAs in the trailing edge (bottom) of the GPax cell are brighter still compared to the surrounding cytosol, and are assigned to the same intensity group (red).

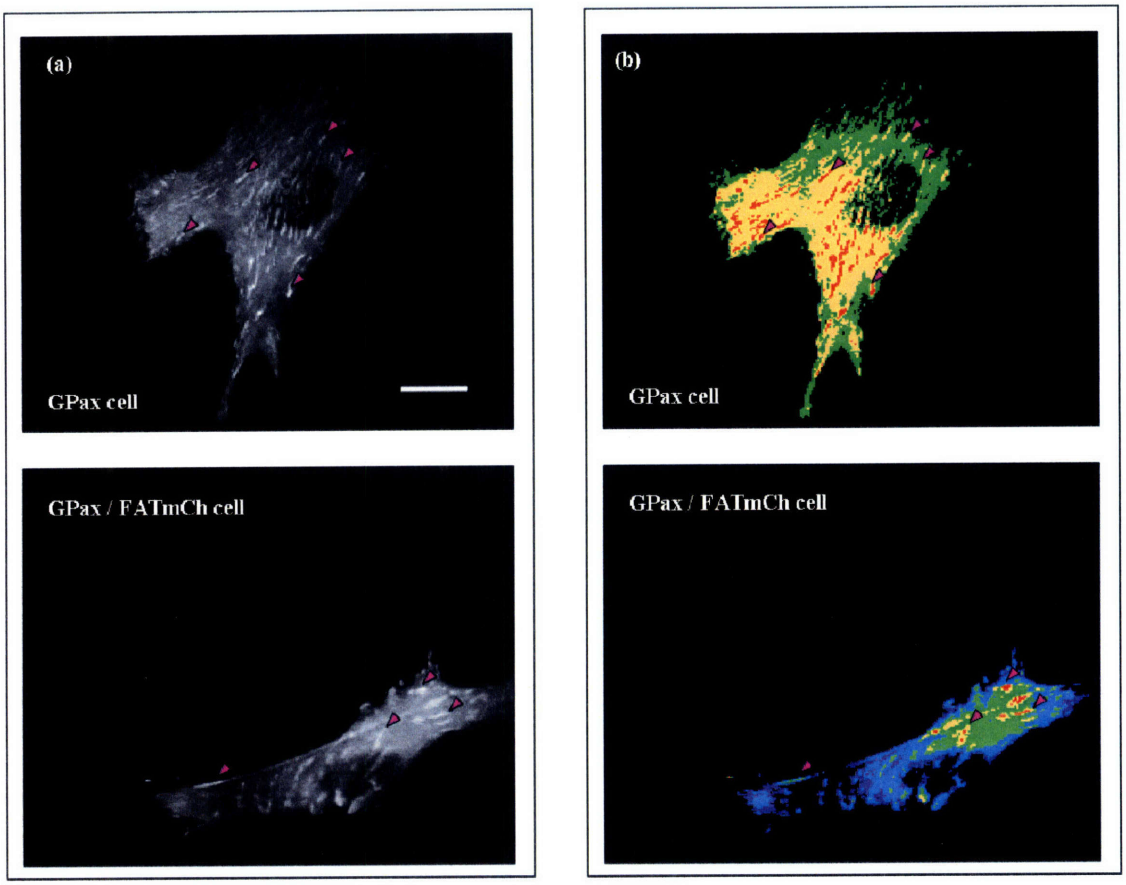

Figure 18(a) Intensity images of GPax (top) and GPax / FATmCh (bottom cells). (b) Images of the same cells in (a), segmented by intensity and arbitrarily colored to distinguish between different intensity segments. Only pixels with LL1000 were selected for intensity segmentation. Scale bar is 10 μm.

Data fitting clearly depends on signal to noise level. Pixels with decay curves consisting of a minimum of 1000 photon counts are selected for fits unless otherwise specified. We express our lower limit in photon count symbolically as LL1000.

3.3 Methods

3.3.1 Cell preparation

Bovine aortic endothelial cells (BAECs) were cultured in Dulbecco's Modified Eagle Medium (DMEM) (Gibco, Invitrogen, Carlsbad, CA) supplemented with 10% fetal bovine serum,1% penicillin/streptomycin, and 1% L-glutamine. Cells were seeded at an initial density of 160,000 cells/well in fibronectin-coated 35mm glass-bottom dishes (MatTek Corporation, Ashland, MA). Plasmids used for transfection were either GFP-Paxillin (gift from K Yamada of the National Institute of Health, Bethesda, MD) or FAT-mCherry (mouse FAT ligated with mCherry into the pcDNA4/HisMax© TOPO® vector (Invitrogen). Cells were transfected at ~80% confluence with either GFP-Paxillin plasmids only or co-transfected with both GFP-Paxillin and FAT-mCherry plasmids, using the FuGene6 transfection reagent from Roche Diagnostics (Indianapolis, IN). Note

that plasmid notation indicates position of fluorophore within the fusion protein, whereby GFP is at the N-terminus of Paxillin and mCherry is at the C-terminus of FAT. Just before imaging, cells were washed with PBS and DMEM supplemented with 10% fetal bovine serum,1% penicillin/streptomycin, and 1% L-glutamine but with no phenol red was replaced in the wells. Lifetime imaging was carried out 24 hours after transfection.

3.3.2 Optical setup

Details of the two-photon lifetime imaging microscope setup have been in So 2001, Pelet 2004, and Pelet 2006 and a schematic is shown in Figure 19. In brief, a custom-built two-photon microscope setup (So 2001) was modified for obtaining lifetime images. This microscope is based on a modified inverted microscope, Axiovert 110 by Zeiss (Göttingen, Germany), with a femtosecond laser source from the Mira family of modelocked Ti:Sapphire oscillators by Coherent (Santa Clara, CA) (Pelet 2004; Pelet 2006). The laser, tuned at 890nm, excites a subfemtoliter volume at the focal point of a 40X Fluar objective (1.3NA, Zeiss). The fluorescence signal from the cell is first selected with a short-pass Schott BG-39 filter and short-pass 700nm filter from Chroma (Rockingham, VT), which minimized contributions from scattered light and autofluorescence, before being sent to the top port of the microscope where it is filtered for green wavelengths with HQ500LP from Chroma (Rockingham, VT). A photomultiplier tube (PMT), R7400P from Hamamatsu (Bridgewater, NJ), detects emitted photons and this signal is sent to a time-correlated single photon counting card (TCSPC card), SPC-730 from Becker-Hickl (Berlin, Germany).

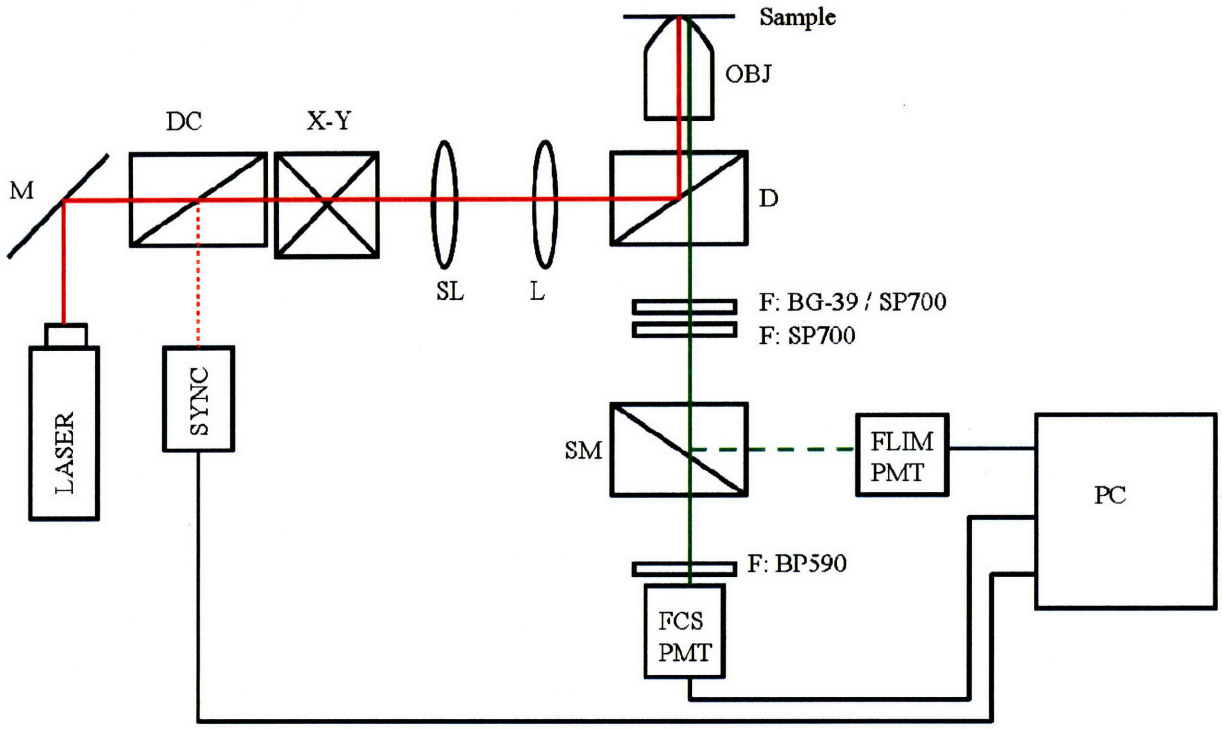

Figure 19 The two-photon scanning microscope has both FLIM and FCS capabilities. M: silver mirror, DC: dichroic mirror, X-Y: galvanometer scanning mirrors, SL: scan lens, L: lens, D: dichroic mirror, OBJ: objective; F: filter; SM: sliding silver mirror, PMT: multi-anode photomultiplier tube, PC: computer.

3.3.3 FLIM imaging

The IR of the system was measured using either fluorescein (flsn) in a well-slide or Gallium Arsenide (GaAs) crystal glued onto a coverslip. Since flsn has a well-characterized decay of 4.0 ns [40, 79], the IR can be extracted as a Gaussian that best fits the fluorescein decay curve with a preset decay time of 4.0 ns. For GaAs, the second harmonic generation (SHG) signal from the GaAs surface is instantaneous, thus directly giving us the IR.

Cells selected for FLIM imaging were those in the middle range of fluorescent intensities as observed using epifluorescence with a 488 nm Argon ion laser (MWK Industries, Austin, TX) or 432 nm diode laser (Laserglow Technologies, Ontario, Canada).This is a compromise between ensuring a bright enough cell that has sufficient photon counts for decay curves with acceptable SNR, and cells that are not over-expressing the fusion proteins at an enormously high level. The selected cells typically have fluorescent protein with concentration in the nM to μM levels. All FLIM imaging was carried out at 890nm, with a power of 40mW before the objective. At this wavelength, mCherry is minimally excited, with fluorescence levels within the noise range. The power used is low to minimize cell damage and to ensure that photobleaching does not occur. FLIM imaging of transfected cells would thus take 7-8 mins. The microscope was carefully focused to the basal adhesion plane of the cell before carrying out FLIM imaging.

3.3.4 Synthetic decay curves

To test the conclusions derived from fitting of experimental data, sets of synthetic decay curves were generated and fitted with the global fitting algorithm. Decay curves have either a single lifetime (τ_D = 2.6 ns; single-exponential decay) or two lifetimes (τ_D = 2.6 ns, τ_F = 1.3 ns; double-exponential decay). For sets of decay curves containing two lifetimes, the pre-factors within each set were varied such that $0 \leq \alpha_F / (\alpha_D + \alpha_F) \leq 1$. Each decay curve is convolved with a Gaussian instrument response of 0.25 ns, with Poisson noise added to simulate the photon counting process. The total photon counts within decay curves were allowed to vary between 100 and 3000, consistent with typical experimental data, depending on the fitting method being tested.

3.3.5 Computation

The global fitting algorithm as developed by Pelet et. al (2004) was carried out on single IBM processors. The computing code is written in MATLAB (The MathWorks, Natick, MA) and uses the *fmincon* optimization function. Convergence is defined as being reached when χ^2 varies by less than 10^{-15}.

3.4 Results

3.4.1 Instrument response

One way to account for IR is to acquire SHG signal from a surface, in our case GaAs. Since SHG is instantaneous, this method directly gives us the IR. Another method would be to take FLIM data of a sample with a well-characterized lifetime, for example flsn with a lifetime of 4.0 ns. Convolution of a Gaussian to a single-exponential decay of lifetime 4.0 ns and comparing this to the actual flsn data would recover the Gaussian that best depicts the IR. With either method, measurements of the IR (I_{msr}) would typically be taken before carrying out cell measurements and it is assumed that the IR does not vary throughout the imaging session. However, a number of factors in TCSPC microscopy may contribute to substantial variations in I_{msr} such as electronic circuit noise, laser instabilities, or loss of mode-lock and thus alignment. If the IR varies appreciably throughout the imaging session, it is inaccurate to use just one IR for all calculations. Though it would be possible to interleave data collection from sample and reference specimens and collect IR data throughout the imaging session, this is not very practical as it significantly increases data acquisition time and it cannot be predicted when exactly the IR would change.

In order to overcome this problem, an adaptive solution was developed based on the assumption that the mean lifetime can be readily extracted and is an invariant for a homogenous population of cells. The IR is directly extracted from the cell FLIM data (I_{ext}). All decay curves from the 256 x 256 cell image are summed and the IR is calculated by presetting mean lifetimes of τ = 2.7 ns for GPax only cells and τ = 2.3 ns for GPax / FATmCh cells. The Gaussian that, once convolved with a single-exponential decay having the preset lifetime, best fits the master decay curve is used as the IR for that particular image. Variations in preset lifetimes of ± 0.3ns produced negligible variations in

the full width half maximum (FWHM) of the Gaussian IR (data not shown), thus validating our method of direct IR extraction.

A plot of scaled IR showing the difference between IR_{msr} and IR_{ext} for two datasets is given in Figure 20. The solid line plot compares differences between IR_{msr} from flsn and sample IR_{ext} from GPax and GPax / FATmCh cells, whereas the dashed line plot compares differences between IR_{msr} from GaAs and sample IR_{ext}. Slight differences between different IR's can be observed. However, it is not immediately obvious how these differences would be quantified. These slight differences however, are sufficient to produce different fitted lifetime results, especially for double-exponential decays. This is shown in Table 1. When fitting single-exponential decays to GPax curves, both IR methods recover similar lifetimes. However, discrepancies become obvious when fitting double exponential decays to data from double-transfected cells. Fits using both methods produce reasonable-looking fits (data not shown), and in all cases, the χ^2 has been minimized. However, fitting with IR_{msr} was unable to recover the expected two FRET lifetimes, for both GaAs and flsn IR_{msr}. IR_{msr} GaAs recovered lifetimes of τ_D = 2.16 ± 0.13 ns and τ_F = 0.01ns while IR_{msr} GaAs recovered lifetimes of τ_D = 2.30 ± 0.10 ns and τ_F = 0.01ns. In both cases, the recovered τ_D is an average of the two lifetimes recovered using IR_{ext}.

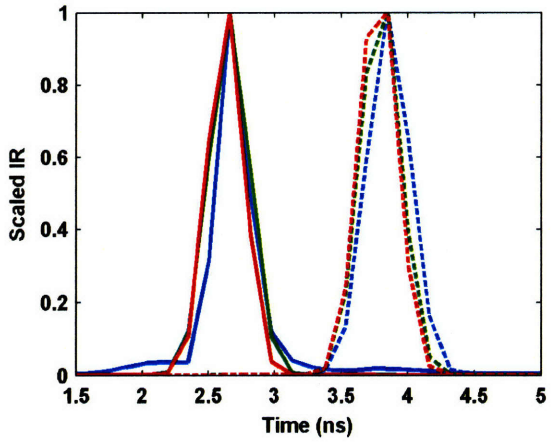

Figure 20 Scaled instrument response (IR) for two datasets. For solid line plot of dataset 1, the blue line is $IR_{msr(GaAs)}$, the green line is $IR_{ext(GPax)}$, and the red line is $IR_{ext(GPax / FATmCh)}$. For dashed line plot of dataset 2, the blue line is $IR_{msr(Flsn)}$, the green line is $IR_{ext(GPax)}$, and the red line is $IR_{ext(GPax / FATmCh)}$. The plot for dataset 2 has been shifted to the right by 1.5 ns, for clarity.

		IR_{msr}			IR_{ext}	
		IR_{msr} method	τ_D (ns)	τ_F (ns)	τ_D (ns)	τ_F (ns)
Single exponential (GPax)	Trial 1 (7 cells)	GaAs	2.31 ± 0.11		2.61 ± 0.08	
	Trial 2 (8 cells)	Flsn	2.48 ± 0.06		2.47 ± 0.06	
Double exponential (GPax / FATmCh)	Trial 1 (7 cells)	GaAs	2.15 ± 0.12	0.01	2.51 ± 0.22	2.01 ± 0.14
	Trial 2 (7 cells)	Flsn	2.30 ± 0.10	0.01	2.56 ± 0.13	1.99 ± 0.08

Table 1 Lifetimes obtained from fits of GPax only cells and GPax / FATmCh cells, using either IR_{msr} (flsn or GaAs) or IR_{ext} .

Our results demonstrate that in order to obtain two relevant FRET lifetimes from double-exponential decay curves, the IR used in fits is important. Since the IR varies throughout the imaging session for our setup, an IR measured at the start of the experiment is rendered invalid for use with data generated later within the imaging session. Even a slight variation in IR could cause deviations in fit results. Therefore, a more robust adaptive method is used to obtain IR_{ext} and obtain more consistent fits. IR_{ext} is used for all subsequent fits, for both FRETting and non-FRETting decay curves.

Theoretically, the decision to use GFP lifetime as an internal reference for single transfected cells is well justified as GFP exhibits a single exponential decay that is relatively insensitive to the cellular environment. For double transfected cells, the mean lifetime is used as a reference as it can be more robustly measured, compared to quantifying a double-exponential decay with noisy data. It also relies on the assumption that the cellular population studied is biochemically homogeneous within biological noise. Clearly, these assumptions cannot always be met in some studies and this approach needs to be used with caution.

3.4.2 Segmented and global fit

We examine the differences in lifetime fits observed between various fitting procedures, and also between global fitting results from summed curves and individual curves. All fitting algorithms use the model as represented by equation (1). For both GPax-only cells (8 cells) and GPax / FATmCh cells (5 cells), fits were carried out with i) a single-exponential decay, ii) a double-exponential decay with τ_D fixed at 2.6 ns and iii) both lifetimes freely varying. For each fitting procedure, results are compared between global fitting of individual decay curves carried out over the whole cell image (global-indiv) and global fitting of decay curves summed upon segmentation according to intensity thresholds (segment-sum), as previously described. LL1000 was chosen, which resulted in ~8000 decays fit for global-indiv and ~6 decays fit for segment-sum.

In order to verify the conclusions made from fitting of cell data, single- and double-exponential decay curves were simulated (5 sets of curves each). The single-exponential decay curves had a lifetime of 2.6 ns and the double-exponential decay curves had lifetimes of τ_D = 2.6 ns and τ_F = 1.3

ns. 2.6 ns was chosen as it is close to the non-FRETting lifetime of GFP, and a τ_D/τ_F ratio of 0.5 was chosen, giving τ_F = 1.3 ns. The same fitting procedure as above was carried out, with τ_D fixed at 2.6 ns for fit procedure (ii). Results are presented in Table 2.

		GPax / single-exponential decays					GPax – FATmCh / double-exponential decays				
		Segment-sum		Global-indiv			Segment-sum		Global-indiv		
		τ_D (ns)	τ_F (ns)	τ_D (ns)	τ_F (ns)	FR	τ_D (ns)	τ_F (ns)	τ_D (ns)	τ_F (ns)	FR
(i) Single-exponential fit	Cell data	2.58 ± 0.07		2.47 ± 0.04			2.37 ± 0.10		2.30 ± 0.19		
	Syn. data	2.60 ± 0.01		2.52 ± 0.00			2.15 ± 0.01		1.981 ± 0.00		
(ii) Double-exponential fit with τ_D fixed	Cell data	2.6	2.56 ± 0.06	2.6	2.05 ± 0.19	0.38 ± 0.25	2.6	2.34 ± 0.12	2.6	1.99 ± 0.05	0.51 ± 0.22
	Syn. data	2.6	2.58 ± 0.01	2.6	2.00 ± 0.01	0.26 ± 0.29	2.6	1.30 ± 0.02	2.6	1.28 ± 0.01	0.52 ± 0.30
(iii) Double-exponential fit	Cell data	2.59 ± 0.05	2.56 ± 0.04	2.76 ± 0.11	2.17 ± 0.08	0.49 ± 0.24	2.40 ± 0.10	2.33 ± 0.11	2.56 ± 0.13	1.99 ± 0.08	0.47 ± 0.24
	Syn. data	2.60 ± 0.00	2.59 ± 0.01	3.02 ± 0.08	2.08 ± 0.01	0.54 ± 0.26	2.58 ± 0.05	1.29 ± 0.04	2.58 ± 0.01	1.27 ± 0.01	0.51 ± 0.30

Table 2 Lifetime fit results for cell and synthetic data (syn. data) using various fitting procedures.

When cell data are fit with single-exponential decays, global-indiv and segment-sum extract similar τ_D for the two cell populations each, with segment-sum values being slightly higher. For GPax cells, segment-sum recovered a lifetime of 2.58 ± 0.07 ns while global-indiv recovered a lifetime of 2.47 ± 0.04 ns. Summing up multiple single-exponential decay curves produces another single-exponential decay curve with the same lifetime but higher photon count and less noise (higher SNR). For GPax / FATmCh cells, the value of τ_D is underestimated. When a double-exponential decay is force-fit with a single-exponential decay, an average lifetime of the actual two lifetimes present is recovered, 2.37 ± 0.10 ns from segment-sum and 2.30 ± 0.19 ns from global-indiv.

Results from simulated decay curves verified our conclusions. For single-exponential decays, segment-sum accurately extracted the lifetime whereas global-indiv extracted a lifetime within 5% of the known value of 2.6 ns. This shows that global-indiv single-exponential fitting on curves with a single lifetime is affected by the SNR of the decay curves, but that fit results are not greatly compromised. For double-exponential decays, both methods extracted lifetimes within 10% of the average of the two true lifetimes.

Fits were also carried out by fixing τ_D to 2.6 ns. GPax cells are not expected to have two lifetimes. Segment-sum indeed recovers a second lifetime of 2.56 ± 0.06 ns, similar to the fixed τ_D value, indicating that it is possible to recover the single decay lifetime even with a double-exponential fit from decay curves with very high SNR. Global-indiv is unable to recover the correct single lifetime due to the need for higher SNR data. It should be possible to recover the second lifetime present in GPax / FATmCh curves by fixing τ_D to the non-FRET lifetime value obtained from GPax cells. Fixing τ_D reduces the number of degrees of freedom given to the fitting algorithm, thus allowing the fits to converge faster. Segment-sum recovers a τ_F of 2.34 ± 0.12 ns while global-indiv recovered a lower τ_F of 1.99 ± 0.05

Results from simulated decay curves verified our conclusions for single-exponential decays. For double-exponential decays, both segment-sum and global-indiv are able to recover the correct τ_F, to within 2%, though the segment-sum value is slightly more accurate. Though summing up many double-exponential curves, each with its own fraction of the two lifetimes, averages over the pre-factors in the fit equation, due to the very high resulting SNR in the summed decay, segment-sum is still well-able to extract the known second lifetime. However, even though the extracted second lifetime obtained from segment-sum might be slightly more accurate, this method does not allow recovery of the pre-factors. Therefore, global-indiv is the desired method for most applications. That the difference in lifetimes obtained from the two methods is larger for cell data compared to synthetic data is an indication that experimental decay curves contain biological noise sources not accounted for when simulating decay curves only with Poisson noise.

When fits were carried out with both lifetimes free to vary, for GPax cells, segment-sum is again able to extract two lifetimes with similar values, 2.60 ± 0.05 ns and 2.56 ± 0.04 ns due to the high SNR. However global-indiv fails and in fact recovers two distinctly different lifetimes due to the low SNR. The recovered values, 2.76 ± 0.11 ns and 2.17 ± 0.08 ns, lie on either side of the single lifetime present, and average to 2.47ns, within 5% of 2.6ns. For GPax / FATmCh decays, segment-sum also fails to recover the two expected lifetimes most likely because of the compound effect of averaging over the pre-factors, and because the two lifetimes present in the decay curves are not well-separated. Global-indiv on the other hand successfully recovers lifetimes of τ_D = 2.56 ± 0.13 ns and τ_F = 1.99 ± 0.08 ns.

Results from simulated decay curves again verified experimental results for single-exponential decays. Segment-sum extracted two lifetimes within 1% of the known τ_D and global-indiv extracted two lifetimes well on either side of the known τ_D. This result shows that a false FRET detection can actually be deduced from single-exponential decays if these data are fit with double-exponential fits. It underscores the importance of exercising some discretion when applying mathematical methodology to known or expected biological phenomena. For double-exponential synthetic curves, both segment-sum and global-indiv are able to recover the two lifetimes present in the curves, within 5% error.

It is unclear which method is best to accurately determine recovered lifetimes when carrying out double-exponential fits on experimental cell data. Both lifetimes could be allowed to vary freely. However, fitted lifetimes may vary for images obtained in a single imaging session, as shown in Table 3. One way to overcome this uncertainty is to assume that τ_D is the same in both GPax-only and GPax / FATmCh cells. This assumption says that the lifetime of GPax in cells is the same

regardless of whether it is the sole fusion protein species within the cell, or whether it is co-expressed with a partner fusion protein. For cells of the same type, cultured, transfected, and imaged under the same conditions, this assumption is reasonable. By doing this, τ_D can be fixed when carrying out double-exponential fits, thus recovering only τ_F and FR. Using this method, a comparison of the values of τ_F can be made across all images.

GPax (single-exponential fit)	2.58 ± 0.04					
	Lifetimes free to vary			Fixed τ_D = 2.6 ns		
	τ_D (ns)	τ_F (ns)	FR	τ_D (ns)	τ_F (ns)	FR
GPax / FATmCh 1	2.58	2.01	0.46 ± 0.22	2.6	2.01	0.50 ± 0.24
GPax / FATmCh 2	2.44	1.93	0.49 ± 0.24	2.6	1.95	0.60 ± 0.21
GPax / FATmCh 3	2.45	1.94	0.41 ± 0.23	2.6	1.97	0.55 ± 0.20
GPax / FATmCh 4	2.48	1.92	0.48 ± 0.24	2.6	1.94	0.57 ± 0.21
GPax / FATmCh 5	2.65	2.07	0.48 ± 0.23	2.6	2.06	0.44 ± 0.24
Mean	2.52	1.97			1.99	
s.d.	0.01	0.07			0.05	

Table 3 Fit results for GPax and GPax / FATmCh cell data obtained during a single imaging session, with two fitting procedures: (i) Double exponential fit with lifetimes free to vary, (ii) Double exponential fit with τ_D fixed at 2.6 ns.

3.4.3 Applicability of global analysis to cell data

It is possible that different locations within the cell, delineated by varying fluorescence intensities, have microenvironments which differentially affect the fluorescent proteins' properties. This would result in varying lifetimes thus invalidating global analysis. Therefore, to test the validity of the global assumption on cell data, the double-exponential global analysis carried out on GPax-only cells as above was further analyzed. Specially, we segment the cell into regions of based on differences in intensity levels. Differences intensity level may correlate with lifetime distribution differences for a number of reasons. For example, the differences in intensity level may reflect different density of protein aggregation that may result in self-quenching and lower lifetime. As another example, the differences in intensity level may be a result of local protein conformation differences that results in lower GFP quantum yield and shorter lifetime. As can be seen from Figure 21 however, FR distributes similarly regardless of which intensity region is examined.

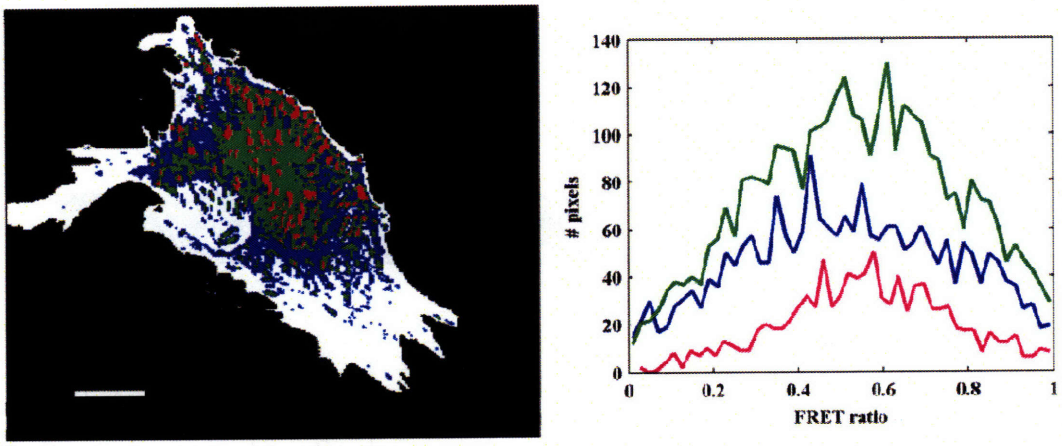

Figure 21 (a) GPax cell segmented by intensity at LL1000. (b) Histogram of FR distribution of cell in (a), color-coded by cell intensity segment. A double-exponential fit was carried out to obtain the FR. Scale bar is 10 μm.

As further validation of this, global analysis was carried out on pixels with similar intensities (and thus photon counts), but located at different regions in the cell, either FAs or cytosol. Since FAs, as sites of cell attachment to the basal surface, transmit force and recruit a distinct set of proteins, these regions are morphologically and biologically different than the cytosol. It would be expected that if variations in fluorescent protein properties exist within the cell, comparing fit results from these two regions would extract such differences. Single-exponential fits carried out on these pixels retrieved $\tau_D = 2.65 \pm 0.03$ ns for FA pixels, and $\tau_D = 2.65 \pm 0.04$ ns for cytosolic pixels. There is indeed no difference between these lifetimes, which demonstrates the applicability of global analysis to cell data. While this lack of intensity-dependent differences in lifetime distribution does not prove the validity of global analysis in all cases, it does justify the use of global analysis for our cell data. The approach that we have taken in testing the validity of global analysis is also useful in evaluating this data analysis method in other biological systems.

3.4.4 Photon counts per pixel – lifetime scaling

It has been reported that at least 100 counts per pixel is required in order to extract a lifetime with uncertainty of 20% from a fluorescence decay curve [60]. A lower limit of one thousand counts per pixel is required in order to accurately extract two lifetimes, provided the lifetimes are well separated and the two pre-factors are of comparable magnitude [60, 113]. In cell samples, these parameters cannot be predicted and depend entirely on the biological system. The binding interaction between fusion proteins will dictate the distance between FRETting fluorophores and thus τ_F. The expression rate of fusion proteins depends on the cell's transcription and translation machinery, and cannot be controlled externally. Thus the FRET ratio (pre-factors) distribution will vary at each pixel depending on the amount of fusion protein present. As we attempt to select cells that are not overexpressing fusion proteins, this limits the total photon counts that can be collected within each pixel, where it might be difficult to collect even 1000 counts per pixel for a two-lifetime fit. Moreover, our fusion proteins localize to FAs, leading to a difference in pixel intensity between FA and cytosolic regions. Whereas FAs might contain pixels with more than 1000 counts, cytosolic regions might not.

In order to overcome these limitations, we examined how the fitted lifetimes and FRs deviate with varying lower limits on photon counts for GPax / FATmCh cells. For GPax cells, this process is unnecessary as enough pixels per cell have higher than 1000 counts. Besides, segment-sum adequately recovers the true τ_D from single-exponential decay curves, as previously shown. For GPax / FATmCh cells, τ_D was fixed at 2.6ns, while τ_F and FR were recovered by carrying out fits at varying photon count lower limit (LL) values. The open circles in Figure 22(a) show the variation in fitted τ_F with LL, from two sets of cells. The fitted τ_F reaches a plateau at LL of around 1500. Fits carried out on synthetic curves with a τ_F / τ_D ratio of 0.8 and varying LL show similar trends (closed circles). Represented as percentage deviation from plateau value, it can be seen that the curves from both cells (open triangles) coincide, with the curve from synthetic data (closed triangles) following a similar trend. Inclusion of decay curves with lower LL into fits leads to systematic underestimation of the second lifetime present in the double-exponential decays. Since the deviation with LL is systematic, it should be possible to carry out fits at lower LL in order to include as many pixels as possible from cell data, including dimmer pixels, and scale up the values from fitted lifetimes to true values. In order to map out this systematic variation, fits were carried out on synthetic curves at varying LL and τ_F / τ_D ratios.

Trends in percentage deviation in fit τ_F with τ_F / τ_D ratio are shown in Figure 22(b), where the known τ_F is used when calculating τ_F / τ_D. Percentage deviation, for example between LL500 and LL2000, is defined as

$$\frac{\tau_{F(LL500)} - \tau_{F(LL2000)}}{\tau_{F(LL2000)}} * 100 \qquad 11$$

Hereinafter, it is written as 500%dev2000. Squares are percentage deviation from $\tau_{F(LL2000)}$ (500%dev2000 and 1000%dev2000), circles are percentage deviation from $\tau_{F(LL1000)}$ (500%dev1000), while triangles are percentage deviation from known τ_F (500%devτ_F, 1000%devτ_F, and 2000%devτ_F). Dotted lines are fits of LL500 %dev points, dashed lines are fits of LL1000 %dev points, while the solid line is a fit of LL2000 %dev points. The τ_F obtained from fits with LL2000 is very close to the true τ_F, within 10% for lifetime ratios between 0.02 and 0.82. However as previously mentioned, the lifetime is increasingly underestimated with higher τ_F / τ_D ratio. While initially LL1000 was the minimum criteria for obtaining 'good fits', Figure 22(b) shows that results obtained from LL1000 fits can in fact be scaled up to the true value. Thus Figure 22(b) provides the τ_F master curve from which the value of the true τ_F can be determined for fits at any LL. As an example, for cell data, fits can be carried out at any two LL values, LL500 to include most of the pixels within cells, and also at LL1000 to capture a smaller fraction of the pixels. The percentage deviation, 500%dev1000, can be calculated from the fitted τ_F obtained at these two LL values. Referring to the 500%dev1000 master curve, the true τ_F / τ_D ratio can be read from the x-axis. . The plot of 500%devτ_F serves as a cross-check, where the true τ_F value calculated from this line should be identical as the one calculated by the above method. True τ_F can be calculated since τ_D is known as the GPax lifetime value.

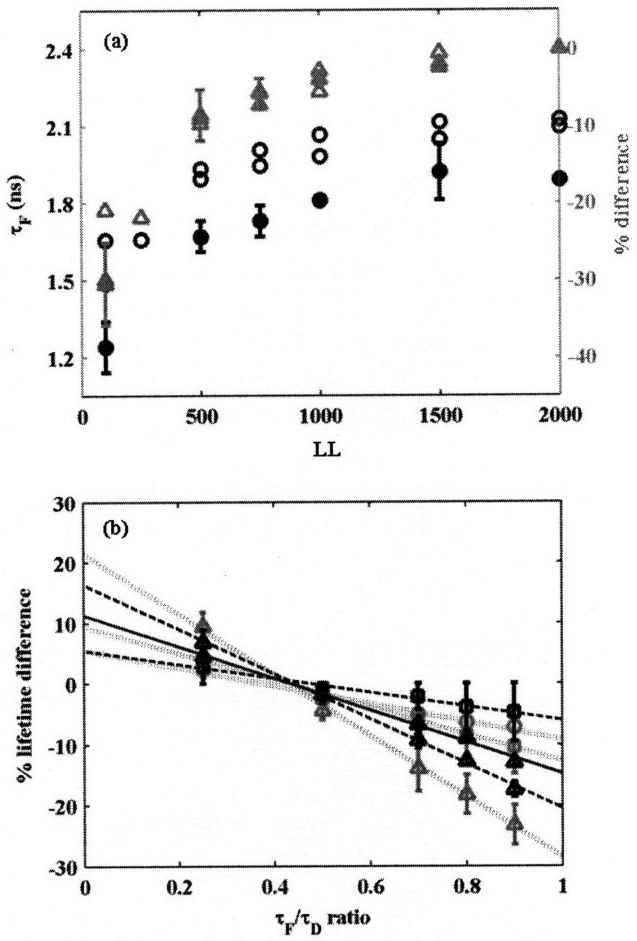

Figure 22 (a) Variation in fitted τ_F with varying LL. Double exponential fits were carried out with τ_D fixed at 2.6 ns for both cell and synthetic data. Left axis is fitted τ_F, right axis is percentage difference in fitted τ_F compared to fitted τ_F at LL2000. Open markers: cell data, closed markers: synthetic data. (b) Master curve for scaling τ_F fit to true τ_F. Squares are percentage deviation from τ_F (LL2000) (500%dev2000 and 1000%dev2000), circles are percentage deviation from τ_F (LL1000) (500%dev1000), triangles are percentage deviation from true τ_F (500%devτ_F, 1000%devτ_F, and 2000%devτ_F). Dotted lines are fits of LL500 %dev points, dashed lines are fits of LL1000 %dev points, solid line is a fit of LL2000 %dev points.

This plot corroborates Gratton's previous finding that a minimum of LL1000 is sufficient to extract τ_F within 20% of the true value. However, we can actually scale up the fitted lifetime to true τ_F, enabling us to calculate a more accurate value for FRET efficiency and thus interfluorophore distance, *r*. The ability to use pixel with lower photon counts further allows us to study regions where fluorescent protein expression is lower.

3.4.5 Photon counts per pixel – FRET ratio scaling

Though much effort has previously been put into analyzing the accuracy of fitted lifetime values obtained from FLIM data [60], not much work has been done to examine the variations in the

exponential pre-factors with various fitting protocols. Here we examine the effect of variations in τ_F / τ_D and LL on pre-factors, formulated as FR as previously described.

Fits were carried out at τ_F / τ_D = 0.8 and varying LL. A scaled histogram of the difference in fit compared to true FR (fitFR – trueFR) (fit-truFR) is shown in Figure 23(a). The histogram is similar for all LL values except for LL100. This is very likely because at LL100, the SNR is below the threshold for obtaining reasonable fit parameters. The histogram is not quite symmetrical about zero-deviation, but is skewed slightly towards negative deviation. A plot of true FR against fit FR at LL1000 (Figure 23(b)) shows the actual distribution of FR values. For comparison, a dashed line with zero y-intercept and slope of one is also plotted. A fit that produces results with a symmetrical histogram about zero deviation would produce a true FR vs fit FR plot with datapoints scattered about this line. The open circles show the position where the points are most dense (histogram peak). When a line of best fit is drawn through the circles, the parameters recovered are a y-intercept of -0.12 and slope of 1.5. If a cell data fit were carried out at LL1000 and the τ_F / τ_D ratio was found to be 0.8 by scaling from the τ_F master curve, the slope and y-intercept values would be used to shift fit FR values to true FR values. Figure 23(c) is a plot of slope and intercept for fits at τ_F / τ_D ratio of 0.8 and varying LL. It shows that the slope approaches one and the y-intercept approaches zero with higher LL. This is an obvious trend as decays with higher total counts have better SNR, leading to more accurate fits.

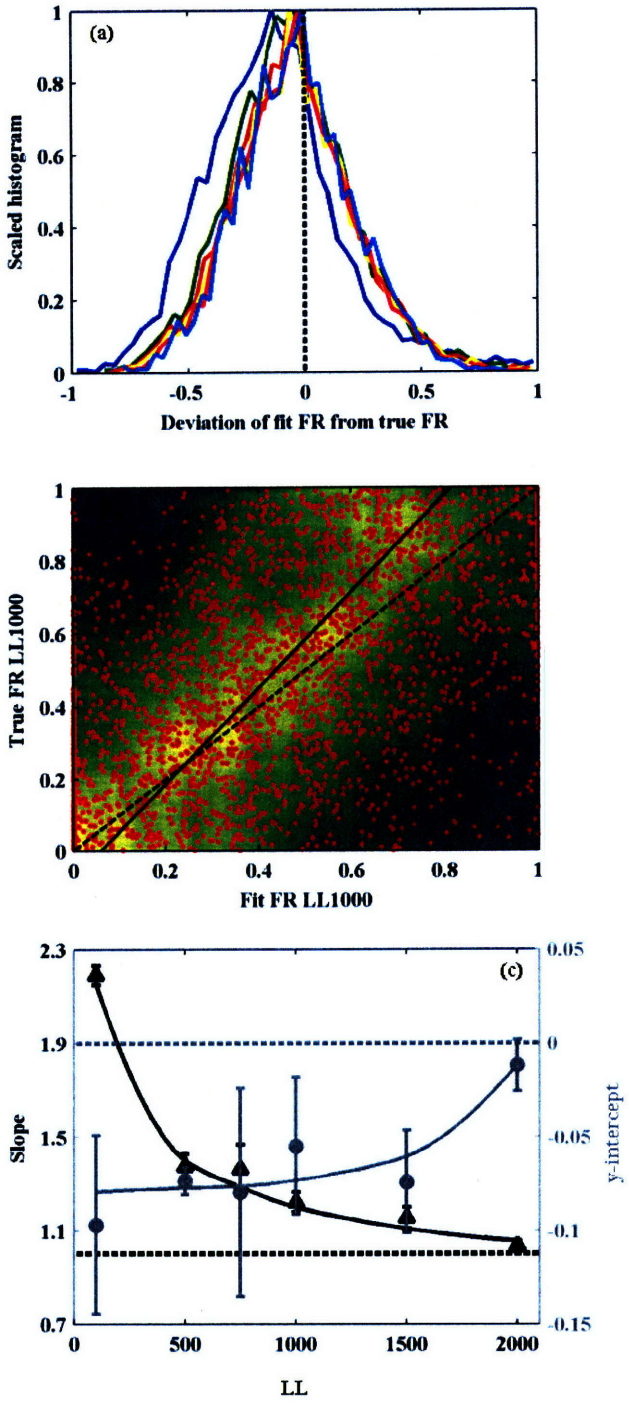

Figure 23 (a) Scaled histogram of fit-truFR at a τ_F / τ_D ratio of 0.8 and varying LL values. Color scheme is as follows: LL100, LL500, LL750, LL1000, LL1500, LL2000. (b) Plot of true FR vs. fit FR at a τ_F / τ_D ratio of 0.8 and LL1000. Red points: raw data. Plot is pseudo-colored by data density; yellow: high density of data, green: low density of data, with a gradation for intermediate values. Solid line: line of best fit through data, dashed line: line with zero y-intercept and slope of one. (c) Slope and intercept of true vs fit FR plots at a τ_F / τ_D ratio of 0.8, and with varying LL. A best-fit spline is drawn through the datapoints.

A scaled histogram of fit-truFR at LL1000, with varying τ_F / τ_D ratios, shows more pronounced differences between low lifetime ratios and higher lifetime ratios (Figure 24(a)). The histogram skews from more positive differences to more negative differences with increasing τ_F / τ_D ratio. Besides that, relatively more pixels show higher differences with increasing τ_F / τ_D ratio. We can again plot the variation in slope and y-intercept with varying ratios, and the plot shows that the slope approaches one and the y-intercept approaches zero as τ_F / τ_D decreases (Figure 24(b)). This suggests that FR can be extracted more accurately from FLIM data when the lifetimes are more widely separated. While this has been shown to be true for lifetimes, it has not previously been articulated in terms of FR.

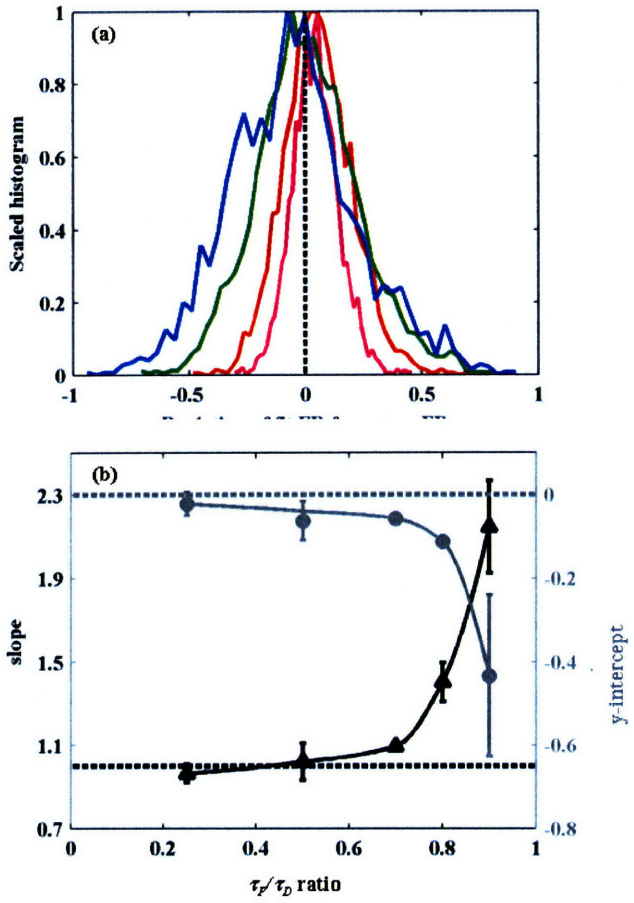

Figure 24 (a) Scaled histogram of fit-truFR at LL1000 and varying τ_F / τ_D ratio. Color scheme is as follows: τ_F / τ_D = 0.25, τ_F / τ_D = 0.5, τ_F / τ_D = 0.7, τ_F / τ_D = 0.8. (b) Slope and intercept of true vs fit FR plots at LL1000 and varying τ_F / τ_D ratio. A best-fit spline is drawn through the datapoints.

With each variation in lifetime ratio and LL, it is possible to deterministically calculate the variation in fit FR. Therefore, it is possible to scale parameters obtained from lower-intensity cell data (low LL) to true lifetime and FR, based on the slope and y-intercept values presented here. Conversely, it is possible to state the variance in true FR at any fit FR value.

3.5 Discussion

3.5.1 Systematic deviation in lifetime and FRET ratio

It is intriguing to see that when double-exponential decay curves are fit with the longer lifetime fixed, both the shorter lifetime and the FRET ratio are systematically underestimated when decays with lower photon counts are included in the fits. That is to say, for any given decay curve with high photon count, including decay curves with progressively lower photon counts in the fit shifts τ_F for the whole set of curves to lower values, and FR for that decay curve also falls (Table 4). This behavior can be attributed to the presence of a noise floor.

	Fix τ_D = 2.6 ns		Intersection of fit at LL2000 with fit at LLx		Lifetimes free to vary		
	τ_F (ns)	FR	x-axis: time (ns)	y-axis: # photons	τ_D (ns)	τ_F (ns)	FR
LL2000	1.90	0.885					
LL1500	1.86	0.845	5.994	44.118	2.75	1.88	0.893
LL1000	1.81	0.787	5.970	44.420			
LL750	1.77	0.747	5.951	44.673			
LL500	1.69	0.687	5.917	45.147			
LL100	1.25	0.474	5.654	48.969			

Table 4 Fit results for a single decay curve with high photon counts, when curves with increasingly lower LL values are included in the fit.

When decay curves have high photon counts (e.g. LL2000), the SNR is high and remains so until longer times, as shown by the solid black line in the schematic of Figure 25(a). The signal itself will be noisy with Poisson noise but this is not shown for clarity. When a fit of the decay is carried out with the longer lifetime fixed, the fit shorter lifetime and FR are close to the true values, with a slight difference due to the tail end of the decay curve reaching the noise floor. For decay curves with low photon counts (e.g. LL100), the SNR is low, and the low signal starts affecting the decay curve at shorter times (solid red line in Figure 25(b)). If both lifetimes were free to vary, τ_D would appear longer than the true value to compensate for the noise floor (dotted red line in the same figure). The shorter lifetime and FR are both underestimated (Table 4). However, because τ_D is fit to the true value, in order to compensate for the difference between fitted and true decay, the shorter lifetime and FRET ratio is underfit, as shown by the solid magenta line.

In order to verify this, we look at the intersection between fits obtained at LL2000 and those obtained at lower LL values, for the same decay curve of high photon counts (Figure 25(c)). The fit from LL2000 should intersect fits with lower LL at lower times and higher FR values (higher photon counts). This is indeed shown to be true, as is given by Table 4, thus verifying our reasoning.

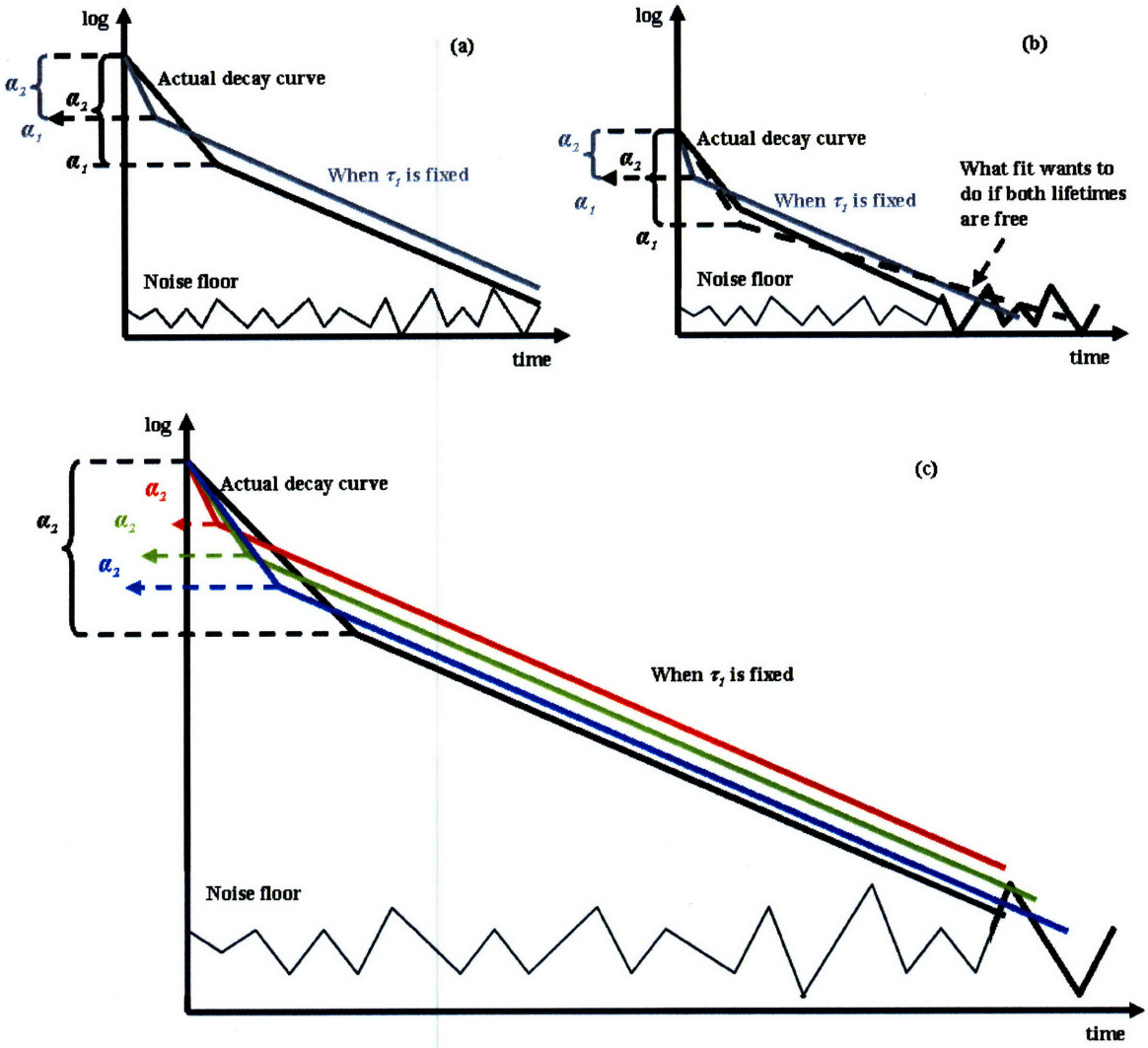

Figure 25 (a) Schematic of high photon counts curve and resulting fit. (b) Schematic of low photon counts curve and resulting fit. (c) Schematic of resulting fit when lower and lower counts curves are included in the fit.

3.5.2 Methodology for fitting cell lifetime data

Based on results presented, the fitting protocol followed for a particular imaging session is thus:

i. Carry out single-exponential decay fits on GPax cells

ii. Calculate the mean of fitted τ_D's and use this value as the fixed τ_D when carrying out double-exponential decay fits on GPax / FATmCh cells

iii. Recover τ_F and FR distributions from fits on GPax / FATmCh cells at different LLs

iv. Scale τ_F and FR from fit to true values, using master curves

Single-exponential decay fits were carried out on six GPax cells' decay curves. The single lifetime extracted was 2.68 ± 0.07 ns. Thus a τ_D of 2.7ns was used as the fixed value when carrying out double-exponential decay fits on six GPax / FATmCh cells' decay curves. Double-exponential decay fits were carried out at LL500, LL1000, and LL2000, for comparison. Percentage deviations 500%dev1000, 500%dev2000, and 1000%dev2000 were calculated. Based on the FR master curve, these %dev's corresponds to a ratio of true τ_F / τ_D of 0.83 ± 0.07. The true τ_F is thus calculated to be 2.24 ± 0.08 ns. This lifetime value can be cross-checked by using the %devτ_F master curves. From this, a lifetime value of 2.37 ± 0.16 ns is obtained, giving an accuracy of 6% to our τ_F estimate. From these calculations, the FRET efficiency of GPax and FATmCh in our intracellular system is 17%, translating to an inter-fluorophore distance of 61.3 Å.

The fit FR was scaled using slope and intercept values of 1.715 and -0.174 respectively. These were obtained from a fit vs. true FR plot at τ_F / τ_D = 0.85 and LL1000 (data not shown). The result of scaling FR is shown in Figure 26. Figure 26(a) is an intensity image of a GPax / FATmCh cell. Figure 26(b) shows the same cell pseudo-colored by the fit FR, and Figure 26(c) shows the cell pseudo-colored by the scaled FR. A histogram of fit FR and scaled FR shows the redistribution of FR upon scaling (Figure 26(d)). Thus from our scaling methodology, we are able to carry out fits on cell data with lower intensities and scale the resulting lifetime and FR to true values, based on a set of master curves.

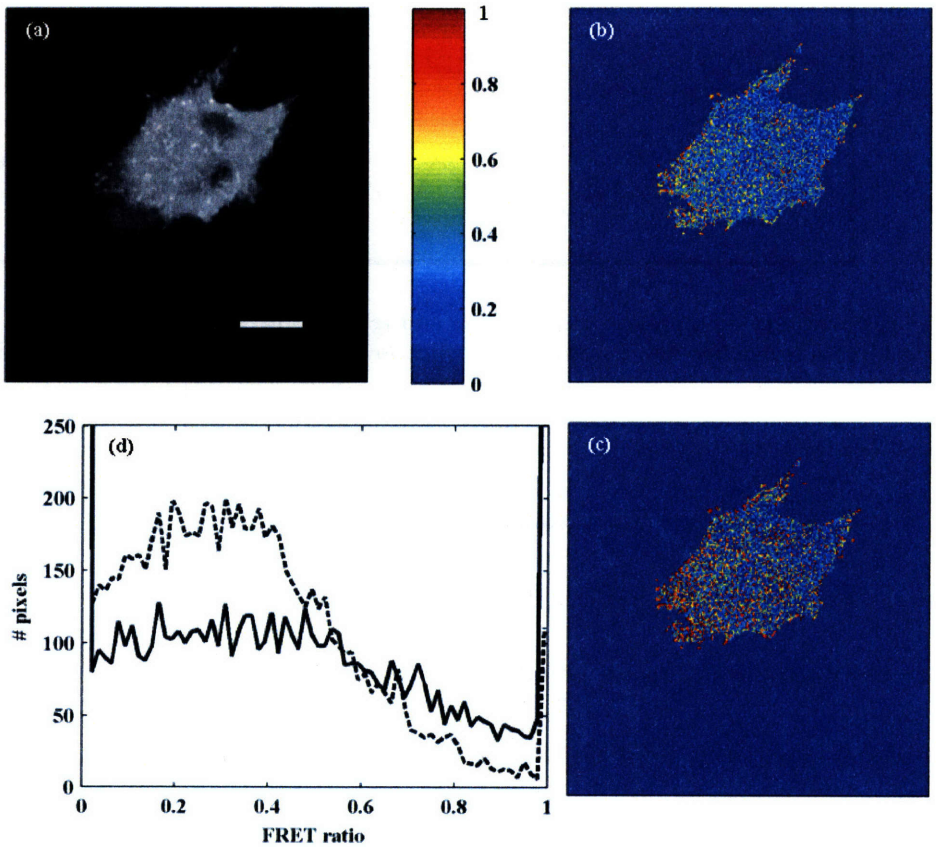

Figure 26 (a) Intensity image of GPax / FATmCh cell (b) Cell image pseudo-colored by fit FRET ratio (c) Cell image pseudo-colored by scaled FRET ratio (d) Histogram of FRET ratio. Dotted line: fit FR, solid line: scaled FR. Scale bar is 10 μm.

3.6 Conclusions

For our model system of interacting GPax and FATmCh proteins within BAECs, it has been shown that when the IR varies throughout the imaging session, it is not possible to use an IR measured at the start of the session in order to fit data from the whole session. An adaptive method is instead used to directly extract an IR from the experimental TCSPC data.

By systematically tracking the variation in lifetime and FR when the known τ_D is fixed for double-exponential decay fits on synthetic curves, we are able to generate lifetime and FR master curves. This allows cell data with low photon counts to be included in the fitting procedure. The resulting fit parameters (lifetime and FR) can be scaled to true values using the master curves. This overcomes the need to carry out fits only with high photon counts, as has been previously shown by other groups, and allows us to obtain more information from dim regions of the cell that would previously have had to be neglected.

By assuming that the GPax lifetime in cells is the same regardless of whether another fluorophore is present, a step-by-step method can be used to obtain FRETting lifetimes from double-transfected cells. Fits of decay curves from GPax-only cells provide this lifetime, which is then fixed for analysis of double-exponential curves from GPax / FATmCh cells. Results are then scaled using the previously mentioned master curves. This methodical process is important in order to make conclusions from real experimental cell data, where photon counts cannot be externally controlled and are necessarily low.

Chapter 4 Calculating Intracellular Free Energy (ΔG)

4.1 Introduction

Cellular processes such as proliferation, differentiation, and migration are regulated in large part by biochemical signals transduced through protein-protein interaction. In order to study these processes, assays have been developed that attempt to quantify the complex signaling network involved. To detect protein assemblages that originate intracellularly, well-established *in vitro* assays including co-immunoprecipitation and a common variation, pull-down assays, were developed [58, 104]. While these methods lead to detection of protein associations, their application to understanding dynamic cellular processes is constrained by the lack of quantification and especially so by the need for sample fixation. In order to increase quantification of protein interaction, assays that measure protein binding constants are available, including isothermal titration calorimetry (ITC) [83, 151, 152], nuclear magnetic resonance (NMR) [46] and surface plasmon resonance (SPR) [47, 67, 120]. Fluorescence cross-correlation spectroscopy (FCCS) has also been used to characterize protein binding in *in vitro* systems [76, 119, 143]. While these techniques have been successfully applied to purified proteins, they do not lend themselves to the interrogation of *in vivo* interactions. Clearly, a quantitative assay that is applicable to a dynamic intracellular system would be more useful.

The ability to tag and track proteins intracellularly means that questions pertaining protein interaction can now be probed [2, 27, 132]. Extending the ability of FCS to the intracellular environment, Kim et. al. are able to measure binding constants between calmodulin (CaM) and Ca2+ / CaM-dependent protein kinase II (CaMKII) under various conditions, in what is probably the first and only paper that reports an intracellular binding constant [78]. Their method utilizes two-photon cross-correlation spectroscopy (TPCCS). There are several other efforts to measure intracellular association / dissociation constants related to protein pairs of interest though these have not yet been published [Wohland T., National University of Singapore]. We would also like to attack this question by combining the utility of FRET / FLIM and FCS.

FRET / FLIM is increasingly used to answer questions related to binding of intracellular proteins [145, 157]. Peter et. al demonstrated a novel receptor-kinase interaction between the chemokine receptor (CXCR4) and protein kinase C (PKC)α in carcinoma cells using an EGFP-mRFP1 FRET pair [115]. A GFP-Cy3 FRET pair used by Parsons et. al detected activated Cdc42 interacting with PAK1 in a location-dependent manner [111]. Due to the small working distance over which FRET is relevant, a positive FRET readout detected through changes in donor fluorescence lifetime most likely denotes direct protein interaction. However, almost all literature related to FRET / FLIM halts at the determination of average lifetimes or calculation of interfluorophore distance. It is important to realize the usefulness of the other pieces of information available from FLIM data, which are the exponential pre-factors. From these, we can obtain ratios of bound to free donor fusion proteins. Combining this information with intensity-concentration measurements available through intracellular FCS measurements, a complete set of measurements allow us to calculate a map of free energy of binding for our protein pair of interest within cells.

4.2 Theory

In the cellular system where binding between GPax and FATmCh is being monitored, the binding reaction is written as $GPax + FATmCh \leftrightarrow GPax - FATmCh$. Assuming thermodynamic equilibrium, dissociation constant, K_d, is therefore given by the following equation, where C denotes concentration.

$$K_d(x,y) = \frac{C_{cell}^{GPax}(x,y) * C_{cell}^{FATmCh}(x,y)}{C_{cell}^{GPax-FATmCh}(x,y)} \quad 12$$

In order to calculate a K_d value for this reaction, it is necessary to measure concentrations, or ratios of concentrations, of free and bound fluorescent species.

As introduced in Chapter 1, eqn. 4 presents the per-pixel fluorescence intensity decay measured by FLIM, where pre-exponential factors α_D and α_F reflect fractional contributions to the total fluorescence from the FRETting and non-FRETting donor species respectively.

$$\frac{\alpha_F}{\alpha_D + \alpha_F} = \frac{I_F}{I_D + I_F} = \frac{C_{cell}^{GPax-FATmCh}}{C_{cell}^{GPax} + C_{cell}^{GPax-FATmCh}} = FR \quad 13$$

I_F and I_D are fluorescent intensities of FRETting and non-FRETting donor species, the ratio of which directly relates to the ratio of concentrations of bound and free GPax within the pixel. This equation can be rearranged to obtain an expression for the ratio $C_{cell}^{GPax} / C_{cell}^{GPax\text{-}FATmCh}$.

$$1 + \frac{C_{cell}^{GPax}}{C_{cell}^{GPax-FATmCh}} = \frac{1}{FR} \quad 14$$

$$\frac{C_{cell}^{GPax}}{C_{cell}^{GPax-FATmCh}} = \frac{1}{FR} - 1 \quad 15$$

The concentration ratio as obtained in eqn. 15 can be substituted into eqn. 12, resulting in the following expression:

$$K_d(x,y) = C_{cell}^{FATmCh}(x,y) * \left(\frac{1}{FR(x,y)} - 1\right) \quad 16$$

It is not a straightforward process, however, to measure the concentration of free FATmCh in a double-transfected cell. FCS measurements carried out directly on these cells would contain contributions from both GPax and FATmCh. It would be difficult to separate the contributions from each species, as well as contributions from the bound complex. We therefore carry out FCS separately on cells singly-transfected with either plasmid. An intensity image of the region where FCS is carried out is also taken. This gives us intensity (I) – concentration (C) calibration values from which it would be possible to calculate the concentration of fluorescent proteins in other transfected cells.

$$C^i_{cell}(x,y) = \frac{\langle I^i(x,y)\rangle_{cell}}{\langle I^i\rangle_{calib}} * \frac{F^i_{cell}}{F^i_{calib}} * C^i_{calib} \quad (17)$$

In this equation, i can be either red (R) or green (G) fusion proteins, making no distinction between free and bound species. F is the image scan rate.

When taking intensity images of double-transfected cells, fluorescent intensities in the green channel arise from both free and bound GPax (from and to FATmCh), with the contribution from bound GPax reduced by the FRET efficiency, E. When converting from intensity to concentration of green species, it follows that the concentration of both free and bound GPax is included. Intensities in the red channel contain contributions from both free and bound FATmCh, as well as some bleed-through, β, from the green channel. Therefore converting from red channel intensity to red species concentration requires subtraction of this bleed-through.

Green channel intensity, $$I^G_{ch}(x,y) = I^{GPax}_{cell}(x,y) + (1-E)I^{GPax-FATmCh}_{cell}(x,y) = I^G_{cell}(x,y) \quad (18)$$

Green species concentration, $$C^{GPax}_{cell}(x,y) + (1-E)C^{GPax-FATmCh}_{cell}(x,y) = C^G_{cell}(x,y) \quad (19)$$

Red channel intensity, $$I^R_{ch}(x,y) = I^{FATmCh}_{cell}(x,y) + I^{GPax-FATmCh}_{cell}(x,y) + \frac{I^G_{cell}(x,y)}{\beta} \quad (20)$$

Red species intensity, $$I^R_{cell}(x,y) = I^{FATmCh}_{cell}(x,y) + I^{GPax-FATmCh}_{cell}(x,y) = I^R_{ch}(x,y) - \frac{I^G_{cell}(x,y)}{\beta} \quad (21)$$

Red species concentration, $$C^{FATmCh}_{cell}(x,y) + C^{GPax-FATmCh}_{cell}(x,y) = C^R_{cell}(x,y) \quad (22)$$

From eqn. 15 and 19, $$C^{GPax-FATmCh}_{cell}(x,y) = \frac{C^G_{cell}(x,y)}{(\frac{1}{FR(x,y)} - E)} \quad (23)$$

Combining this with eqn. 22, we obtain $$C^{FATmCh}_{cell}(x,y) = C^R_{cell}(x,y) - \frac{C^G_{cell}(x,y)}{(\frac{1}{FR(x,y)} - E)} \quad (24)$$

A final substitution in eqn. 16 gives us K_d.

$$K_d(x,y) = (\frac{1}{FR(x,y)} - 1) * (C^R_{cell}(x,y) - \frac{C^G_{cell}(x,y)}{(\frac{1}{FR(x,y)} - E)}) \quad (25)$$

Using this methodology which combines FLIM and intensity-concentration scaling, K_d values can therefore be calculated for entire cells. A conversion to the Gibbs free energy of binding naturally

falls out as $\Delta G = RT \ln K_d$. R is the universal gas constant, 8.314 $JK^{-1}mol^{-1}$, and T is the temperature of the system, 300K.

4.3 Materials and methods

4.3.1 Cell preparation

Bovine aortic endothelial cells (BAECs) were cultured in Dulbecco's Modified Eagle Medium (DMEM) (Gibco, Invitrogen, Carlsbad, CA) supplemented with 10% fetal bovine serum,1% penicillin/streptomycin, and 1% L-glutamine. Cells were seeded at an initial density of 160,000 cells/well in fibronectin-coated 35mm glass-bottom (#1.5) dishes (MatTek Corporation, Ashland, MA). Transfection was carried out at ~80% confluence with either or both GFP-Paxillin (GPax), FAT-mCherry (FATmCh) plasmids, using the FuGene6 transfection reagent from Roche Diagnostics (Indianapolis, IN) and manufacturer's transfection protocols. Note that plasmid notation indicates position of fluorophore within the fusion protein, whereby GFP is at the N-terminus of Paxillin and mCherry is at the C-terminus of FAT. Just before imaging, cells were washed with PBS and DMEM supplemented with 10% fetal bovine serum,1% penicillin/streptomycin, and 1% L-glutamine but with no phenol red was replaced in the wells. Lifetime imaging was carried out 24 hours after transfection.

4.3.2 Plasmids

GPax plasmids were obtained as a gift from K. Yamada of the NIH, Bethesda, MD. Mouse FAT from the dsRed-FAT plasmid (N. Mochizuki, National Cardiovascular Center Research Institute, Japan) was amplified by PCR with primer pairs (5-CTAAGCAACCTGTCCAGCATCAGC3-) and (5-CGGATCCGGGTGTGGCCGTGTCTGCCCTAGC3-). The resulting PCR fragment was ligated into pcDNA4/HisMax© TOPO® vector (Invitrogen, Carlsbad, CA). mCherry from the pRSET-B mCherry plasmid (R. Tsien, UCSD) was digested with EcoRI and BamHI and ligated into the pcDNA4-FAT vector at the 3' end of FAT. The FAT-mCherry plasmid was amplified using the Qiagen MaxiPrep kit (Qiagen, Valencia, CA).

4.3.3 Instrumentation

The custom-built two-photon microscope setup shown in Figure 19 (So, 2001) is based on a modified inverted microscope, Axiovert 110 by Zeiss (Göttingen, Germany), with a femtosecond laser source from the Mira family of modelocked Ti:Sapphire oscillators by Coherent (Santa Clara, CA) (Pelet 2004; Pelet 2006). The laser excites a subfemtoliter volume at the focal point of a 40X Fluar objective (1.3NA, Zeiss).

For lifetime imaging (setup described elsewhere: So 2001; Pelet 2004; Pelet 2006), the laser is tuned at 890nm with 40mW power before the objective, resulting in low power at the sample so as to minimize photobleaching and cell damage. In order to minimize contributions from scattered laser light and autofluorescence, the cell's fluorescence signal is selected with a short-pass Schott BG-39 filter and short-pass 700nm filter from Chroma (Rockingham, VT). The signal is sent to the top port of the microscope where it is filtered for green wavelengths with HQ500LP from Chroma (Rockingham, VT). A photomultiplier tube (PMT), R7400P from Hamamatsu (Bridgewater, NJ),

detects emitted photons and this signal is sent to a time-correlated single photon counting card (TCSPC card), SPC-730 from Becker-Hickl (Berlin, Germany).

For FCS, a PMT with higher photon detection efficiency, H7421 from Hamamatsu (Bridgewater, NJ) is used in the bottom port of the microscope and is combined with single photon counting electronics. The laser is tuned either at 890nm (40mW before the objective) or 780nm (20mW before the objective). Power is low for minimized photobleaching throughout imaging. Green wavelengths from the cell are selected with BG-39 and SP700 filters (Chroma, Rockingham, VT) while red wavelengths are selected with two SP700 and a BP590-35 filters (Chroma, Rockingham, VT).

4.3.4 Imaging procedure

In order to obtain intensity-concentration values, intracellular FCS was carried out on cells transfected with either GPax or FATmCh. Intensity images of the same cells were also taken. FCS calibration factors, effective volume (V_{eff}) and $(r_0/z_0)^2$, were obtained using an aqueous solution containing 10nM Alexa Fluor 488 (Molecular Probes, Eugene, OR) imaged in 8-chamber Lab-Tek®II #1.5 coverglass slides (Thermo Fisher Scientific, Waltham, MA).

Double-transfected cells with fluorescent intensities in the middle range as observed using a 432 nm diode laser (Laserglow Technologies, Ontario, Canada) were selected for complete sets of intensity-FLIM imaging. We attempt to select for cells that are not over-expressing fusion proteins at too high a level but that are bright enough such that lifetime decay curves will have sufficient photon counts and acceptable signal-to-noise ratio (SNR). Selected cells typically have fluorescent protein concentrations in the nM to μM range.

4.3.5 Data analysis

FLIM data were analyzed using the global analysis algorithm as presented in Chapter 3. From GPax transfected cells, the non-FRETting lifetime, τ_D, of GFP is obtained using a single-exponential fit to lifetime decays. This value is fixed when analyzing double-transfected cells. Resulting double-exponential fits retrieve the FRETting lifetime, τ_D, from which efficiency of energy transfer, E, can be calculated as shown in eqn. 5, as well as per-pixel FRs. A lower photon count limit of LL500 was used when selecting pixels for which to fit decay curves. FR scaling was carried out accordingly, based on the method presented in Chapter 3.

FCS autocorrelation curves were analyzed with MATLAB (The MathWorks, Natick, MA) using the *lsqnonlin* nonlinear least-squares curve fitting function.

A mean filter with a 5 x 5 kernel was used. While having the effect of reducing the effect of noise on resulting calculations, this step also results in loss of resolution (blurring) especially at image edges.

4.4 Results and discussion

4.4.1 FCS intensity-concentration calibration

For GPax cells, FCS was carried out on 5 different cells, totaling 26 repeated measurements, while for FATmCh cells, FCS was carried out on three different cells, totaling 38 repeated measurements. Representative autocorrelation curves and the resultant fit from each cell set are presented in Figure 27. The GPax autocorrelation curves were fit with a single component fit, while the FATmCh curves were fit with a single component plus a constant term fit. In Chapter 1, G(0) is defined in eqn. 8 as the normalized autocorrelation value at zero time lag, and the following paragraph shows how it is inversely proportional to concentration. As can be seen from Figure 27, G(0) values are similar, thus signifying similar intracellular protein concentrations in both these cells. mCherry is a dim fluorophore compared to GFP [129, 130], and is stringently filtered in our setup by the BP590-35 filter to remove autofluorescence signals, thus resulting in a noisier autocorrelation curve. These points are also reflected in the intensity-concentration values calculated as following: I^{G}_{calib} = 4.45 ± 0.64, C^{G}_{calib} = 24.22 ± 6.00 nM, I^{R}_{calib} = 0.35 ± 0.10, C^{R}_{calib} = 30.03 ± 17.45 nM, $F^{G,R}_{calib}$ = 25khz.

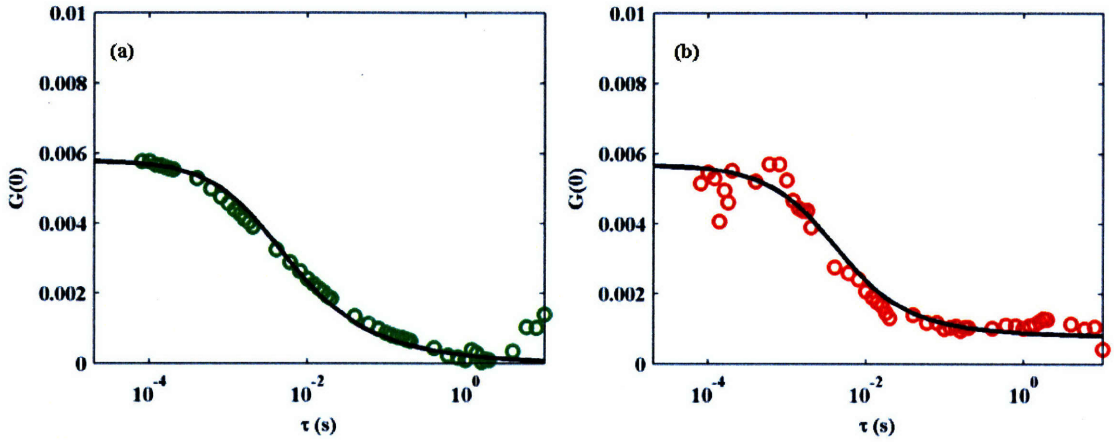

Figure 27 Representative FCS curves and resultant fit from (a) GPax or (b) FATmCh only cells.

4.4.2 Single cell calculation of ΔG

A representative dataset from a single cell measurement is shown in Figure 28. Figure 28(a) and (b) show the concentration (nM) of red and green species within the cell while Figure 28(c) shows the cell pseudo-colored by FR distribution. Global analysis on FLIM data extracted fitted lifetimes of τ_D = 2.60 ns and τ_F = 1.94 ns. The resultant true τ_F / τ_D ratio of 0.8 gives a FRET efficiency, E, of 0.2 and an interfluorophore distance of 56Å. Figure 28(d) shows the resultant cell map once ΔG has been calculated. Averaging over the whole cell, ΔG = -38.22 ± 5.14 kJ/mol.

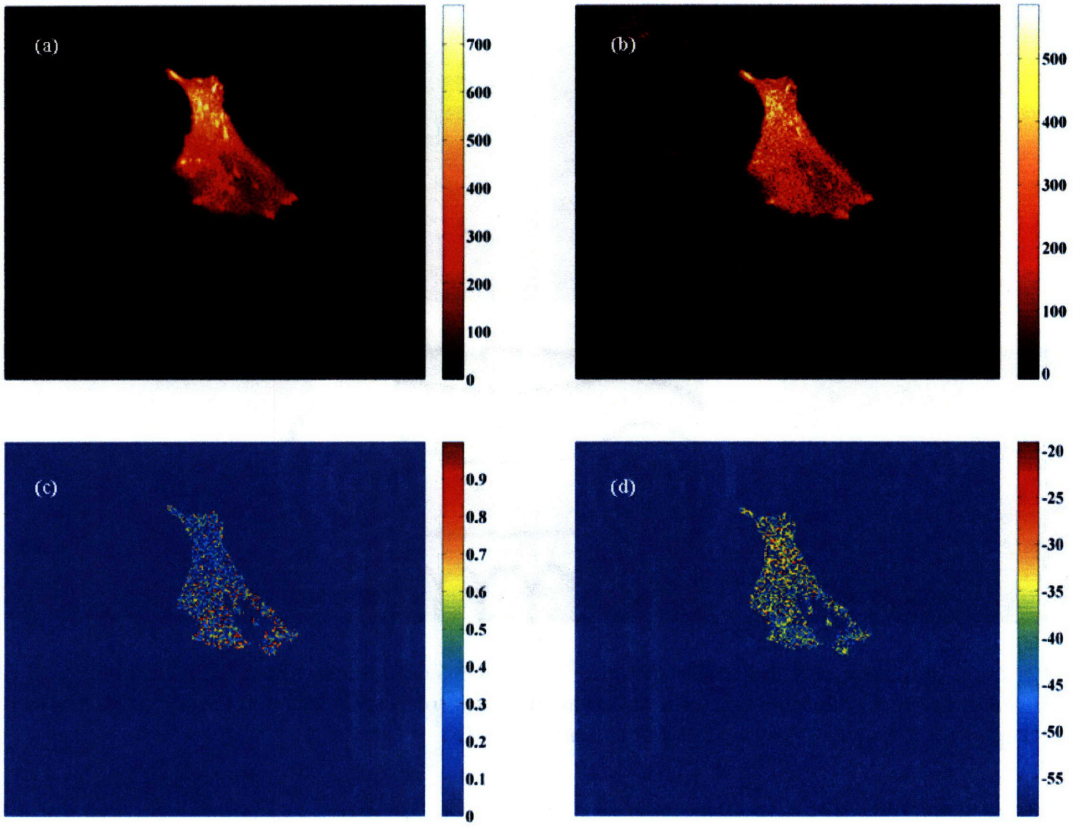

Figure 28 Sample measurement and resulting calculation for one dataset. (a) Concentration (nM) of green species, C^{G}_{cell} (b) Concentration (nM) of red species, C^{R}_{cell} (c) Cell pseudo-colored by FRET ratio. (d) Resulting map of calculated ΔG.

4.4.3 Effect of FRET ratio scaling and mean filtering

In order to calculate more accurate ΔG values, FR is scaled according to the scaling master curve presented in Chapter 3, and mean filtered. Figure 29 demonstrates the results of scaling and filtering with a 5 x 5 kernel on the same cell dataset as shown in Figure 28. Figure 29 (a) shows the cell pseudo-colored by scaled FR distribution and Figure 29 (b) shows the result of mean filtering on FR. Scaling of FR redistributes FR values within each pixel with maximum and minimum preserved at one and zero respectively while mean filtering reduces the range of FR values to middle range of the scale, as expected. Figure 29(c) and (d) show the mean filtered concentration (nM) of red and green species within the cell. As can be seen, mean filtering softens the image and results in blurring of edges. The resultant map of calculated ΔG is shown in Figure 29(e). Averaging over the whole cell, ΔG = -41.08 ± 2.82 kJ/mol.

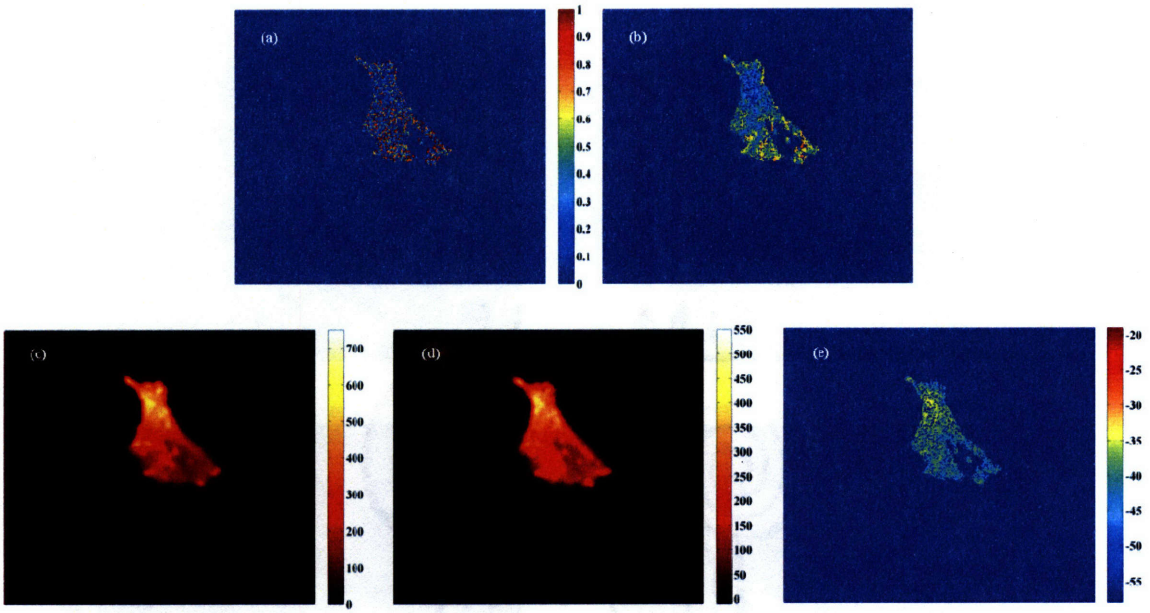

Figure 29 Effects of scaling FR and mean filtering (a) Cell pseudo-colored by FRET ratio (b) Cell pseudo-colored by mean filtered scaled FRET ratio (c) Concentration (nM) of green species, C^{G}_{cell} (d) Concentration (nM) of red species, C^{R}_{cell} (d) Resulting map of calculated ΔG.

With increasing kernel size, ΔG and variance decrease to a plateau. A kernel size of 5 x 5 strikes a balance between increasing loss of resolution and decreasing noise. This is shown in Figure 30(a), which tracks the effect of increasing kernel size on the distribution of ΔG. Number of neighbors in the plot refers to the number of surrounding rows of pixels that are averaged over, whereby neighbor number of 2 corresponds to a 5 x 5 kernel size. The effect on ΔG of FR scaling and filtering is further demonstrated in Figure 30(b) where values presented in the plot are normalized by the maximum values within each column. FR values are arranged in increasing value in column 1 of Figure 30(b). As a result of FR scaling, low FR values are reassigned as zero, high FR values are reassigned as one, and intermediate values are redistributed as per Figure 23(b) (column 2). Mean filtering averages out FR values (columns 3 and 4). Due to FR scaling, pixels reassigned FR values of zero or one lead to ΔG values of $\pm\infty$ (here reduced to normalized values of zero or one; column 6). Mean filtering once again results in averaging out of ΔG values (columns 7 and 8). A histogram of the various methods for calculating ΔG is given in Figure 30(c), where it can be seen that the number of pixels captured in the final ΔG calculation increases with mean filtering due to reduced noise, and the deviation from mean also decreases. The more accurate method for calculating ΔG would therefore be to scale FR and apply mean filtering to FR as well as measured intensity values.

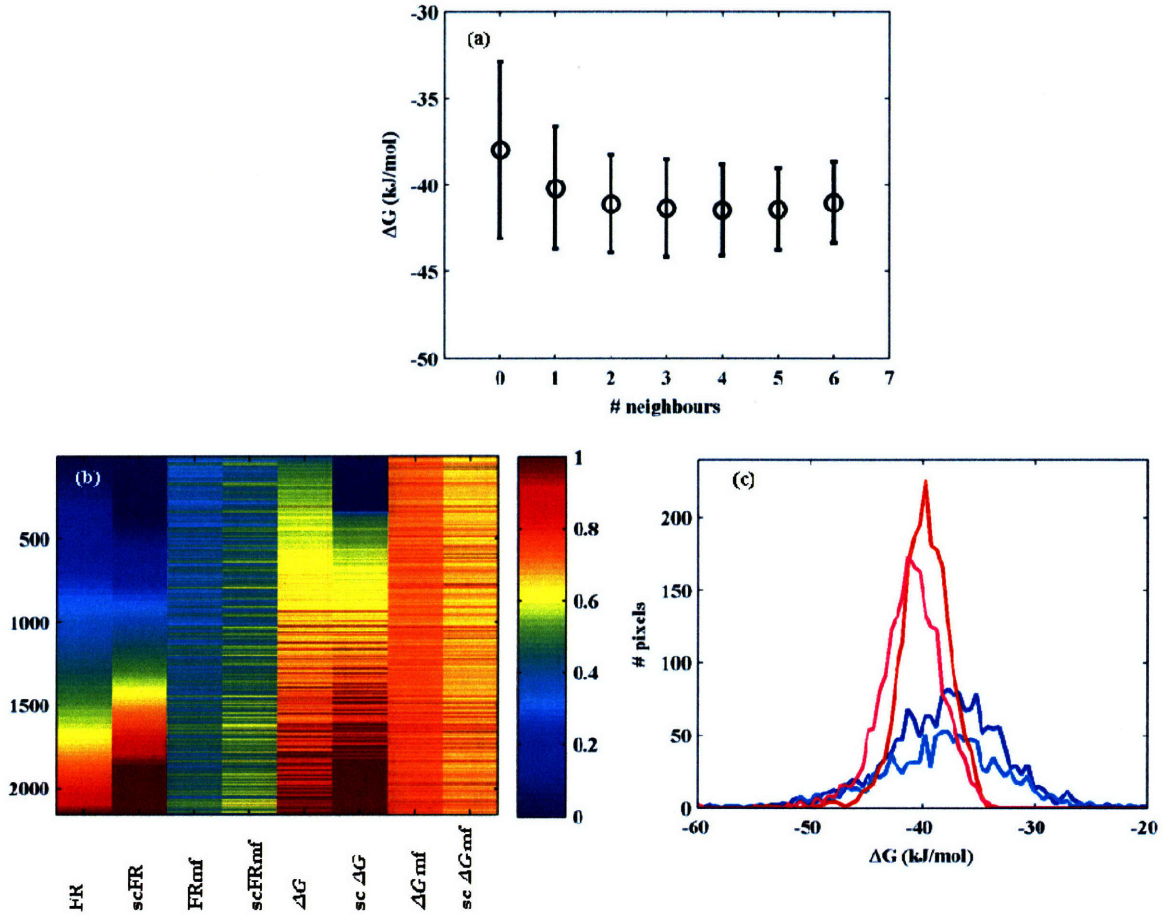

Figure 30 Effects of FR scaling and mean filtering on calculated ΔG values. (a) Plot of ΔG vs kernel size. A neighbor number of two corresponds to a 5 x 5 kernel. Error bars indicate standard deviation. (b) Evolution of pixels, sorted by increasing FR (column 1), with applied FR scaling and mean filtering; sc: FR scaling, mf: mean filtering. (c) Histogram of ΔG values with FR scaling and mean filtering. ΔG, scΔG, ΔGmf, scΔGmf.

4.4.4 Sensitivity analysis

In an ideal system, FCS intensity-concentration calibration measurements would give an exact intensity value for each measured concentration, resulting in an exact scaling value between intensities that matched the concentration scaling values. Consider two sets of intensity-concentration calibration values: $I_A - C_A$ and $I_B - C_B$. Ideally, $\frac{I_A}{I_B} = \frac{C_A}{C_B} = \beta$. However due to noise, $\frac{I_A}{I_B} = \alpha$ and $\frac{C_A}{C_B} = \gamma$ where $\alpha \neq \gamma$. This is what gives rise to the standard deviations presented in Section 4.4.1. One way to carry out sensitivity analysis on these calibration results is therefore to vary the intensity values that correspond to the mean calibration concentration values, in order to determine the effect of this variation in intensity-concentration calibration values on calculated ΔG. Results are shown in Figure 31 where ΔG values were calculated for various combinations of high and low intensity values as defined by the standard deviation given in section 4.4.1. In other words,

we are looking here at the effect of measurement noise on calculated ΔG values. In the figure legend, R denotes red species and G denotes green species. High limits correspond to the intensity mean plus standard deviation, while low limits correspond to the intensity mean minus standard deviation. From the figure, it can be seen that differences in mean ΔG values between calculations carried out with extreme limits of intensity variations compared to calculations carried out with the mean intensity calibration values are on the order of 5%. This indicates that using mean intensity-concentration calibration values is sufficient to calculate ΔG values.

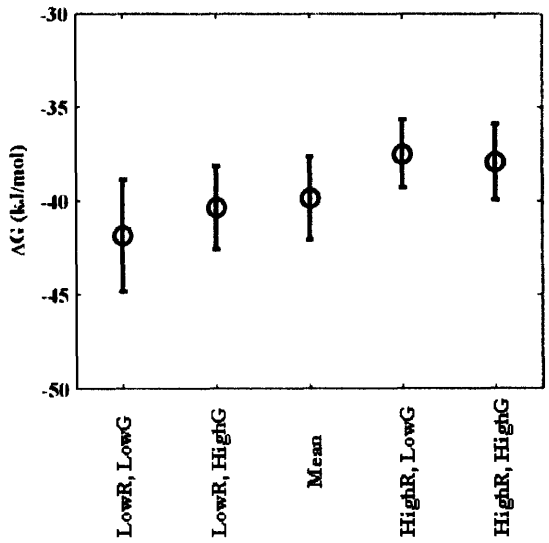

Figure 31 Sensitivity analysis of calculated ΔG values based on variances in intensity-concentration calibration values. Error bars indicate standard deviation.

4.4.5 ΔG across multiple cells

Previously measured K_d values for the FAT-LD interaction *in vitro* have been published. Gao et. al measured a K_d of $\approx$ 10 μM for the interaction between a synthetic LD peptide and the FAT domain by ITC [51]. Thomas et. al measured a K_d of $\approx$ 4 μM for a similar interaction, though using the SPR technique. More interestingly, when both LD2 and LD4 are present in the protein construct, the interaction between this construct and FAT is much tighter, resulting in a measured K_d of 300 – 600 nM [142]. This increase in binding affinity with the presence of both LD domains points to an allosteric effect in protein binding. While the presence of one LD domain can result in binding between FAT and this domain, the presence of both LD domains here strengthens the binding roughly ten-fold, indicating positive cooperativity.

We look at how these values compare to our calculated *in vivo* ΔG. A plot of ΔG values calculated for ten cells measured on three separate days is given in Figure 32(a). It can be seen that there is indeed variation in the ΔG measured from cell to cell, up to 10%. These ΔG values correspond to an average K_d value of 366.9 ± 33.7 nM. The *in vitro* system consists of purified proteins freely diffusing and binding in a buffer solution whereas our *in vivo* system consists of fusion proteins interacting in a heterogeneous and highly volume occupied environment [100]. Despite these differences, a comparison between our measured *in vivo* K_d values (366.9 ± 33.7 nM) and the third presented *in vitro* value range (300 – 600 nM) shows very good agreement. Figure 32(b) depicts a

potential schematic representation of this binding interaction within our cellular system. This agreement is an indication that despite the inherent differences between the environments within which proteins are interacting, a purified protein construct consisting of both LD domains interacting with FAT *in vitro* is a sufficient representation of the Paxillin-FAT interaction *in vivo*, since full-length paxillin also contains both LD domains.

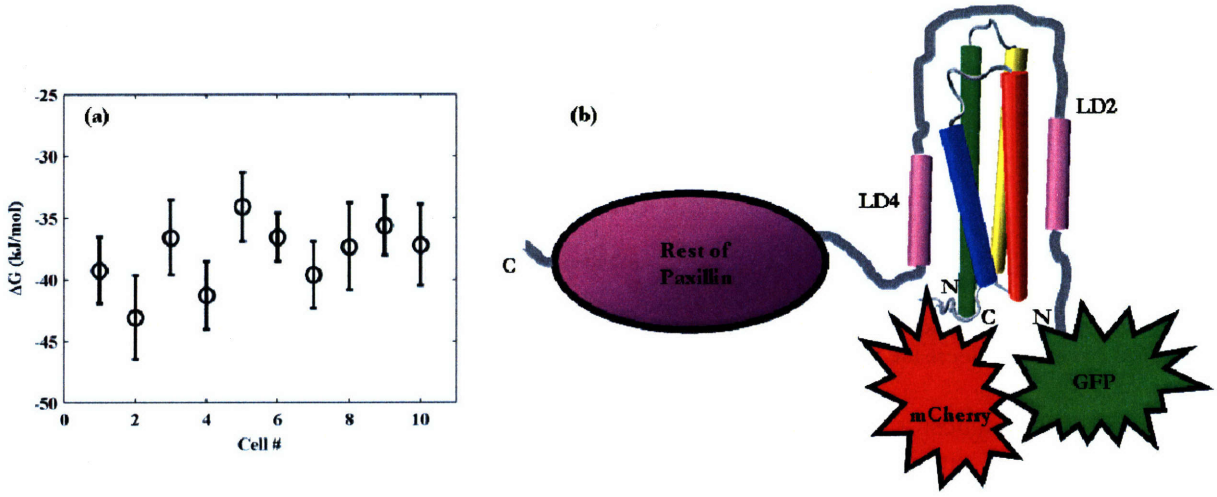

Figure 32 (a) Calculated ΔG values for ten cells measured on three separate days. Error bars denote standard deviation. (b) Schematic of potential binding interaction between FATmCh and GPax (not to scale).

In order to determine whether the cell-to-cell variation arises purely from measurement noise, we look at the effect of binning as presented in Figure 30(a). If variations seen in measurements are due purely to random noise, as pixels are averaged over kernels of increasing size, the variance should keep decreasing with the square root of the number of pixels averaged over. However, it can be seen from Figure 30(a) that this is not the case. This point is emphasized in Figure 33 which plots the expected decay in standard deviation compared to the measured decay, with increased kernel size. While both become smaller with increasing kernel size, the measured standard deviation decays at a slower rate. This leads us to conclude that there is some inherent difference in binding interaction between our proteins of interest from cell to cell.

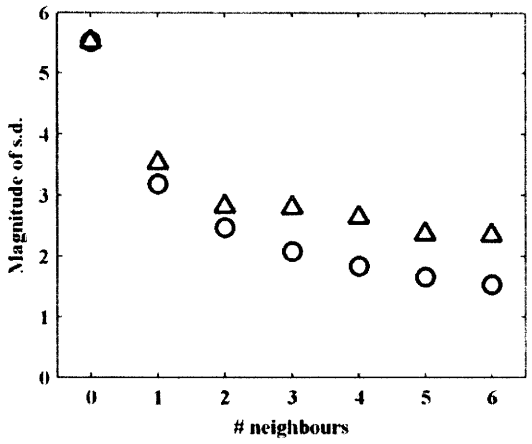

Figure 33 Expected (circles) decrease in standard deviation of ΔG with increasing kernel size, compared to measured (triangles) decrease in standard deviation of ΔG.

What our results suggest is that the same protein pair binds differentially to each other depending on their local internal environment. This goes against the grain of conventional understanding of proteins, which is that linear protein sequences lead to specific globular folds, and inter-protein interactions are determined by the contours of this fold, which do not vary over space or time. However, it is possible that this is not strictly true. It is known that paxillin has on the upward of fifteen different binding partners. It is likely that binding of GPax's many other partners could slightly modify its globular fold such that its interaction with FATmCh depends on the secondary effects caused by other binding partners as well. Different cells might be at different stages in their cycle, where different subsets of binding partners are attached to GPax, and this could lead to the variation seen. One way to 'equalize' cells would be to synchronize them by overnight serum-starving. However, it is not clear that even this is sufficient to remove the variations seen. This is demonstrated in Figure 34, which shows a GPax-transfected cell that had just undergone mitosis. The two resulting daughter cells are therefore synchronized. The cells were fixed with 4% paraformaldehyde and stained with DAPI (nucleus) and rhodamine-phalloidin (actin). As can be seen from this figure, the distribution of GPax and the actin cytoskeleton organization is different. The daughter cell on the right received more GPax than the daughter cell on the left. The actin stress fibers in the left daughter cell largely extend along the length of the cell while in the right daughter cell, stress fibers originate at a point in the center and traverse radially throughout the whole cell.

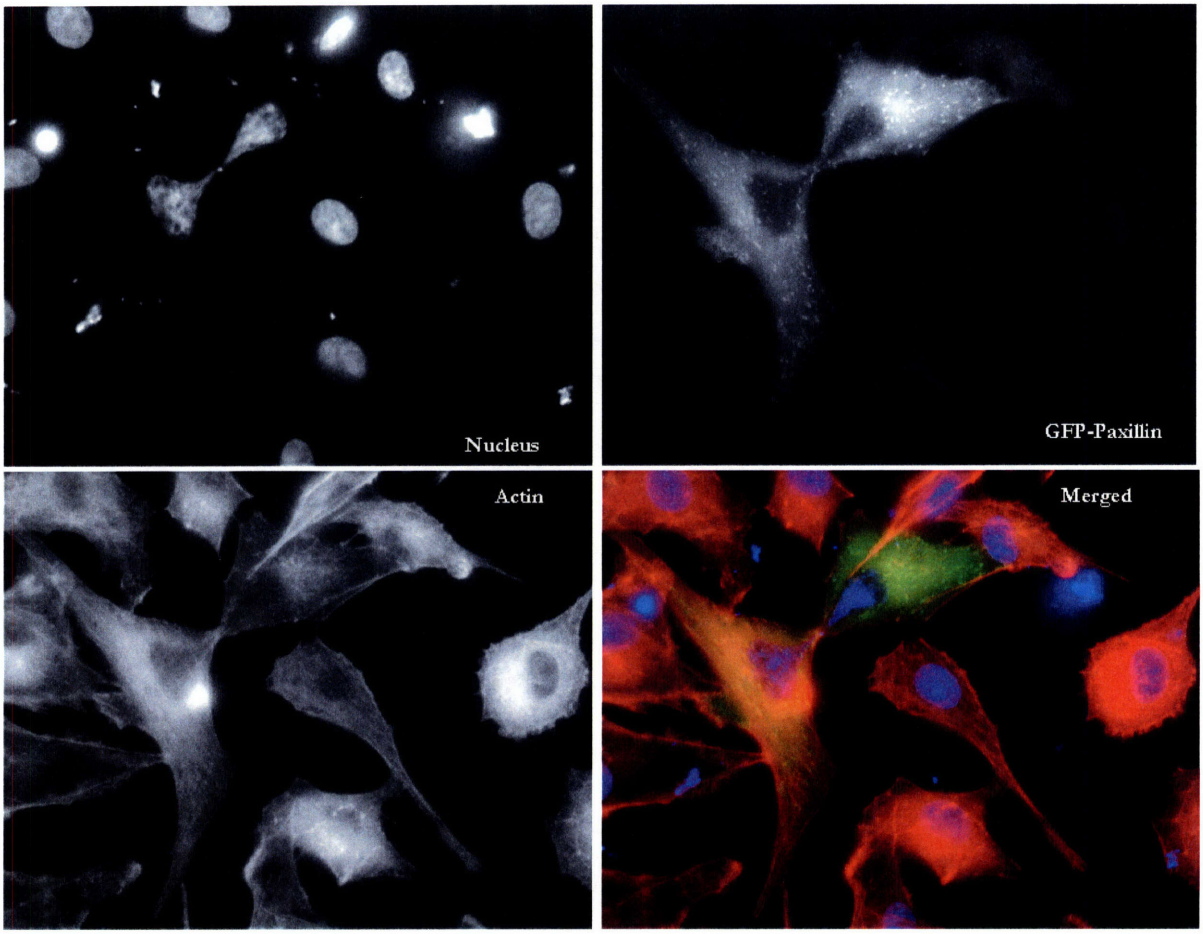

Figure 34 Epifluorescence images of GFP-Paxillin transfected cells plated in a fibronectin-coated glass-bottom-dish. Cells were fixed with 4% paraformaldehyde and stained with DAPI (nucleus) and rhodamine-phalloidin (actin).

It might be time to rethink our understanding of intracellular inter-protein interaction. Current methods used to predict or depict protein binding, for example molecular dynamics simulation [59, 85] or protein docking software [16, 148], are capable only of modeling small proteins or protein segments solvated usually in water. Conclusions obtained from these computational methods should thus always be carefully evaluated against the realities of an inherently complex intracellular environment where proteins are packed together and where binding interactions with multiple protein partners complicate the simplified one-to-one binding interaction usually depicted in computational models.

4.4.6 Comparison between FA and cytosol

We check to see as well if there are any significant differences between ΔG values calculated at FAs compared to ΔG values calculated in the cytosol. One might expect there to be some difference in the distribution of these ΔG values as FAs are mechanically and biochemically different environments compared to the cytosol. Traction forces exerted by cells onto the glass substrate presumably are transferred through the actin cytoskeleton intracellularly and are transmitted to the substrate via focal adhesions, since these are the sites of cell attachment to the substrate. The

cytosolic region does not 'feel' this force. A specific subset of proteins localize to FAs compared to those present in the cytosol, thus potentially resulting in different binding characteristics between GPax and FATmCh.

FA and cytosolic regions within cells were identified and separately grouped. As was explained in Section 3.2, FA and cytosolic regions do not necessarily both have similar intensity levels throughout the cell. While FAs are always brighter than the immediate surrounding cytosol, FA intensities are not the same throughout the whole cell. Some bright cytosolic regions might be as bright as some FA regions in other parts of the cell. Each cell is thus first segmented into regions with similar FA and cytosolic intensities, before further segmentation into separate FA and cytosolic regions. An example is shown in Figure 35, which shows the original intensity image and the same cell segmented into FA (red), cytosol (blue), and unselected regions (black).

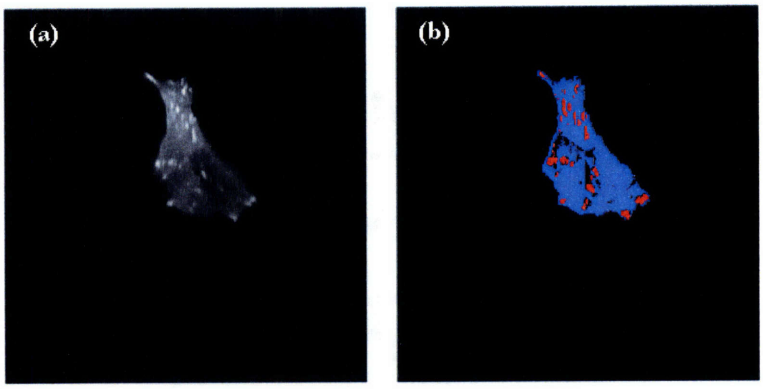

Figure 35 Segmentation of FA and cytosolic region. (a) Grayscale intensity image of double-transfected cell. (b) Cell segmented into FA (red) and cytosolic (blue) regions.

A comparison between FA and cytosolic measured values is presented in Figure 36. While there might be slight differences within each cell, these differences are not significant and no observable trend is seen, either for FR values (Figure 36(a)), or for ΔG values (Figure 36(b)). Thus contrary to expectations, differences that do exist between FA and cytosol do not appear to affect GPax / FATmCh binding. From *in vitro* binding experiments, it is known that the LD2-LD4 fragment and FAT readily associate in solution. It could be that in the cellular system, GPax and FATmCh associate in the cytosol and the complex is recruited to FAs by GPax's other binding partners, the binding of which does not affect the GPax-FATmCh interaction. If this were the case, then even at the FA, free FATmCh can freely associate or exchange to bind GPax at the same rate binding occurs in the cytosol. It could be that the GPax-FATmCh complex is perched off to one side of the direct force transmission pathway related to intracellularly generated traction. Though cell-to-cell variations observed as described in the previous chapter are real, the source of the variance is unrelated to known differences in the FA and cytosolic environments.

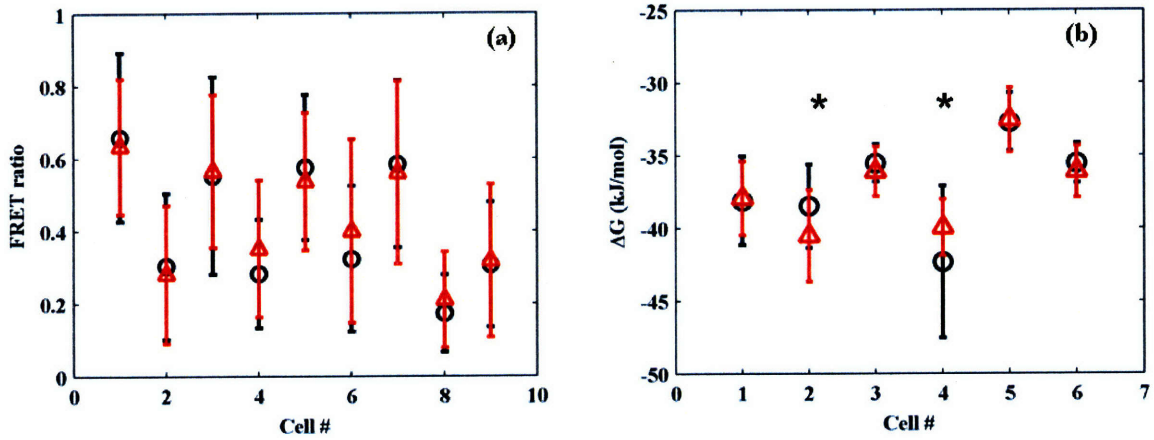

Figure 36 Comparison between values measured at focal adhesions (circles) and values measured in the cytosol (triangles). (a) FR values. (b) ΔG values. Cell numbers here are not equivalent. Error bars denote standard deviation.

4.4.7 Evaluation of assumptions and limitations

Results from FCS intensity-concentration calibration are based on the implicit assumption that the fluorescent species observed diffusing in and out of the focal volume are of the same species, all of which are free molecules available for binding. This would be untrue if other proteins bind to the fusion proteins in such a way to prevent subsequent GPax-FATmCh interaction. If the levels of all endogenous protein expression are much lower than fusion protein expression, this factor can be ignored. While this can be shown to be true for endogenous paxillin and FAK compared to GPax and FATmCh as shown in Figure 11 above, and extrapolating to other endogenous proteins lead us to the same conclusion, this point cannot be definitively proven for comparisons between protein species. If the expression levels of some endogenous fusion protein binding partners are indeed comparable to fusion protein expression levels, their binding should be evaluated. To this end, it is noted that for FAT, talin is the only other potential binding partner, and it binds onto FAT on the face that does not take part in paxillin binding. For paxillin, the LD domains involved in FAT binding are at the N-terminus, and are not involved in other binding interactions. Therefore even though it is possible that the fusion proteins bind to other binding partners, these binding interactions would probably not completely prevent GPax-FATmCh binding, though these could still affect the interaction via a distance or allosteric effect.

The presence of fusion proteins bound to endogenous binding partners could result in a distortion of the FCS autocorrelation curves and resultant fits. In terms of the effect on G(0) value, since we have shown above that most likely all fluorescent, and thus diffusing, species are available for binding, direct conversion of G(0) to concentration without any correction or scaling, is valid. This is the most important consideration for our calculations, since we are interested in concentrations and the G(0) value is very clear from the autocorrelation curves. The effect of fusion proteins with multiple binding partners on the diffusion timescale is not as obvious. Approximating the diffusing fluorescent species as a homogenous sphere, its hydrodynamic radius scales by the third root of the molecular weight [128]. Thus in order to detect a change in the diffusion timescale by at least a factor of two, binding with another partner should result in an increase of eight times the mass of the fusion protein, which is unlikely due to the similar sizes of proteins, even in the case of

FATmCh due to the presence of the fluorophore. Thus bound and unbound fusion proteins will exhibit diffusion times on the same scale, averaging to one value in our measurements.

Our imaging procedure takes at best 16 mins, as presented in the timeline of Figure 37 (a). The bottleneck in the imaging sequence lies in the time it takes to acquire a sufficiently good FLIM dataset. This time is governed by the need to acquire data for a sufficiently long time in order to build up decay curves with enough photon counts and good SNR as described in Chapter 3. Excitation power is kept low so as to not cause damage to the cell. Within this imaging time frame, the cell undergoes many processes, the most obvious of which is morphological change and motion. This is shown in Figure 37 (b) where images taken before and after FLIM were converted to binary form and subtracted one from the other. The presence of a cell outline shows which parts of the cell have changed throughout the FLIM imaging time. Due to this, our calculations should be considered an average measure over both space and time. This time could be reduced by further improvements in FLIM techniques. One example is to carry out video rate FLIM [1, 42], though finer temporal resolution is required in order to resolve multiple lifetimes. One could also explore the possibility of multifocal multiphoton [77] FLIM which would acquire images at multiple points in the sample simultaneously, thereby reducing the image acquisition time and removing motion artifacts. This technology however has yet to be developed.

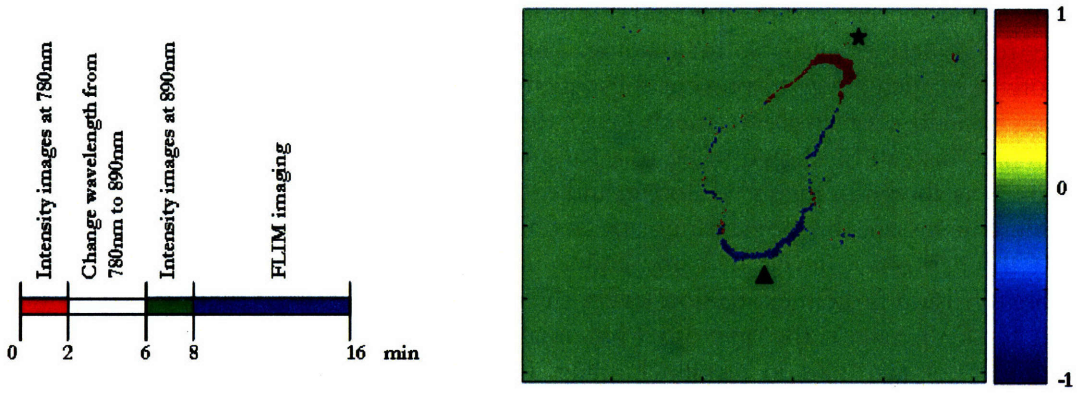

Figure 37 Imaging timescale and its effects. (a) Imaging timeline to obtain a complete dataset, i.e. intensity images at 780 nm and 890nm as well FLIM. (b) Difference in cell position before and after FLIM. After FLIM, the cell leading edge (star) has moved forward and the trailing edge (triangle) has retracted.

The main assumption made in this work that allows us to formulate the equations for our system is that the system is under thermodynamic equilibrium. While the cell might remain relatively static, internal processes that occur might affect local environments, and thus binding events, for example changes in the rate of fusion protein translation. However, the assumption of thermodynamic equilibrium within cells is reasonable considering the much longer timescale for translation, and most other cellular processes, compared to our measurement timescale.

4.6 Conclusions

We have presented here a novel method for calculating intracellular free energy of binding between two fluorescent fusion proteins. This method utilizes fluorescent microscopy techniques, FRET /

FLIM and FCS, in order to measure the interaction between free and bound proteins in our model system. The lack of published literature on measurements of intracellular K_d or ΔG is a testament to the difficulty of carrying out such a measurement. Measured intracellular K_d values are reasonable compared to *in vitro* measurements, though a direct comparison is not necessarily accurate given the differences in both actual proteins used, and in microenvironment inhabited. Expected differences between FA and cytosolic measurements were not observed, leading to the conclusion that the binding interaction proceeds similarly at the FA and in the cytosol, probably due to the GPax-FATmCh complex being perched to the side of the direct traction force transmission pathway.

It would be highly advantageous if a separate method could be used to verify our results. The use of two fluorophores in our system suggests that it would be possible to apply the TPCCS method as published by Kim et. al. [78] in order to achieve this verification. This would essentially involve carrying out FCS measurements on double-transfected cells and quantifying the autocorrelation and cross-correlation amplitudes in order to back out binding stoichiometry. Our capability of carrying out spectrally resolved fluorescence correlation spectroscopy based on global analysis (SRFCS-G) [117] readily lends itself to this measurement technique. Attacking the issue of verification from another angle, it would be possible to carry out fluorescence recovery after photobleaching (FRAP) measurements to compare k_{off} between fusion proteins at FAs (reaction-limited) compared to those at the cytosol (diffusion-limited). However, measurements obtained would relate to fusion protein association / dissociation to / from FAs as a whole compared to diffusion in the cytosol, and not between our specific fusion protein pair. Thus verification would be difficult to achieve.

With the successful application of our method, we hope to pursue measurements in other systems that will help to increase our understanding of the complex protein networking inherent in biological systems.

Chapter 5 Force-Induced Changes in Intracellular Free Energy (ΔG)

5.1 Introduction

Cells are very sensitive to their physical environment and adapt accordingly, depending on the cues they receive. For example, the same type of cells can have very different morphology depending on the stiffness of the substrate they are plated on. Fibroblasts and endothelial cells are more spread, with strong actin stress fibers when cultured on substrates with stiffnesses higher than 2 MPa, though this stiffness-dependence disappears upon confluence [167]. Smooth muscle cells also spread and organize their cytoskeleton and FA much more so on rigid compared to soft surfaces [43]. Cell migration has been shown to occur preferentially from soft to hard surfaces [91]. In probing further into the cell to the protein-level substrate stiffness-dependent changes that might be occurring, Lele et. al. discovered that the dissociation rate, k_{off}, of FA protein zyxin from FAs increases with a decrease in substrate stiffness, though the same observation cannot be made for Vinculin [87].

Direct perturbation of the substrate that cells are plated on, also result in observable changes to the cells. A 10% cyclic stretch results in alignment of endothelial cells perpendicular to the direction of stretch within 4 hrs of onset of stretch [103]. Fibroblasts experiencing 20% uniaxial stretch at 1 Hz showed increase in FAK Y925 phorphorylation which peaked at 20 min after start of stretch. This was followed by MAPK activity [158]. A steady stretch applied to rabbit aortas maintained in organ culture resulted in increased FAK phosphorylation to maximal levels by 5 mins of stretch, the effect of which was reduced by addition of kinase inhibitor PP2 [86].

We seek to study whether, and how, the interaction between our protein pair of interest, GPax and FATmCh, is affected by the variation in substrate stiffnesses that it sees, as well as by a 10% step change in strain applied to its substrate. This is done by calculating the free energy of binding between these proteins using the method presented in Chapter 4 and comparing these values for the different treatments meted out to the cells. In order to gain insight into the origin of changes seen, we attempt to abolish it by adding cytochalasin D which disrupts the actin cytoskeleton or genistein, a tyrosine kinase inhibitor.

5.2 Materials and methods

5.2.1 Cell preparation

Bovine aortic endothelial cells (BAECs) were cultured in Dulbecco's Modified Eagle Medium (DMEM) (Gibco, Invitrogen, Carlsbad, CA) supplemented with 10% fetal bovine serum,1% penicillin/streptomycin, and 1% L-glutamine. Cells were seeded at a density of 350,000 cells/well in fibronectin-coated 35mm glass-bottom (#1.5) dishes (MatTek Corporation, Ashland, MA). Transfection was carried out at time of cell seeding either or both GFP-Paxillin (GPax), FAT-mCherry (FATmCh) plasmids, using the FuGene6 transfection reagent from Roche Diagnostics (Indianapolis, IN) and manufacturer's transfection protocols. Just before imaging, cells were washed with PBS, and DMEM supplemented with 10% fetal bovine serum, 1% penicillin/streptomycin, and

1% L-glutamine but with no phenol red was replaced in the wells. A complete set of intensity and FLIM imaging as described in section 5.2.4. was carried out 24 hours after transfection.

For chemical disruption experiments, cells were incubated with 2 μM cytochalasin D (Sigma-Aldrich, MO) for 30 mins prior to imaging or with 100 μM Genistein (EMD Biosciences, CA) for 60 mins prior to imaging. Cells are subconfluent at time of imaging.

5.2.2 Substrates of varying stiffnesses

PDMS (Silgard 184, Dow Chemical) was mixed at a 1:10 (PDMSstiff) and 1:90 (PDMSsoft) weight ratio of curing agent to elastomer. The mixture was mixed vigorously and degassed for 40 mins. 35 mm #1 glass coverslips (VWR, PA) were spin-coated with PDMS at 500 rpm for 10 s and 1500 rpm for 60s (convention used for speed regimes hereafter is 500:10/1500:60). Coated coverslips were left to dry at room temperature (RT) for 30 mins before being baked in the oven at 80°C for at least 3 hrs. Wells were cut out of a 0.5" tall PDMS piece. Dust was removed with tape from both baked coverslips and PDMS wells before autoclaving. Coverslips and wells were plasma treated by plasma cleaner (Harrick, CA) in air environment for 45 s to increase hydrophilicity and immediately bonded together. Bonded wells were incubated in the oven for 10 mins to enhance bonding strength. Wells were coated with 5 μg/ml fibronectin for 2 hrs in the incubator before cell seeding and transfection.

Collagen gel of concentration 2 mg/ml were prepared at pH 7.4. An ice-cold mixture was prepared in an eppendorf, containing 20 μl 10X PBS (Lonza, PA), 7.6 μl 0.5N NaOH, 85.3 μl distilled, deionized water (Cellgro, VA), and 87.1 μl 4.59 mg/ml collagen (BD Biosciences, MA). Cell culture wells were made from plasma treated #1 glass coverslips (VWR, PA) bonded to PDMS wells. 10 μl collagen gel solution was dropped onto the surface of the well and the well was tilted to even out collagen distribution. Gels were allowed to polymerize in the incubator for at least 20 mins before cell plating. Care has to be taken when exchanging DMEM or other liquids as surface tension makes the collagen gel susceptible to peeling off the glass surface.

Cells plated on stretchable silicone sheets (Specialty Manufacturing, Inc., MI) in the stretch device were included in substrate stiffness comparison. A schematic of cells on various substrates is shown in Figure 38.

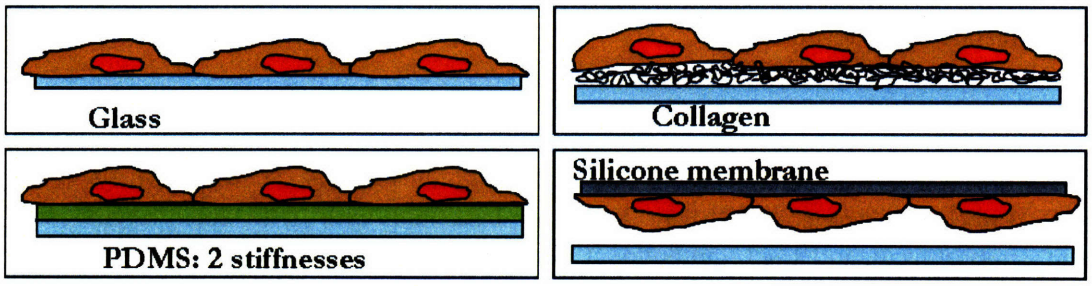

Figure 38 Schematic of cells plated on substrates of varying stiffnesses.

5.2.3 Stretch device

A schematic of our stretch device is given in Figure 39. The major design principle governing this choice of device is that it is modular, facilitating the culture of multiple sets of cells for imaging

during the same imaging session. Once assembled, cells are in an enclosed, sterile compartment, suitable for long-term monitoring. Another strong advantage is that the distance between the membrane, where cells are plated, and the glass coverslip is held constant while stretch is applied. This is important in order to ensure focus on the cell adhesion plane is not lost throughout application of stretch, especially since cell position changes in the x-y plane with applied stretch. The device results in an equibiaxial strain profile [84].

A silicon sheet (Specialty Manufacturing, Inc., MI) of size 2" x 2" was affixed to the membrane holder with 1/16" O-ring (McMaster-Carr, NJ). Wells were cut out of a 0.5" tall PDMS piece and adhered onto the silicon sheet. Surface contact is sufficient to provide a good seal between the membrane and PDMS. This assembly was incubated with 5 μg/ml fibronectin applied to the membrane for 2 hrs before cell seeding and transfection. To assemble the device for imaging, high vacuum grease (Dow Corning, was applied to the outer edge of a #1 glass coverslip (VWR, PA) and the coverslip was carefully lowered into the base and firmly attached to the bottom, resulting in a complete seal around the coverslip. 2 ml and 0.3 ml DMEM with no phenol red was added to the base and cells respectively. Castrol grease (Structure Probe, Inc, PA) was applied to the piston tip to ensure good lubrication and facilitate slip between the piston tip and the membrane during strain application. The cell culture assembly was affixed to the piston with 3/16" screws (McMaster-Carr, NJ), being very careful to use a spacer to prevent the piston from applying strain to the membrane at this time. The PDMS piece was removed and the whole assembly was inverted and lowered into the base, having first removed the spacer. Care was taken to ensure no air bubbles were trapped between the membrane and the glass coverslip. The piston was affixed to the base with 3/16" set screws.

Stretch device calibration was carried out by measuring ink marks on the membrane as stretch is applied. A plot of strain against number of screw turns (Figure 40) shows that a strain of 10% can be achieved with 4 ¾ screw turns. This is close to the value calculated directly from device dimensions. This manual application of a 10% step strain requires 40s.

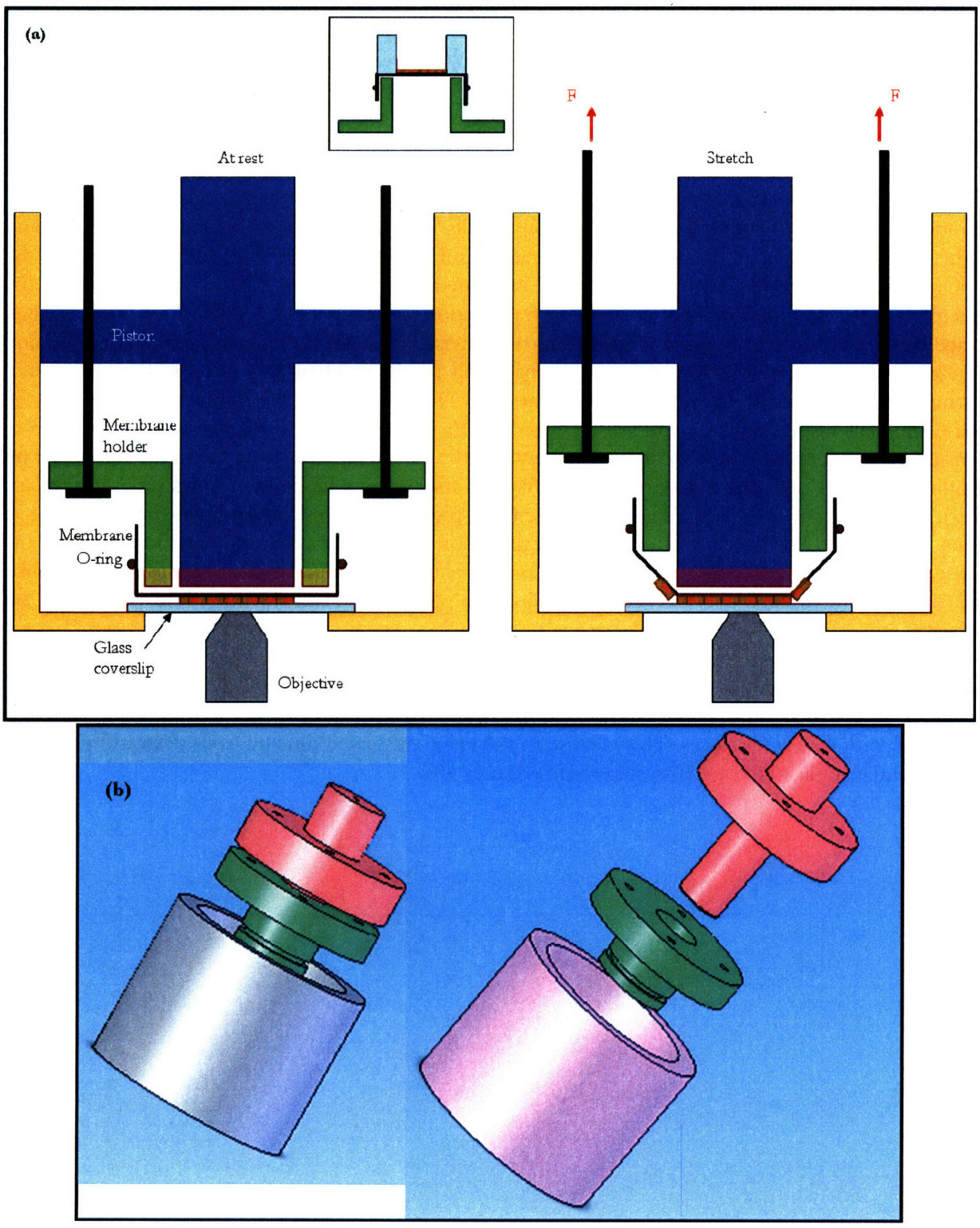

Figure 39 Equibiaxial stretch device. (a) Schematic of the stretch device before and during applied stretch. Membrane holder orientation with cultured cells when in the incubator is shown in the inset. (b) Solidworks drawings of the device in two exploded view configurations, for clearer detail.

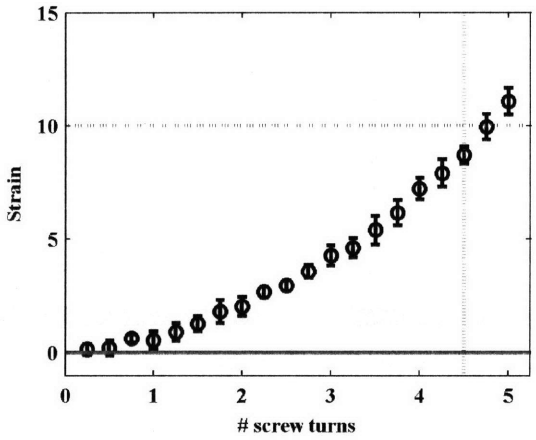

Figure 40 Calibration of stretch device. Percentage strain with number of screw turns was measured. Measured values for number of turns required to obtain 10% strain matches value calculated from device dimensions.

5.3.4 Instrumentation and imaging procedure

Substrates of different heights and compositions would have different optical properties compared to #1.5 glass coverslip. Since FCS intensity-concentration calibration was carried out on cells plated on coverslips, direct intensity scaling is inaccurate and would distort the resultant calculation of ΔG values. In order to correct for this, the variation in intensity of 10nM Alexa Fluor 488 (Molecular Probes, Eugene, OR) was measured in the different experimental setups.

Cell selection for imaging for cells on different substrates as well as cells in the stretch device follows the protocol given in Sections 4.3.3 and 4.4.4. Care is taken to select cells using the BP590-35 filter first, in order to ensure sufficient counts from FATmCh. Since mCherry is a dim fluorophore and is stringently selected by our choice of filter sets, it is more susceptible to noise, which distorts the resultant ΔG calculations.

For cells plated in the stretch device, initially a complete set of intensity-FLIM images was taken, 10% strain was applied, and another complete set of intensity-FLIM images was taken for the same cells. The imaging protocol is identical for chemical disruption experiments, with imaging commencing after the above-mentioned incubation times. The experimental timeline is presented in Figure 41 below. An equilibration time after application of step strain of 5 minutes was chosen as FAK phosphorylation was shown to peak at 5 minutes after application of stretch [86].

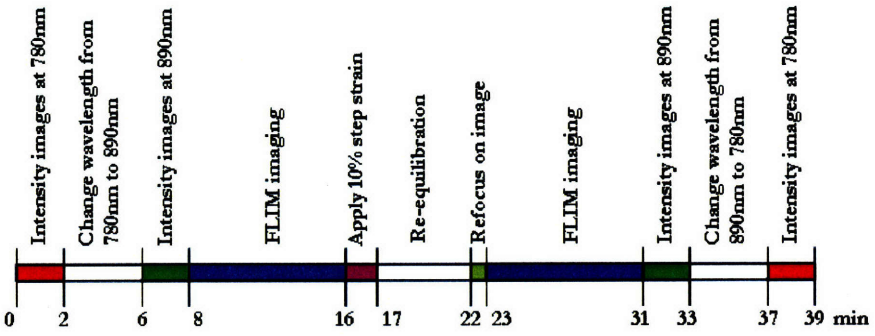

Figure 41 Timeline for stretch experiment.

All plots of ΔG show results after scaling FR and mean filtering.

5.3 Results and discussion

5.3.1 Substrate characterization

In order to study the effect of substrate stiffness on the binding interaction of GPax and FATmCh, ΔG values were calculated for cells on glass, PDMSstiff, PDMSsoft, collagen, and silicone membrane. Glass has a very high stiffness of ≈ 80 GPa. A frequency sweep of both PDMS samples at 1% strain was made in a cone-plate rheometer (20 mm, 2° steel cone). Prepared samples were deposited and results are plotted in Figure 42. PDMSstiff is dominated by the storage modulus, giving it a stiffness of ≈ 10 kPa, while the stiffness of PDMSsoft contains almost equal contribution from both storage and loss moduli, giving it a stiffness of ≈ 50 Pa. It should be noted that the stiffness of PDMSstiff usually found in the literature is on the order of 10 MPa [160], leading us to believe that the moduli as output by the cone-plate rheometer is a measure of stiffness, but is not the actual storage or loss modulus. The pH 7.4 collagen gel of concentration 2 mg/ml has a stiffness of ≈ 20Pa [161], and the silicone membrane has stiffness in the kPa range, estimated by qualitative comparison between the membrane and thin PDMS sheets.

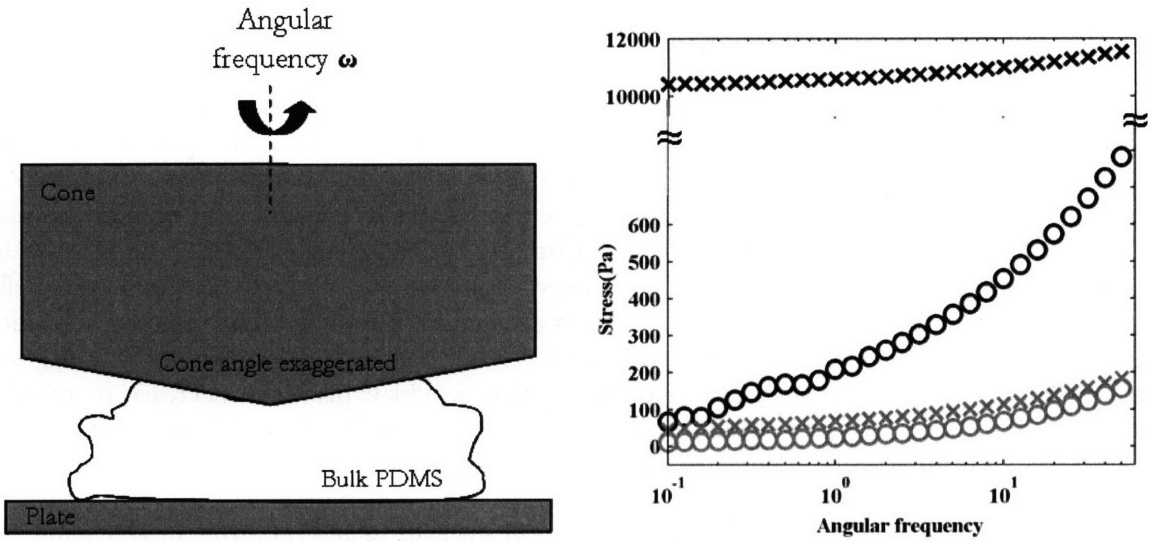

Figure 42 Cone plate rheometry. (a) Cone plate rheometry experimental setup for measurement of bulk modulus of PDMS. (b) Cone plate rheometer measurement of PDMS stiffness. G' (x) and G" (o) was measured at varying angular frequency for both PDMSstiff (black) and PDMSsoft (gray).

The thickness of spin-coated PDMS was measured optically. Sample thickness distribution across the diameter of the coverslip and 1:10 ratio PDMS coatings of two thicknesses is plotted in Figure 43. Our measurements for the thickness of a #1 glass coverslip (closed circles) match the manufacturer's range of 140 – 170 μm. Squares are measurements of a layer deposited with the spin regime of 500:30/1500:60 and triangles are measurements of a layer deposited with the spin regime of 100:30/1500:30. As expected, a longer spin results in thinner coated layer. PDMS layers used for cell experiments have thicknesses of ≈ 50 μm. The thickness of collagen gel could not be measured. However, from estimates calculated relating volume of gel put down to surface area covered, average height is also ≈ 50 μm.

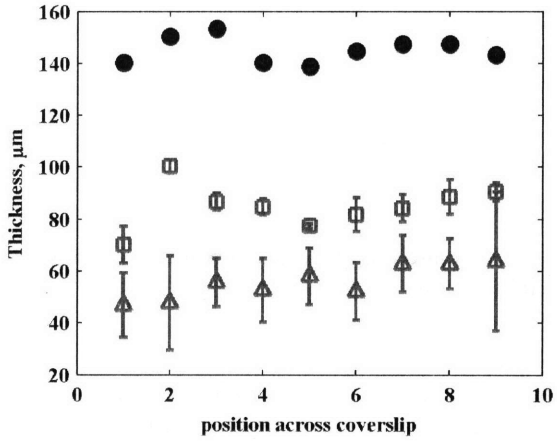

Figure 43 Thickness of spin-coated PDMS, spun with two different spin profiles, compared to the thickness of #1 glass coverslip. Closed circles: #1 glass coverslip, squares: spin regime 500:30/1500:60, triangles: spin regime 100:30/1500:30.

5.2.2 Effect of substrate stiffness on ΔG

The morphology of cells plated on substrates softer than glass did not show a significant difference compared to cells plated on glass. However, it was quite obvious that cells plated on softer substrates ($cell_{subs}$) have FAs that are not as bright as FAs in cells plated on glass ($cell_{glass}$). This was subjectively evaluated by comparing the relative intensity between FA and cytosol between the various sets of cells, where the intensity of FA compared to cytosol is high in $cell_{glass}$ but is lower in $cell_{subs}$. Since internal cell stress balances external stress, being on softer substrates means that cells do not have to exert such high stresses. This has been shown by others who observed substrate stiffness dependence of traction forces exerted by cells [91, 95]. Taking it a step further, this suggests FA plaques that contain fewer constituent proteins. This would explain the decrease in relative intensity between FA and cytosol, which made it more challenging to find and focus on the FA plane. Therefore, results presented here are representative of cytosolic measurements of ΔG.

The plots in Figure 44(a) compares ΔG values calculated for cells plated on different substrates, as labeled. ΔG values do not vary by more than 3% regardless of substrate type. Averaging ΔG values over all cells within each substrate group emphasizes this point (Figure 44(b)). Whatever variation exists from sets of cells is found not significant (student t-test).

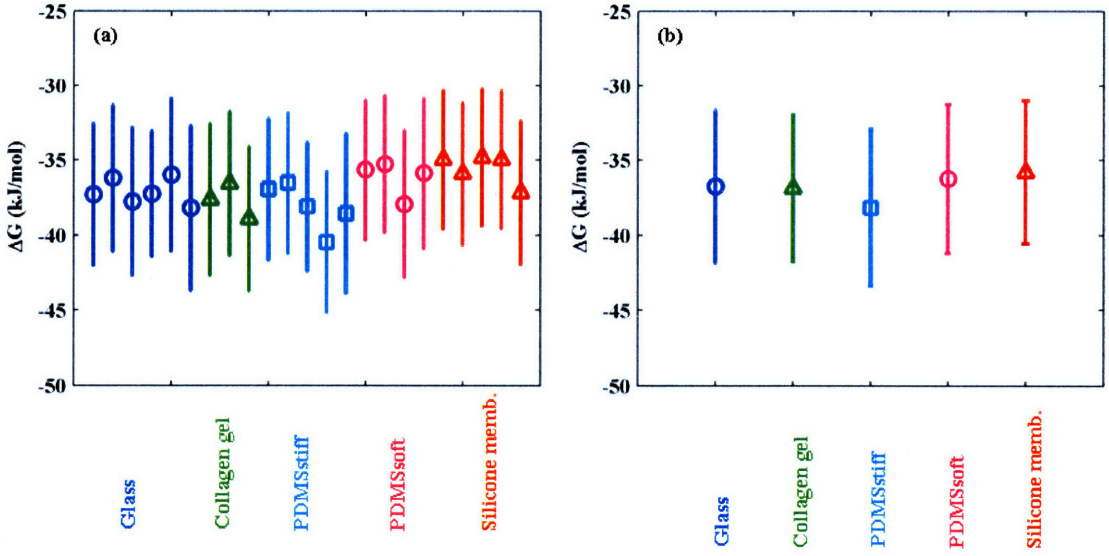

Figure 44 ΔG values calculated for cells plated on different substrates, as labeled. (a) Individual ΔG values for each cell measured. (b) Average ΔG values for each substrate type.

This finding is not too surprising. We already have evidence, from Chapter 4, that there exists no significant difference between ΔG values calculated at FAs compared to cytosol, even though the local microenvironment is mechanically and biochemically different. Thus even though cells plated on different substrates exert different internal stresses, at the time of imaging, they are all at a steady state condition which does not affect the binding interaction between GPax and FATmCh.

5.3.2 Effect of 10% step strain on ΔG

A 10% step strain was applied and ΔG values were calculated and compared for the same cell before and after strain. Intensity comparisons between cell intensity before and after applied stretch show a 35.9% decrease in GPax intensity (Figure 45(a)), and a much smaller decrease of 5.5% in FATmCh intensity (Figure 45(b)).

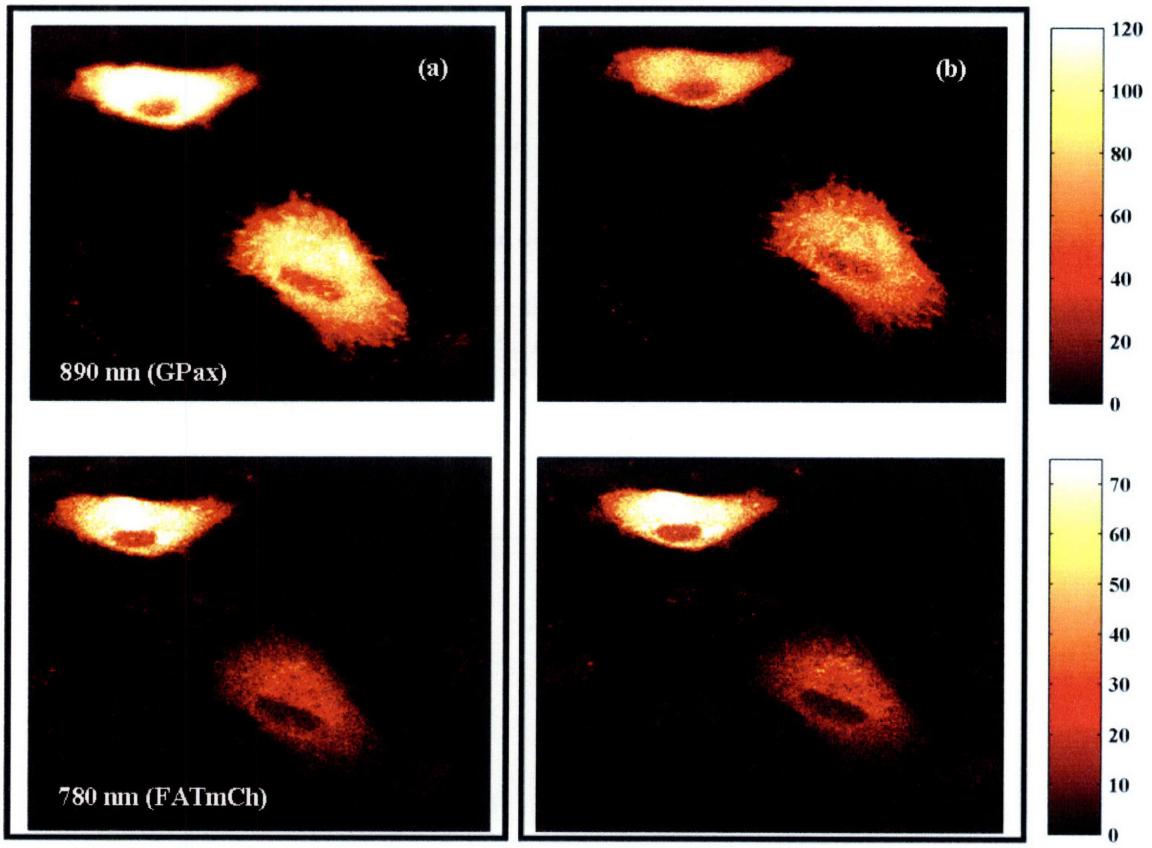

Figure 45 Intensity images of double-transfected cells in the stretch device, at λ = 890 nm (exciting GPax) and λ = 780 nm (exciting FATmCh), both (a) before and (b) after stretch application.

Directly from FLIM global analysis fits, it can be seen that FR shifts to higher values upon stretch, on average 0.072 ± 0.008, or 18.6% (5 cells). Shifts are significant for all pairs (student t-test). A representative histogram of FR distribution for cells under static and stretch conditions demonstrates this (Figure 46). A lower histogram height upon stretch, corresponding to fewer total pixels, is also an indication of the loss in GPax intensity, since the same intensity threshold cutoff (LL500) was used in both cases when selecting pixels for which to carry out FLIM analysis. Besides this, there was also a difference in fitted FRET lifetime, τ_F, the lifetime being lower by 4.8% upon stretch. A lower τ_F corresponds to a slight conformational change that brings the fluorophores closer by 2 Å.

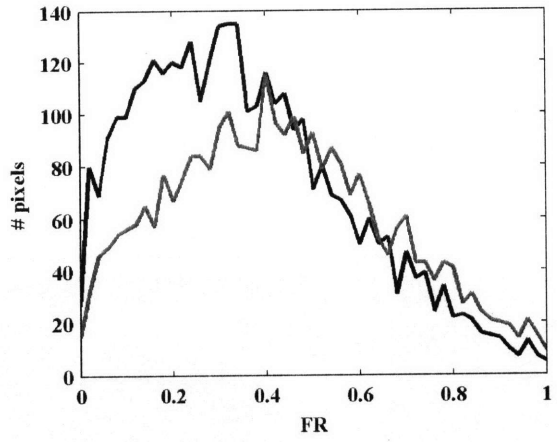

Figure 46 Histogram of FR distribution under static (black) and stretch (gray) conditions.

The effect of 10% step strain on ΔG values for 5 different cells is shown in Figure 47. Overall, there is a shift to lower ΔG values upon application of stretch, whereby all shifts are significant (student t-test) except for one pair. Overall, a reduction of 5 ± 1% is observed. A lower ΔG value corresponds to a smaller K_d, which indicates a tighter binding interaction. Grouping all ΔG values together before and after stretch before carrying out comparisons also results in similar conclusions.

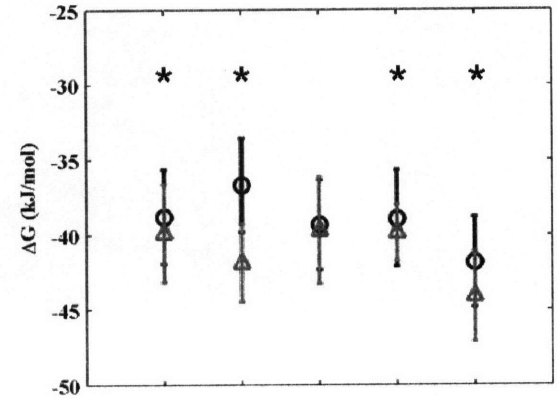

Figure 47 Comparison of ΔG values calculated for 5 cells under static (circle) and 10% strain application (triangle). Significant difference is indicated, P<0.05.

In order to verify that the change is real, complete intensity-FLIM measurements were carried out on cells cultured in the stretch device, with a time interval of 15 mins between complete sets, but without application of stretch. 15 mins corresponds to the average time it usually takes between static and stretch imaging of the same cells. ΔG values were then compared. This is to remove the effect of time as a potential factor in the change seen in ΔG values. Results of this are shown in Figure 48. The one pair with a significant change shows a change in the opposite direction to the change observed upon stretch. Therefore, overall there is no significant change in ΔG values. FLIM global analysis fits also show no significant change in either τ_F or FR. This confirms our observation that the application of stretch results in an enhancement of GPax – FATmCh binding.

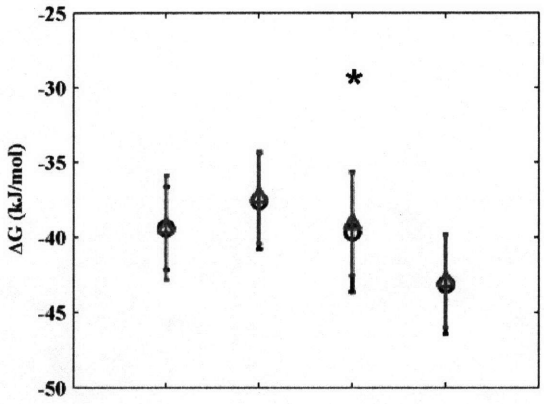

Figure 48 Comparison of ΔG values calculated for static cells before (circle) and after (triangle) a 15 minute time interval. Significant difference is indicated, P<0.05.

5.3.3 Effect of chemical disruption on stretch-induced ΔG

A very interesting observation that can be made related to the changes in ΔG values we measure is that it reflects global changes occurring throughout the cell, since we average values over the whole cell. Therefore, the effect of force that is directed into the cell through the FAs is translated into signals that are able to propagate throughout the whole cell. This most likely points to some kind of soluble factor(s) effect. There are many factors that could give rise to the change seen in ΔG values, including direct mechanical effect [87], a phosphorylation enzyme effect [131, 158], Ca^{2+} signaling [135], and oxidative stress [68]. It might well be impossible to specifically tease out the actual factor(s) that effects changes seen in ΔG values. However, it is possible to try and negate the changes seen, by blocking specific processes within the cells an examining how the response changes (or not). We biochemically alter the cell by adding either cytochalasin D or genistein to the system.

Cytochalasin D acts by capping the barbed end actin of actin filaments while allowing depolymerization at the pointed end to still occur. This results in dismantling of the intracellular actin network as shown in Figure 49(a). Genistein is an ATP-competitive tyrosine kinase inhibitor, the addition of which therefore blocks any potential tyrosine phosphorylation signaling within the signal transduction cascade. Addition of genistein to the system does not result in any observable morphological changes (Figure 49(b)) or changes in actin filament organization.

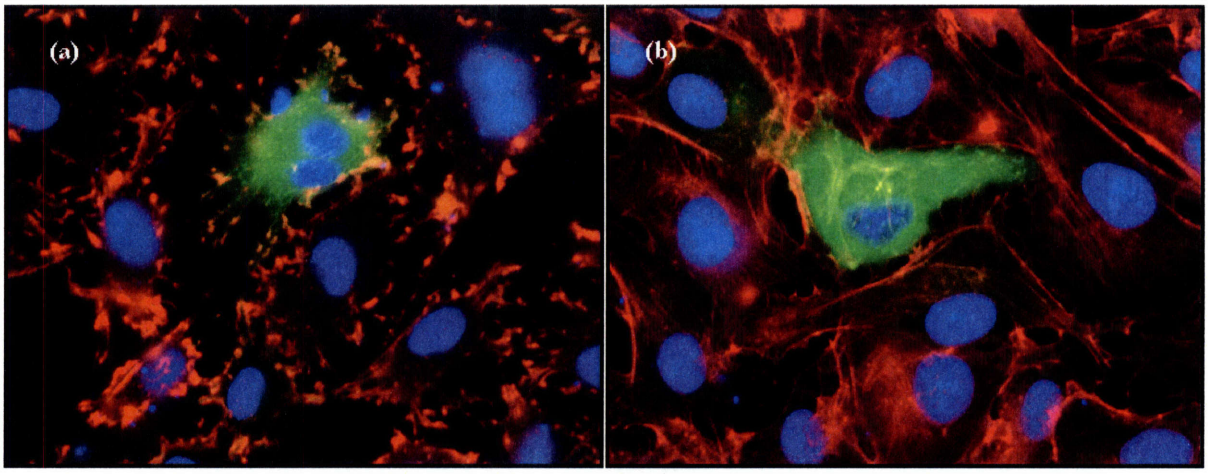

Figure 49 Images of cells plated on fibronectin-coated glass-bottom-dishes, transfected with GPax and fixed with 4% paraformaldehyde. Cells were stained with nuclear stain, DAPI (blue), and actin stain, rhodamine-phalloidin (red). (a) Effect of cytochalasin D. (b) Effect of genistein.

The effect of adding these two biochemical reagents (cytochalasin D 4 cells, genistein 6 cells) to the system is quantified in Figure 50. Firstly, the results of FLIM global analysis fits are plotted in Figure 50(a) whereby the percentage difference in τ_F obtained for fits on static and stretch cells are compared. As previously explained, stretch leads to shortening of τ_F, corresponding to a decrease in interfluorophore distance. Merely adding a time interval does not significantly change the lifetime, and nor does addition of cytochalasin. This means that with these two treatments, interfluorophore distance remains constant. Addition of genistein brings back the decrease in interfluorophore distance. Next, the overall percentage difference in ΔG values calculated under static and stretch conditions are plotted in Figure 50(b). Lastly, a pixel-by-pixel percentage difference in ΔG values was calculated and plotted in Figure 50(c). As can be seen, all plots display a similar overall trend. A positive stretch response corresponds to a decrease in interfluorophore distance, i.e. the proteins are holding on to each other slightly tighter. Merely adding a time interval between images removes the effect of stretch on calculated ΔG values. Addition of cytochalasin D results in a slight lowering of the stretch response, though a change is still noted, while the addition of genistein does not alter the stretch response. Though there is a significant difference between a stretch and time interval response, there is no significant difference between a stretch response and responses associated with either biochemical disruption.

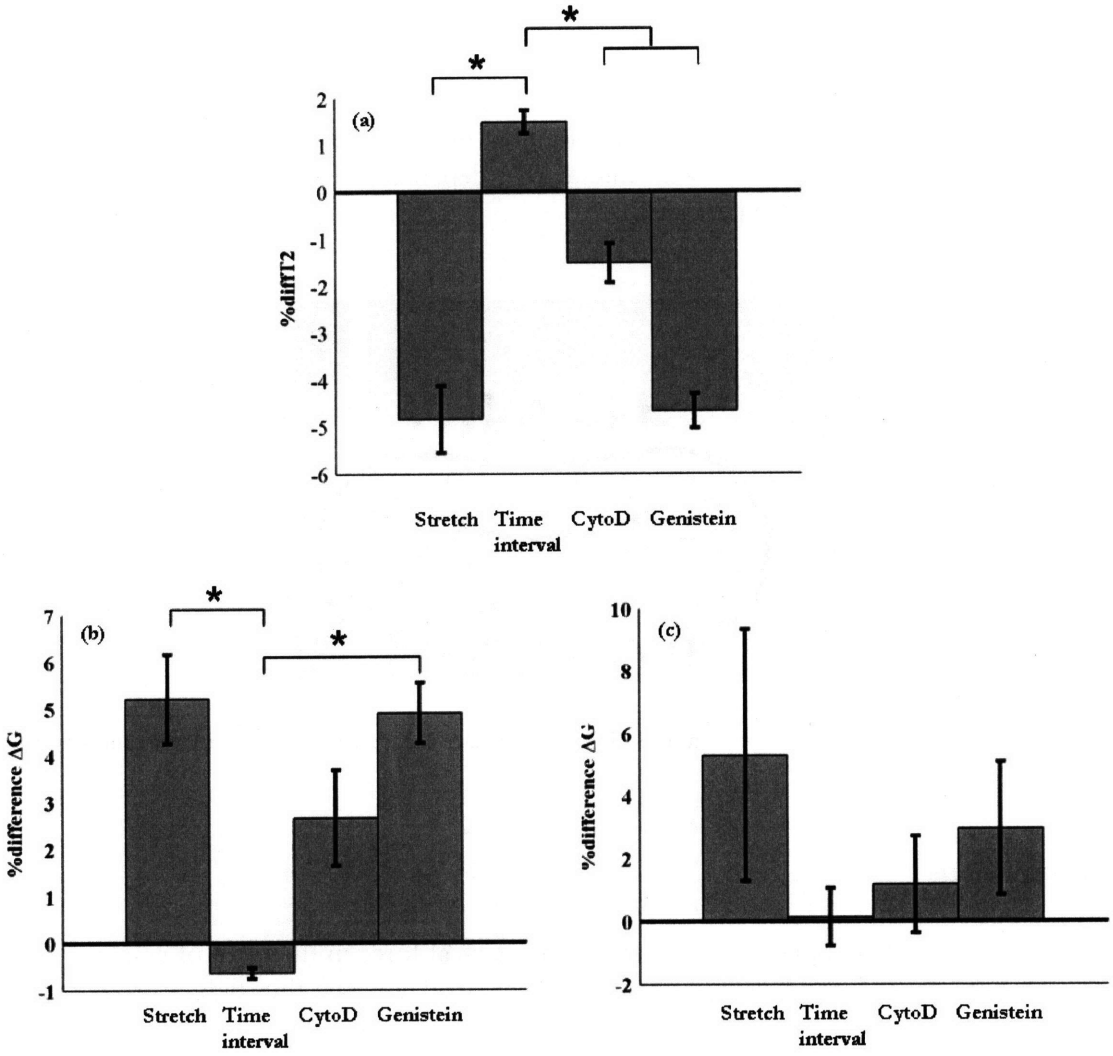

Figure 50 Stretch response with various treatments. (a) Percentage change in fit τ_F. (b) Percentage change in overall measurement of ΔG. (c) Percentage change in per-pixel measurement of ΔG.

From our data, blocking of Tyr phosphorylation preserves the stretch response. This means that it is not the Tyr phosphorylation pathways that lead to stretch-induced signaling, as applied to our system of GPax – FATmCh binding. It might seem that cytochalasin D slightly reduces the stretch response. If this is indeed true, changes in GPax – FATmCh binding is caused in part by a direct physical effect of the applied mechanical force. A look at the lifetime data also leads us to postulate that physical changes in protein conformation is what (at least partially) gives rise to changes seen in ΔG values. However, without better statistics, this conclusion is not definitive.

5.3.4 Variations in regional stretch response

A closer look at the per pixel percentage difference in calculated ΔG values, on a whole cell level, demonstrates to us that different regions of the cell actually experience different amounts of changes in ΔG values, in terms of both magnitude and direction (Figure 51). Though GPax – FATmCh

binding becomes tighter overall (positive percentage difference), there are some regions (negative percentage difference), that exhibit a weakening of interaction. Thus it can be concluded that the stretch response is not uniform throughout the whole cell. This really drives home the point that the intracellular environment is quite heterogeneous, and that the same external mechanical perturbation can cause differential responses on protein interaction, depending on its location, and most likely also depending on its other binding partners.

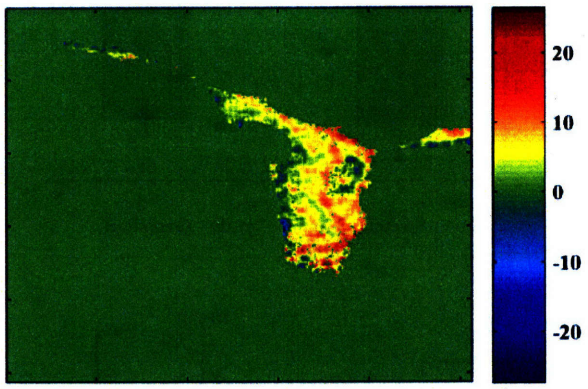

Figure 51 Cell pseudo-colored by the percentage difference in ΔG values under static and stretch conditions, calculated on a per pixel basis.

5.4 Conclusions

In this work, we show that application of external mechanical force in the form of equibiaxial strain results in a shift in ΔG to lower values, corresponding to smaller K_d and thus tighter protein binding, between our proteins, GPax and FATmCh, compared to static conditions. This change directly correlates with a change in $\tau_{F'}$. In other words, the change in ΔG values correlates with change in interfluorophore distance, which we translate to directly reflect changes in average inter-protein distance between GPax and FATmCh. Simply taking measurements at a time interval similar to the time interval between static and stretch measurements abolishes the changes seen, thus negating time interval as the source of changes seen. In order to explore other potential sources of change, biochemical disruption was affected by adding either cytochalasin D or genistein, to either disrupt the actin cytoskeleton network or to block Tyr phosphorylation. While genistein preserves the stretch response, observations related to cytochalasin D are not as conclusive. The response is reduced slightly, though statistical significance cannot be established. These results lead us to the conclusion that some other factor(s) not related to these specific biochemical disruptions is what causes the stretch response.

Though it was argued in the previous chapter that endogenous protein expression levels are much lower compared to fusion protein expression levels, this cannot be readily verified. If this were untrue, the presence of endogenous proteins and subsequent activation upon stretch application could explain our observations. One example relates to the binding between talin and FATmCh. Assuming talin binding of FATmCh displaces GPax, it is possible that under stretch conditions, competitive binding of talin for FATmCh displaces GPax, thus affecting FATmCh-GPax binding.

Since changes are seen globally throughout the cell, another potential explanation is that within the 5 minutes allowed for equilibration, fusion proteins at FAs are continuously modified and cycle out into the cytosol at a rate governed by the fusion protein turnover rate at FAs. Published fluorescence recovery data of GFP-Pax in FAs [30] shows that the k_{off} for GFP-Pax is 0.015 s^{-1} when the recovery curve is fit with an exponential as demonstrated by Lele et. al [87]. Given a best case estimate of FA area being 10% of cytosolic area at the adhesion plane (based on Figure 18), and FA height being 10% of cell height, FA volume is roughly 1% of cell volume. FA intensity is on average 1.5 times cytosol intensity at the adhesion plane, as seen also in Figure 18. Thus in total, the number of fusion proteins in all FAs is 0.015 times the number of fusion proteins in the cytosol. In order to replace all cytosolic fusion proteins with fusion proteins modified at the FA, 66.7 turnover events are required. Within the 5 minutes allowed for equilibration, the total number of turnover events is 5 x 60 x 0.015 = 4.5. Even allowing for the 22 mins it takes to complete an imaging set (as shown in Figure 41), this number increases only to 20. Therefore this is an unlikely explanation for the changes seen in our results. The other explanation is that it is most likely an effect related to some other soluble factor(s) that has as yet not been identified.

Even with chemical disruption, the magnitude of change in ΔG values calculated correlates with the change in fit τ_F. This really is a major strength in our measurement technique, compared to measuring K_d with TPCCS [78]. With our technique, the origin of change in measured values can hereby be directly linked to changes in inter-protein distances, thus relating the mechanotransduction phenomena to molecular conformational change.

Chapter 6 Conclusions and Future Directions

6.1 Summary

The central contribution of this work is the ability to measure the intracellular binding constant, ΔG, between fusion proteins of interest, GPax and FATmCh. The method combines two-photon fluorescence microscopy techniques FRET / FLIM and FCS in order to quantify intracellular protein concentrations and thus binding constants. It was demonstrated that care has to be taken when utilizing global analysis as a tool to interpret FLIM data. A methodology for including low SNR data inherent in cell-based measurements was presented, along with a way to correct for this.

Interestingly, cell-to-cell variation in ΔG exists even when random noise has been accounted for. This leads us to the conclusion that a protein's globular structure is not rigid or fixed inside the cell, but probably varies depending on its microenvironment and likely its binding partners. Surprisingly, there was no correlation between ΔG calculated in FAs compared to those in the cytosol, even though these are two very different intracellular regions, both mechanically and biochemically.

Though cells in general behave differently depending on their substrate stiffness, we do not see any substrate-dependence in the binding interaction of our protein pair. However, application of a 10% step stretch results in a tighter binding interaction. Time interval alone does not account for this change. Addition of genistein preserves the change though addition of cytochalasin D slightly reduces the effect. Our conclusion from this is that Tyr phosphorylation is not responsible for the strengthening of binding, but that the direct mechanical force transmission is in some way a contributing factor. Elucidating the actual source(s) would be difficult.

6.2 Future work

The method developed in this thesis for calculating intracellular binding constant, ΔG, provides a very useful tool with which the binding characteristics of other important protein pairs can be elucidated.

6.2.1 Alternative protein pairs

Protein pairs exist that demonstrate a higher potential to be mechanosensing elements within the FA force transmission pathway. This includes talin and vinculin, as well as zyxin and VASP. Talin binds directly to integrin and actin, through its head and tail domains respectively. External force application would travel from the extracellular domain through integrin and talin, to the actin cytoskeleton. Thus force perturbation could cause direct and measurable conformational change in talin. Talin also has multiple vinculin binding sites along its rod domain, most of which are cryptic and could be exposed with tensile force along the protein. The method could also be applied to other protein pairs that do not necessarily localize to FAs. It would be exciting to carry out these measurements on choices of protein pairs that definitively exhibit location-specific differential binding ratios.

6.2.2 Other methods for external force application

More physiologically relevant force application methods can be applied in order to study effects that are more relevant in biological systems. Our stretch device can be modified for the application of cyclic stretch, with control over magnitude and frequency of the forcing function. Other force application methods could also be used, for example shear stress. Shear stress would be the more biologically relevant forcing method, mimicking blood flow over endothelial cells.

6.2.3 Faster image acquisition techniques

The length of time required for image acquisition, on the order of 15 mins for a complete set, is on the long side. This results in measurements that are averages over both space and time, due to the slight (but potentially significant) cell motion within this time frame. It would be of great benefit to reduce this time by further improvements in FLIM techniques. Some examples include video rate FLIM and multifocal multiphoton FLIM, the idea of which is intriguing.

References

1. **Agronskaia, A.V., L. Tertoolen, and H.C. Gerritsen**, Fast fluorescence lifetime imaging of calcium in living cells. *J Biomed Opt.* 9(6): p. 1230-7 2004.
2. **Ai, H.W., N.C. Shaner, Z. Cheng, R.Y. Tsien, and R.E. Campbell**, Exploration of new chromophore structures leads to the identification of improved blue fluorescent proteins. *Biochemistry.* 46(20): p. 5904-10 2007.
3. **Alcala, J.R., E. Gratton, and F.G. Prendergast**, Resolvability of fluorescence lifetime distributions using phase fluorometry. *Biophys J.* 51(4): p. 587-96 1987.
4. **Alcala, J.R., E. Gratton, and F.G. Prendergast**, Fluorescence lifetime distributions in proteins. *Biophys J.* 51(4): p. 597-604 1987.
5. **Alenghat, F.J. and D.E. Ingber**, Mechanotransduction: all signals point to cytoskeleton, matrix, and integrins. *Sci STKE.* 2002(119): p. PE6 2002.
6. **Alexandrakis, G., E.B. Brown, R.T. Tong, T.D. McKee, R.B. Campbell, Y. Boucher, and R.K. Jain**, Two-photon fluorescence correlation microscopy reveals the two-phase nature of transport in tumors. *Nat Med.* 10(2): p. 203-7 2004.
7. **Badimon, L., J.J. Badimon, W. Penny, M.W. Webster, J.H. Chesebro, and V. Fuster**, Endothelium and atherosclerosis. *J Hypertens Suppl.* 10(2): p. S43-50 1992.
8. **Baneyx, G., L. Baugh, and V. Vogel**, Fibronectin extension and unfolding within cell matrix fibrils controlled by cytoskeletal tension. *Proc Natl Acad Sci U S A.* 99(8): p. 5139-43 2002.
9. **Benes, M., D. Billy, W.T. Hermens, and M. Hof**, Muscovite (mica) allows the characterisation of supported bilayers by ellipsometry and confocal fluorescence correlation spectroscopy. *Biol Chem.* 383(2): p. 337-41 2002.
10. **Berland, K.M., P.T. So, and E. Gratton**, Two-photon fluorescence correlation spectroscopy: method and application to the intracellular environment. *Biophys J.* 68(2): p. 694-701 1995.
11. **Berney, C. and G. Danuser**, FRET or no FRET: a quantitative comparison. *Biophys J.* 84(6): p. 3992-4010 2003.
12. **Bishayee, A., L. Beguinot, and S. Bishayee**, Phosphorylation of tyrosine 992, 1068, and 1086 is required for conformational change of the human epidermal growth factor receptor c-terminal tail. *Mol Biol Cell.* 10(3): p. 525-36 1999.
13. **Biskup, C., T. Zimmer, L. Kelbauskas, B. Hoffmann, N. Klocker, W. Becker, A. Bergmann, and K. Benndorf**, Multi-dimensional fluorescence lifetime and FRET measurements. *Microsc Res Tech.* 70(5): p. 442-51 2007.
14. **Bismuto, E., E. Gratton, and D.C. Lamb**, Dynamics of ANS binding to tuna apomyoglobin measured with fluorescence correlation spectroscopy. *Biophys J.* 81(6): p. 3510-21 2001.
15. **Blann, A.D. and G.Y. Lip**, The endothelium in atherothrombotic disease: assessment of function, mechanisms and clinical implications. *Blood Coagul Fibrinolysis.* 9(4): p. 297-306 1998.
16. **Bradford, J.R. and D.R. Westhead**, Improved prediction of protein-protein binding sites using a support vector machines approach. *Bioinformatics.* 21(8): p. 1487-94 2005.
17. **Braunwald, E.**, Shattuck lecture--cardiovascular medicine at the turn of the millennium: triumphs, concerns, and opportunities. *N Engl J Med.* 337(19): p. 1360-9 1997.
18. **Breslow, J.L.**, Cardiovascular disease burden increases, NIH funding decreases. *Nat Med.* 3(6): p. 600-1 1997.

19. **Brooks, B.R., R.E. Bruccoleri, B.D. Olafson, D.J. States, S. Swaminathan, and M. Karplus**, Charmm - a program for macromolecular energy, minimization, and dynamics calculations. *Journal of Computational Chemistry.* 4(2): p. 187-217 1983.
20. **Brown, M.C., M.S. Curtis, and C.E. Turner**, Paxillin LD motifs may define a new family of protein recognition domains. *Nat Struct Biol.* 5(8): p. 677-8 1998.
21. **Butler, P.J., G. Norwich, S. Weinbaum, and S. Chien**, Shear stress induces a time- and position-dependent increase in endothelial cell membrane fluidity. *Am J Physiol Cell Physiol.* 280(4): p. C962-9 2001.
22. **Cance, W.G., J.E. Harris, M.V. Iacocca, E. Roche, X. Yang, J. Chang, S. Simkins, and L. Xu**, Immunohistochemical analyses of focal adhesion kinase expression in benign and malignant human breast and colon tissues: correlation with preinvasive and invasive phenotypes. *Clin Cancer Res.* 6(6): p. 2417-23 2000.
23. **Chang, G., R.H. Spencer, A.T. Lee, M.T. Barclay, and D.C. Rees**, Structure of the MscL homolog from Mycobacterium tuberculosis: a gated mechanosensitive ion channel. *Science.* 282(5397): p. 2220-6 1998.
24. **Chen, H., H.L. Puhl, 3rd, S.V. Koushik, S.S. Vogel, and S.R. Ikeda**, Measurement of FRET efficiency and ratio of donor to acceptor concentration in living cells. *Biophys J.* 91(5): p. L39-41 2006.
25. **Chien, S., S. Li, and Y.J. Shyy**, Effects of mechanical forces on signal transduction and gene expression in endothelial cells. *Hypertension.* 31(1 Pt 2): p. 162-9 1998.
26. **Choquet, D., D.P. Felsenfeld, and M.P. Sheetz**, Extracellular matrix rigidity causes strengthening of integrin-cytoskeleton linkages. *Cell.* 88(1): p. 39-48 1997.
27. **Chudakov, D.M., S. Lukyanov, and K.A. Lukyanov**, Fluorescent proteins as a toolkit for in vivo imaging. *Trends Biotechnol.* 23(12): p. 605-13 2005.
28. **Clayton, A.H., Q.S. Hanley, and P.J. Verveer**, Graphical representation and multicomponent analysis of single-frequency fluorescence lifetime imaging microscopy data. *J Microsc.* 213(Pt 1): p. 1-5 2004.
29. **Cohen-Kashi, M., Y. Namer, and M. Deutsch**, Fluorescence resonance energy transfer imaging via fluorescence polarization measurement. *J Biomed Opt.* 11(3): p. 34015 2006.
30. **Cohen, D.M., B. Kutscher, H. Chen, D.B. Murphy, and S.W. Craig**, A conformational switch in vinculin drives formation and dynamics of a talin-vinculin complex at focal adhesions. *J Biol Chem.* 281(23): p. 16006-15 2006.
31. **Cooley, M.A., J.M. Broome, C. Ohngemach, L.H. Romer, and M.D. Schaller**, Paxillin binding is not the sole determinant of focal adhesion localization or dominant-negative activity of focal adhesion kinase/focal adhesion kinase-related nonkinase. *Mol Biol Cell.* 11(9): p. 3247-63 2000.
32. **Cunningham, K.S. and A.I. Gotlieb**, The role of shear stress in the pathogenesis of atherosclerosis. *Lab Invest.* 85(1): p. 9-23 2005.
33. **Davies, P.F., A. Robotewskyj, and M.L. Griem**, Quantitative studies of endothelial cell adhesion. Directional remodeling of focal adhesion sites in response to flow forces. *J Clin Invest.* 93(5): p. 2031-8 1994.
34. **Davies, P.F.**, Flow-mediated endothelial mechanotransduction. *Physiol Rev.* 75(3): p. 519-60 1995.
35. **Davies, P.F., K.A. Barbee, M.V. Volin, A. Robotewskyj, J. Chen, L. Joseph, M.L. Griem, M.N. Wernick, E. Jacobs, D.C. Polacek, N. dePaola, and A.I. Barakat**, Spatial relationships in early signaling events of flow-mediated endothelial mechanotransduction. *Annu Rev Physiol.* 59: p. 527-49 1997.

36. **Davies, P.F., J. Zilberberg, and B.P. Helmke**, Spatial microstimuli in endothelial mechanosignaling. *Circ Res.* 92(4): p. 359-70 2003.
37. **Dewey, C.F., Jr., S.R. Bussolari, M.A. Gimbrone, Jr., and P.F. Davies**, The dynamic response of vascular endothelial cells to fluid shear stress. *J Biomech Eng.* 103(3): p. 177-85 1981.
38. **Diener, A., B. Nebe, F. Luthen, P. Becker, U. Beck, H.G. Neumann, and J. Rychly**, Control of focal adhesion dynamics by material surface characteristics. *Biomaterials.* 26(4): p. 383-92 2005.
39. **Dill, K.A., S.B. Ozkan, T.R. Weikl, J.D. Chodera, and V.A. Voelz**, The protein folding problem: when will it be solved? *Curr Opin Struct Biol.* 17(3): p. 342-6 2007.
40. **Edelman, L.M., R. Cheong, and J.D. Kahn**, Fluorescence resonance energy transfer over approximately 130 basepairs in hyperstable lac repressor-DNA loops. *Biophys J.* 84(2 Pt 1): p. 1131-45 2003.
41. **Elson, E.L. and D. Magde**, Fluorescence correlation spectroscopy. I. Conceptual basis and theory. *Biopolymers.* 13(1): p. 1-27 1974.
42. **Elson, E.L., I. Munro, J. Requejo-Isidro, J. McGinty, C. Dunsby, N. Galletly, G.W. Stamp, M.A.A. Neil, M.J. Lever, P.A. Kellett, A. Dymoke-Bradshaw, J. Hares, and P.M.W. French**, Real-time time-domain fluorescence lifetime imaging including single-shot acquisition with a segmented optical image intensifier. *New Journal of Physics 6.* 180: p. 1-13 2004.
43. **Engler, A., L. Bacakova, C. Newman, A. Hategan, M. Griffin, and D. Discher**, Substrate compliance versus ligand density in cell on gel responses. *Biophys J.* 86(1 Pt 1): p. 617-28 2004.
44. **Evans, E. and K. Ritchie**, Dynamic strength of molecular adhesion bonds. *Biophys J.* 72(4): p. 1541-55 1997.
45. **Festy, F., S.M. Ameer-Beg, T. Ng, and K. Suhling**, Imaging proteins in vivo using fluorescence lifetime microscopy. *Mol Biosyst.* 3(6): p. 381-91 2007.
46. **Fielding, L., S. Rutherford, and D. Fletcher**, Determination of protein-ligand binding affinity by NMR: observations from serum albumin model systems. *Magnetic Resonance in Chemistry.* 43: p. 463-470 2005.
47. **Fivash, M., E.M. Towler, and R.J. Fisher**, BIAcore for macromolecular interaction. *Curr Opin Biotechnol.* 9(1): p. 97-101 1998.
48. **Förster, T.**, Intermolecular energy migration and fluorescence. *Ann. Phys. (Leipzig).* 2: p. 55-75 1948.
49. **Frangos, S.G., V. Gahtan, and B. Sumpio**, Localization of atherosclerosis: role of hemodynamics. *Arch Surg.* 134(10): p. 1142-9 1999.
50. **Galbraith, C.G., K.M. Yamada, and M.P. Sheetz**, The relationship between force and focal complex development. *J Cell Biol.* 159(4): p. 695-705 2002.
51. **Gao, G., K.C. Prutzman, M.L. King, D.M. Scheswohl, E.F. DeRose, R.E. London, M.D. Schaller, and S.L. Campbell**, NMR solution structure of the focal adhesion targeting domain of focal adhesion kinase in complex with a paxillin LD peptide: evidence for a two-site binding model. *J Biol Chem.* 279(9): p. 8441-51 2004.
52. **Geiger, B., Z. Avnur, T.E. Kreis, and J. Schlessinger**, The dynamics of cytoskeletal organization in areas of cell contact. *Cell Muscle Motil.* 5: p. 195-234 1984.
53. **Geiger, B., A. Bershadsky, R. Pankov, and K.M. Yamada**, Transmembrane crosstalk between the extracellular matrix--cytoskeleton crosstalk. *Nat Rev Mol Cell Biol.* 2(11): p. 793-805 2001.

54. **Geiger, B. and A. Bershadsky**, Exploring the neighborhood: adhesion-coupled cell mechanosensors. *Cell.* 110(2): p. 139-42 2002.
55. **Ghukasyan, V., Y.Y. Hsu, S.H. Kung, and F.J. Kao**, Application of fluorescence resonance energy transfer resolved by fluorescence lifetime imaging microscopy for the detection of enterovirus 71 infection in cells. *J Biomed Opt.* 12(2): p. 024016 2007.
56. **Gimbrone, M.A., Jr., J.N. Topper, T. Nagel, K.R. Anderson, and G. Garcia-Cardena**, Endothelial dysfunction, hemodynamic forces, and atherogenesis. *Ann N Y Acad Sci.* 902: p. 230-9; discussion 239-40 2000.
57. **Göppert-Mayer, M.**, Uber elementarakte mit zwei quantensprungen. *Ann. Phys. (Leipzig).* 5: p. 273-294 1931.
58. **Gosling, J.P.**, A decade of development in immunoassay methodology. *Clin Chem.* 36(8 Pt 1): p. 1408-27 1990.
59. **Gough, C.A., T. Gojobori, and T. Imanishi**, Cancer-related mutations in BRCA1-BRCT cause long-range structural changes in protein-protein binding sites: a molecular dynamics study. *Proteins.* 66(1): p. 69-86 2007.
60. **Gratton, E., S. Breusegem, J. Sutin, Q. Ruan, and N. Barry**, Fluorescence lifetime imaging for the two-photon microscope: time-domain and frequency-domain methods. *J Biomed Opt.* 8(3): p. 381-90 2003.
61. **Hagel, M., E.L. George, A. Kim, R. Tamimi, S.L. Opitz, C.E. Turner, A. Imamoto, and S.M. Thomas**, The adaptor protein paxillin is essential for normal development in the mouse and is a critical transducer of fibronectin signaling. *Mol Cell Biol.* 22(3): p. 901-15 2002.
62. **Haidekker, M.A., N. L'Heureux, and J.A. Frangos**, Fluid shear stress increases membrane fluidity in endothelial cells: a study with DCVJ fluorescence. *Am J Physiol Heart Circ Physiol.* 278(4): p. H1401-6 2000.
63. **Haraguchi, T., T. Shimi, T. Koujin, N. Hashiguchi, and Y. Hiraoka**, Spectral imaging fluorescence microscopy. *Genes Cells.* 7(9): p. 881-7 2002.
64. **Haupts, U., S. Maiti, P. Schwille, and W.W. Webb**, Dynamics of fluorescence fluctuations in green fluorescent protein observed by fluorescence correlation spectroscopy. *Proc Natl Acad Sci U S A.* 95(23): p. 13573-8 1998.
65. **Hayashi, I., K. Vuori, and R.C. Liddington**, The focal adhesion targeting (FAT) region of focal adhesion kinase is a four-helix bundle that binds paxillin. *Nat Struct Biol.* 9(2): p. 101-6 2002.
66. **Hoellerer, M.K., M.E. Noble, G. Labesse, I.D. Campbell, J.M. Werner, and S.T. Arold**, Molecular recognition of paxillin LD motifs by the focal adhesion targeting domain. *Structure.* 11(10): p. 1207-17 2003.
67. **Homola, J.**, Present and future of surface plasmon resonance biosensors. *Anal Bioanal Chem.* 377(3): p. 528-39 2003.
68. **Howard, A.B., R.W. Alexander, R.M. Nerem, K.K. Griendling, and W.R. Taylor**, Cyclic strain induces an oxidative stress in endothelial cells. *Am J Physiol.* 272(2 Pt 1): p. C421-7 1997.
69. **Huang, H., R.D. Kamm, and R.T. Lee**, Cell mechanics and mechanotransduction: pathways, probes, and physiology. *Am J Physiol Cell Physiol.* 287(1): p. C1-11 2004.
70. **Hytonen, V.P. and V. Vogel**, How Force Might Activate Talin's Vinculin Binding Sites: SMD Reveals a Structural Mechanism. *PLoS Comput Biol.* 4(2): p. e24 2008.
71. **Ikada, Y.**, Tissue Engineering: Fundamentals and Applications. p. 61 2006.
72. **Ilic, D., B. Kovacic, K. Johkura, D.D. Schlaepfer, N. Tomasevic, Q. Han, J.B. Kim, K. Howerton, C. Baumbusch, N. Ogiwara, D.N. Streblow, J.A. Nelson, P. Dazin, Y.**

Shino, K. Sasaki, and C.H. Damsky, FAK promotes organization of fibronectin matrix and fibrillar adhesions. *J Cell Sci.* 117(Pt 2): p. 177-87 2004.

73. **Isralewitz, B., M. Gao, and K. Schulten**, Steered molecular dynamics and mechanical functions of proteins. *Curr Opin Struct Biol.* 11(2): p. 224-30 2001.
74. **Janmey, P.A. and D.A. Weitz**, Dealing with mechanics: mechanisms of force transduction in cells. *Trends Biochem Sci.* 29(7): p. 364-70 2004.
75. **Kamm, R.D. and M.R. Kaazempur Mofrad**, On the molecular basis for mechanotransduction. *MCB.* 1(3): p. 201-209 2004.
76. **Kettling, U., A. Koltermann, P. Schwille, and M. Eigen**, Real-time enzyme kinetics monitored by dual-color fluorescence cross-correlation spectroscopy. *Proc Natl Acad Sci U S A.* 95(4): p. 1416-20 1998.
77. **Kim, K.H., C. Buehler, K. Bahlmann, T. Ragan, L.W.C. A., E. Nedivi, E. Heffer, S. Fantini, and P.T. So**, Multifocal multiphoton microscopy based on multianode photomultiplier tubes. *Optics Express.* 15(18): p. 11658-11678 2007.
78. **Kim, S.A., K.G. Heinze, K. Bacia, M.N. Waxham, and P. Schwille**, Two-photon cross-correlation analysis of intracellular reactions with variable stoichiometry. *Biophys J.* 88(6): p. 4319-36 2005.
79. **Klonis N, S.W.**, Spectral Properties of the Prototropic Forms of Fluorescein in Aqueous Solution. *Journal of Fluorescence.* 6(3) 1996.
80. **Korlach, J., P. Schwille, W.W. Webb, and G.W. Feigenson**, Characterization of lipid bilayer phases by confocal microscopy and fluorescence correlation spectroscopy. *Proc Natl Acad Sci U S A.* 96(15): p. 8461-6 1999.
81. Lakowicz, J.R., *Principles of Fluorescence Spectroscopy.* 2006.
82. **Laukaitis, C.M., D.J. Webb, K. Donais, and A.F. Horwitz**, Differential dynamics of alpha 5 integrin, paxillin, and alpha-actinin during formation and disassembly of adhesions in migrating cells. *J Cell Biol.* 153(7): p. 1427-40 2001.
83. **Leavitt, S.A. and E. Freire**, Direct measurement of protein binding energetics by isothermal titration calorimetry *Current Opinion in Structural Biology.* 11(5): p. 560-566 2001.
84. **Lee, A.A., T. Delhaas, L.K. Waldman, D.A. MacKenna, F.J. Villarreal, and A.D. McCulloch**, An equibiaxial strain system for cultured cells. *Am J Physiol.* 271(4 Pt 1): p. C1400-8 1996.
85. **Lee, S.E., R.D. Kamm, and M.R. Mofrad**, Force-induced activation of talin and its possible role in focal adhesion mechanotransduction. *J Biomech.* 40(9): p. 2096-106 2007.
86. **Lehoux, S., B. Esposito, R. Merval, and A. Tedgui**, Differential regulation of vascular focal adhesion kinase by steady stretch and pulsatility. *Circulation.* 111(5): p. 643-9 2005.
87. **Lele, T.P., J. Pendse, S. Kumar, M. Salanga, J. Karavitis, and D.E. Ingber**, Mechanical forces alter zyxin unbinding kinetics within focal adhesions of living cells. *J Cell Physiol.* 207(1): p. 187-94 2006.
88. **Levesque, M.J., R.M. Nerem, and E.A. Sprague**, Vascular endothelial cell proliferation in culture and the influence of flow. *Biomaterials.* 11(9): p. 702-7 1990.
89. **Li, S., M. Kim, Y.L. Hu, S. Jalali, D.D. Schlaepfer, T. Hunter, S. Chien, and J.Y. Shyy**, Fluid shear stress activation of focal adhesion kinase. Linking to mitogen-activated protein kinases. *J Biol Chem.* 272(48): p. 30455-62 1997.
90. **Lidke, K.A., B. Rieger, D.S. Lidke, and T.M. Jovin**, The role of photon statistics in fluorescence anisotropy imaging. *IEEE Trans Image Process.* 14(9): p. 1237-45 2005.
91. **Lo, C.M., H.B. Wang, M. Dembo, and Y.L. Wang**, Cell movement is guided by the rigidity of the substrate. *Biophys J.* 79(1): p. 144-52 2000.

92. **Mack, P.J., M.R. Kaazempur-Mofrad, H. Karcher, R.T. Lee, and R.D. Kamm**, Force-induced focal adhesion translocation: effects of force amplitude and frequency. *Am J Physiol Cell Physiol.* 287(4): p. C954-62 2004.
93. **MacKerell Jr, A.D., D. Bashford, M. Bellott, R.L.J. Dunbrack, J.D. Evanseck, M.J. Field, S. Fischer, J. Gao, H. Guo, S. Ha, D. Joseph-McCarthy, L. Kuchnir, K. Kiczera, F.T.K. Lau, C. Mattos, S. Michnick, T. Ngo, D.T. Nguyen, B. Prodhom, W.E.I. Reiher, B. Roux, M. Schlenkrich, J.C. Smith, R. Stote, J. Straub, M. Watanabe, J. Wiorkiewicz-Kuczera, D. Yin, and M. Karplus**, All-atom empirical potential for molecular modeling and dynamics studies of proteins. *J. Phys. Chem. B.* 102: p. 3586-3616 1998.
94. **Magde, D., E.L. Elson, and W.W. Webb**, Fluorescence correlation spectroscopy. II. An experimental realization. *Biopolymers.* 13(1): p. 29-61 1974.
95. **Marganski, W.A., M. Dembo, and Y.L. Wang**, Measurements of cell-generated deformations on flexible substrata using correlation-based optical flow. *Methods Enzymol.* 361: p. 197-211 2003.
96. **Marques, O. and Y.H. Sanejouand**, Hinge-bending motion in citrate synthase arising from normal mode calculations. *Proteins.* 23(4): p. 557-60 1995.
97. **Marszalek, P.E., H. Lu, H. Li, M. Carrion-Vazquez, A.F. Oberhauser, K. Schulten, and J.M. Fernandez**, Mechanical unfolding intermediates in titin modules. *Nature.* 402: p. 100-103 1999.
98. **Mattheyses, A.L., A.D. Hoppe, and D. Axelrod**, Polarized fluorescence resonance energy transfer microscopy. *Biophys J.* 87(4): p. 2787-97 2004.
99. **Millington, M., G.J. Grindlay, K. Altenbach, R.K. Neely, W. Kolch, M. Bencina, N.D. Read, A.C. Jones, D.T. Dryden, and S.W. Magennis**, High-precision FLIM-FRET in fixed and living cells reveals heterogeneity in a simple CFP-YFP fusion protein. *Biophys Chem.* 127(3): p. 155-64 2007.
100. **Minton, A.P.**, How can biochemical reactions within cells differ from those in test tubes? *J Cell Sci.* 119(Pt 14): p. 2863-9 2006.
101. **Mitra, S.K., D.A. Hanson, and D.D. Schlaepfer**, Focal adhesion kinase: in command and control of cell motility. *Nat Rev Mol Cell Biol.* 6(1): p. 56-68 2005.
102. **Mofrad, M.R., J. Golji, N.A. Abdul Rahim, and R.D. Kamm**, Force-induced unfolding of the focal adhesion targeting domain and the influence of paxillin binding. *Mech Chem Biosyst.* 1(4): p. 253-65 2004.
103. **Moretti, M., A. Prina-Mello, A.J. Reid, V. Barron, and P.J. Prendergast**, Endothelial cell alignment on cyclically-stretched silicone surfaces. *J Mater Sci Mater Med.* 15(10): p. 1159-64 2004.
104. **Morgan, C.L., D.J. Newman, and C.P. Price**, Immunosensors: technology and opportunities in laboratory medicine. *Clin Chem.* 42(2): p. 193-209 1996.
105. **Nilius, B. and G. Droogmans**, Ion channels and their functional role in vascular endothelium. *Physiol Rev.* 81(4): p. 1415-59 2001.
106. **Oemar, B.S., M.R. Tschudi, N. Godoy, V. Brovkovich, T. Malinski, and T.F. Luscher**, Reduced endothelial nitric oxide synthase expression and production in human atherosclerosis. *Circulation.* 97(25): p. 2494-8 1998.
107. **Olesen, S.P., P.F. Davies, and D.E. Clapham**, Muscarinic-activated K+ current in bovine aortic endothelial cells. *Circ Res.* 62(6): p. 1059-64 1988.
108. **Ortiz, V., S.O. Nielsen, M.L. Klein, and D.E. Discher**, Unfolding a linker between helical repeats. *J Mol Biol.* 349(3): p. 638-47 2005.

109. **Palmer, A.G., 3rd and N.L. Thompson**, Fluorescence correlation spectroscopy for detecting submicroscopic clusters of fluorescent molecules in membranes. *Chem Phys Lipids.* 50(3-4): p. 253-70 1989.
110. **Paramore, S. and G.A. Voth**, Examining the influence of linkers and tertiary structure in the forced unfolding of multiple-repeat spectrin molecules. *Biophys J.* 91(9): p. 3436-45 2006.
111. **Parsons, M., J. Monypenny, S.M. Ameer-Beg, T.H. Millard, L.M. Machesky, M. Peter, M.D. Keppler, G. Schiavo, R. Watson, J. Chernoff, D. Zicha, B. Vojnovic, and T. Ng**, Spatially distinct binding of Cdc42 to PAK1 and N-WASP in breast carcinoma cells. *Mol Cell Biol.* 25(5): p. 1680-95 2005.
112. **Patterson, G.H., D.W. Piston, and B.G. Barisas**, Forster distances between green fluorescent protein pairs. *Anal Biochem.* 284(2): p. 438-40 2000.
113. **Pelet, S., M. Previte, L. Laiho, and P. So**, A fast global fitting algorithm for fluorescence lifetime imaging microscopy based on image segmentation. *Biophys J.* 87(4): p. 2807-17 2004.
114. **Pelet, S., M.J. Previte, and P.T. So**, Comparing the quantification of Forster resonance energy transfer measurement accuracies based on intensity, spectral, and lifetime imaging. *J Biomed Opt.* 11(3): p. 34017 2006.
115. **Peter, M., S.M. Ameer-Beg, M.K. Hughes, M.D. Keppler, S. Prag, M. Marsh, B. Vojnovic, and T. Ng**, Multiphoton-FLIM quantification of the EGFP-mRFP1 FRET pair for localization of membrane receptor-kinase interactions. *Biophys J.* 88(2): p. 1224-37 2005.
116. **Phillips, J.C., R. Braun, W. Wang, J. Gumbart, E. Tajkhorshid, E. Villa, C. Chipot, R.D. Skeel, L. Kale, and K. Schulten**, Scalable molecular dynamics with NAMD. *J Comput Chem.* 26(16): p. 1781-802 2005.
117. **Previte, M.J., S. Pelet, K.H. Kim, C. Buehler, and P.T. So**, Spectrally resolved fluorescence correlation spectroscopy based on global analysis (SRFCS-G). *Analytical Chemistry.* In press 2008.
118. **Prutzman, K.C., G. Gao, M.L. King, V.V. Iyer, G.A. Mueller, M.D. Schaller, and S.L. Campbell**, The focal adhesion targeting domain of focal adhesion kinase contains a hinge region that modulates tyrosine 926 phosphorylation. *Structure (Camb).* 12(5): p. 881-91 2004.
119. **Rarbach, M., U. Kettling, A. Koltermann, and M. Eigen**, Dual-color fluorescence cross-correlation spectroscopy for monitoring the kinetics of enzyme-catalyzed reactions. *Methods.* 24(2): p. 104-16 2001.
120. **Rich, R.L. and D.G. Myszka**, Advances in surface plasmon resonance biosensor analysis. *Curr Opin Biotechnol.* 11(1): p. 54-61 2000.
121. **Rief, M., J. Pascual, M. Saraste, and H.E. Gaub**, Single molecule force spectroscopy of spectrin repeats: low unfolding forces in helix bundles. *J Mol Biol.* 286(2): p. 553-61 1999.
122. **Riveline, D., E. Zamir, N.Q. Balaban, U.S. Schwarz, T. Ishizaki, S. Narumiya, Z. Kam, B. Geiger, and A.D. Bershadsky**, Focal contacts as mechanosensors: externally applied local mechanical force induces growth of focal contacts by an mDia1-dependent and ROCK-independent mechanism. *J Cell Biol.* 153(6): p. 1175-86 2001.
123. **Rizzo, M.A. and D.W. Piston**, High-contrast imaging of fluorescent protein FRET by fluorescence polarization microscopy. *Biophys J.* 88(2): p. L14-6 2005.
124. **Ross, R., J. Glomset, and L. Harker**, Response to injury and atherogenesis. *Am J Pathol.* 86(3): p. 675-84 1977.
125. **Sawada, Y. and M.P. Sheetz**, Force transduction by Triton cytoskeletons. *J Cell Biol.* 156(4): p. 609-15 2002.
126. **Schwille, P., U. Haupts, S. Maiti, and W.W. Webb**, Molecular dynamics in living cells observed by fluorescence correlation spectroscopy with one- and two-photon excitation. *Biophys J.* 77(4): p. 2251-65 1999.

127. **Schwille, P., S. Kummer, A.A. Heikal, W.E. Moerner, and W.W. Webb**, Fluorescence correlation spectroscopy reveals fast optical excitation-driven intramolecular dynamics of yellow fluorescent proteins. *Proc Natl Acad Sci U S A.* 97(1): p. 151-6 2000.
128. **Schwille, P. and E. Haustein**, Fluorescence Correlation Spectroscopy: An introduction to its concepts and applications. *Biophysics Textbook Online.* p. 1-33 2004.
129. **Shaner, N.C., R.E. Campbell, P.A. Steinbach, B.N. Giepmans, A.E. Palmer, and R.Y. Tsien**, Improved monomeric red, orange and yellow fluorescent proteins derived from Discosoma sp. red fluorescent protein. *Nat Biotechnol.* 22(12): p. 1567-72 2004.
130. **Shaner, N.C., P.A. Steinbach, and R.Y. Tsien**, A guide to choosing fluorescent proteins. *Nat Methods.* 2(12): p. 905-9 2005.
131. **Shikata, Y., A. Rios, K. Kawkitinarong, N. DePaola, J.G. Garcia, and K.G. Birukov**, Differential effects of shear stress and cyclic stretch on focal adhesion remodeling, site-specific FAK phosphorylation, and small GTPases in human lung endothelial cells. *Exp Cell Res.* 304(1): p. 40-9 2005.
132. **Shu, X., N.C. Shaner, C.A. Yarbrough, R.Y. Tsien, and S.J. Remington**, Novel chromophores and buried charges control color in mFruits. *Biochemistry.* 45(32): p. 9639-47 2006.
133. **Shyy, J.Y. and S. Chien**, Role of integrins in endothelial mechanosensing of shear stress. *Circ Res.* 91(9): p. 769-75 2002.
134. **So, P.T., C.Y. Dong, B.R. Masters, and K.M. Berland**, Two-photon excitation fluorescence microscopy. *Annu Rev Biomed Eng.* 2: p. 399-429 2000.
135. **Sokabe, M., K. Naruse, S. Sai, T. Yamada, K. Kawakami, M. Inoue, K. Murase, and M. Miyazu**, Mechanotransduction and intracellular signaling mechanisms of stretch-induced remodeling in endothelial cells. *Heart Vessels.* Suppl 12: p. 191-3 1997.
136. **Sotomayor, M. and K. Schulten**, Single-molecule experiments in vitro and in silico. *Science.* 316(5828): p. 1144-8 2007.
137. Stevens, R.J., K.M.J. Douglas, A.N. Saratzis, and G.D. Kitas, *Expert Reviews in Molecular Medicine.* Vol. 7. 2005: Cambridge University Press.
138. **Stultz, C.M., A.D. Levin, and E.R. Edelman**, Phosphorylation-induced conformational changes in a mitogen-activated protein kinase substrate. Implications for tyrosine hydroxylase activation. *J Biol Chem.* 277(49): p. 47653-61 2002.
139. **Tama, F. and Y.H. Sanejouand**, Conformational change of proteins arising from normal mode calculations. *Protein Eng.* 14(1): p. 1-6 2001.
140. **Tarbell, J.M. and M.Y. Pahakis**, Mechanotransduction and the glycocalyx. *J Intern Med.* 259(4): p. 339-50 2006.
141. **Thaler, C., S.V. Koushik, P.S. Blank, and S.S. Vogel**, Quantitative multiphoton spectral imaging and its use for measuring resonance energy transfer. *Biophys J.* 89(4): p. 2736-49 2005.
142. **Thomas, J.W., M.A. Cooley, J.M. Broome, R. Salgia, J.D. Griffin, C.R. Lombardo, and M.D. Schaller**, The role of focal adhesion kinase binding in the regulation of tyrosine phosphorylation of paxillin. *J Biol Chem.* 274(51): p. 36684-92 1999.
143. **Torres, T. and M. Levitus**, Measuring conformational dynamics: a new FCS-FRET approach. *J Phys Chem B.* 111(25): p. 7392-400 2007.
144. **Toutant, M., A. Costa, J.M. Studler, G. Kadare, M. Carnaud, and J.A. Girault**, Alternative splicing controls the mechanisms of FAK autophosphorylation. *Mol Cell Biol.* 22(22): p. 7731-43 2002.

145. **Truong, K. and M. Ikura**, The use of FRET imaging microscopy to detect protein-protein interactions and protein conformational changes in vivo. *Curr Opin Struct Biol.* 11(5): p. 573-8 2001.
146. **Tsien, R.Y.**, The green fluorescent protein. *Annu Rev Biochem.* 67: p. 509-44 1998.
147. **Tzima, E., M. Irani-Tehrani, W.B. Kiosses, E. Dejana, D.A. Schultz, B. Engelhardt, G. Cao, H. DeLisser, and M.A. Schwartz**, A mechanosensory complex that mediates the endothelial cell response to fluid shear stress. *Nature.* 437(7057): p. 426-31 2005.
148. **Vajda, S. and C.J. Camacho**, Protein-protein docking: is the glass half-full or half-empty? *Trends Biotechnol.* 22(3): p. 110-6 2004.
149. **van Munster, E.B. and T.W. Gadella**, Fluorescence lifetime imaging microscopy (FLIM). *Adv Biochem Eng Biotechnol.* 95: p. 143-75 2005.
150. **Van Munster, E.B., G.J. Kremers, M.J.W. Adjobo-Hermans, and T.W.J. Gadella Jr**, Fluorescence resonance energy transfer (FRET) measurement by gradual acceptor photobleaching. *Journal of Microscopy.* 218(3): p. 253-262 2005.
151. **Velazquez-Campoy, A., S.A. Leavitt, and E. Freire**, Characterization of protein-protein interactions by isothermal titration calorimetry. *Methods Mol Biol.* 261: p. 35-54 2004.
152. **Velazquez Campoy, A. and E. Freire**, ITC in the post-genomic era...? Priceless. *Biophys Chem.* 115(2-3): p. 115-24 2005.
153. **Verveer, P.J., A. Squire, and P.I. Bastiaens**, Global analysis of fluorescence lifetime imaging microscopy data. *Biophys J.* 78(4): p. 2127-37 2000.
154. **Verveer, P.J. and P.I. Bastiaens**, Evaluation of global analysis algorithms for single frequency fluorescence lifetime imaging microscopy data. *J Microsc.* 209(Pt 1): p. 1-7 2003.
155. **Vogel, S.S., C. Thaler, and S.V. Koushik**, Fanciful FRET. *Sci STKE.* 2006(331): p. re2 2006.
156. **Vogel, V., W.E. Thomas, D.W. Craig, A. Krammer, and G. Baneyx**, Structural insights into the mechanical regulation of molecular recognition sites. *Trends Biotechnol.* 19(10): p. 416-23 2001.
157. **Wallrabe, H. and A. Periasamy**, Imaging protein molecules using FRET and FLIM microscopy. *Curr Opin Biotechnol.* 16(1): p. 19-27 2005.
158. **Wang, J.G., M. Miyazu, E. Matsushita, M. Sokabe, and K. Naruse**, Uniaxial cyclic stretch induces focal adhesion kinase (FAK) tyrosine phosphorylation followed by mitogen-activated protein kinase (MAPK) activation. *Biochem Biophys Res Commun.* 288(2): p. 356-61 2001.
159. **Weinbaum, S., X. Zhang, Y. Han, H. Vink, and S.C. Cowin**, Mechanotransduction and flow across the endothelial glycocalyx. *Proc Natl Acad Sci U S A.* 100(13): p. 7988-95 2003.
160. **White, C.C., P.L. Drzal, and M.R. VanLandingham**, Viscoelastic Characterization of Polymers Using Dynamics Instrumented Indentation. *Mater. Res. Soc. Symp. Proc.* 841: p. R5.3.1-R5.3.6 2005.
161. **Willits, R.K. and S.L. Skornia**, Effect of collagen gel stiffness on neurite extension. *J Biomater Sci Polym Ed.* 15(12): p. 1521-31 2004.
162. **Wohland, T., K. Friedrich, R. Hovius, and H. Vogel**, Study of ligand-receptor interactions by fluorescence correlation spectroscopy with different fluorophores: evidence that the homopentameric 5-hydroxytryptamine type 3As receptor binds only one ligand. *Biochemistry.* 38(27): p. 8671-81 1999.
163. **Wu, P. and L. Brand**, Resonance energy transfer: methods and applications. *Anal Biochem.* 218(1): p. 1-13 1994.

164. **Yamamoto, T., R. El-Hayek, and N. Ikemoto**, Postulated role of interdomain interaction within the ryanodine receptor in Ca(2+) channel regulation. *J Biol Chem.* 275(16): p. 11618-25 2000.
165. **Yamawaki, H., S. Pan, R.T. Lee, and B.C. Berk**, Fluid shear stress inhibits vascular inflammation by decreasing thioredoxin-interacting protein in endothelial cells. *J Clin Invest.* 115(3): p. 733-8 2005.
166. **Yao, Y., A. Rabodzey, and C.F. Dewey, Jr.**, Glycocalyx modulates the motility and proliferative response of vascular endothelium to fluid shear stress. *Am J Physiol Heart Circ Physiol.* 293(2): p. H1023-30 2007.
167. **Yeung, T., P.C. Georges, L.A. Flanagan, B. Marg, M. Ortiz, M. Funaki, N. Zahir, W. Ming, V. Weaver, and P.A. Janmey**, Effects of substrate stiffness on cell morphology, cytoskeletal structure, and adhesion. *Cell Motil Cytoskeleton.* 60(1): p. 24-34 2005.
168. **Yin, H., M.D. Wang, K. Svoboda, R. Landick, S.M. Block, and J. Gelles**, Transcription against an applied force. *Science.* 270(5242): p. 1653-7 1995.
169. **Zal, T. and N.R. Gascoigne**, Photobleaching-corrected FRET efficiency imaging of live cells. *Biophys J.* 86(6): p. 3923-39 2004.
170. **Zamir, E. and B. Geiger**, Components of cell-matrix adhesions. *J Cell Sci.* 114(Pt 20): p. 3577-9 2001.
171. **Zimerman, B., T. Volberg, and B. Geiger**, Early molecular events in the assembly of the focal adhesion-stress fiber complex during fibroblast spreading. *Cell Motil Cytoskeleton.* 58(3): p. 143-59 2004.